

FINAL REPORT ON

**APPLICATION OF MODEL-BASED SIGNAL
PROCESSING METHODS TO COMPUTATIONAL
ELECTROMAGNETICS SIMULATORS**

**Office of Naval Research
Research Grant N00014-98-1-0178**

For the period December 1, 1997 through November 30, 2000

Submitted by

Professor Hao Ling

**Department of Electrical and Computer Engineering
The University of Texas at Austin
Austin, TX 78712-1084**

December 31, 2000

**Reproduced From
Best Available Copy**

DTIC QUALITY INSPECTED 1

20010129 036

REPORT DOCUMENTATION PAGEForm Approved
OMB No. 0704-0188

Public reporting burden for this collection of information is estimated to average 1 hour per response, including the time for reviewing instructions, searching existing data sources, gathering and maintaining the data needed, and completing and reviewing the collection of information. Send comments regarding this burden estimate or any other aspect of this collection of information, including suggestions for reducing this burden to Washington Headquarters Services, Directorate for Information Operations and Reports, 1215 Jefferson Davis Highway, Suite 1204, Arlington, VA 22202-4302, and to the Office of Management and Budget, Paperwork Reduction Project (0704-0188), Washington, DC 20503.

1. AGENCY USE ONLY (Leave blank)		2. REPORT DATE Dec. 31, 2000	3. REPORT TYPE AND DATES COVERED Final Report 1 Dec. 97 - 30 Nov. 00	
4. TITLE AND SUBTITLE Final Report on Application of Model-Based Signal Processing Methods to CEM Simulators			5. FUNDING NUMBERS Research Grant ONR N00014-98-1-0178	
6. AUTHOR(S) Hao Ling				
7. PERFORMING ORGANIZATION NAMES(S) AND ADDRESS(ES) The University of Texas at Austin Department of Electrical and Computer Engineering Austin, TX 78712-1084			8. PERFORMING ORGANIZATION REPORT NUMBER No. 3	
9. SPONSORING / MONITORING AGENCY NAMES(S) AND ADDRESS(ES) Office of Naval Research Ballston Centre Tower One 800 North Quincy Street Arlington, VA 22217-5660 Program Officer Reza Malek-Madani ONR 311			10. SPONSORING / MONITORING AGENCY REPORT NUMBER	
11. SUPPLEMENTARY NOTES				
a. DISTRIBUTION / AVAILABILITY STATEMENT Approved for Public Release Distribution Unlimited			12. DISTRIBUTION CODE	
13. ABSTRACT (Maximum 200 words) This report summarizes the scientific progress on the research grant "Application of Model-Based Signal Processing Methods to Computational Electromagnetics Simulators" during the period 1 December 1997 - 30 November 2000. Progress on model-based extrapolation and interpolation of complex radiation and scattering phenomena in frequency and aspect is described.				
14. SUBJECT TERMS Computational electromagnetics Model-based signal processing			15. NUMBER OF PAGES 120	
			16. PRICE CODE	
17. SECURITY CLASSIFICATION OF REPORT Unclassified	18. SECURITY CLASSIFICATION OF THIS PAGE Unclassified	19. SECURITY CLASSIFICATION OF ABSTRACT Unclassified	20. LIMITATION OF ABSTRACT	

FINAL REPORT ON

**APPLICATION OF MODEL-BASED SIGNAL
PROCESSING METHODS TO COMPUTATIONAL
ELECTROMAGNETICS SIMULATORS**

**Office of Naval Research
Research Grant N00014-98-1-0178**

For the period December 1, 1997 through November 30, 2000

Submitted by

Professor Hao Ling

**Department of Electrical and Computer Engineering
The University of Texas at Austin
Austin, TX 78712-1084**

December 31, 2000

APPLICATION OF MODEL-BASED SIGNAL PROCESSING METHODS TO COMPUTATIONAL ELECTROMAGNETICS SIMULATORS

Project Starting Date: Dec. 1, 1997

Reporting Period: Dec. 1, 1997 – Nov. 30, 2000

Principal Investigator: Professor Hao Ling
(512) 471-1710
ling@ece.utexas.edu

Graduate Students: Tao Su, Bin Jiang, Hosung Choo

A. SCIENTIFIC OBJECTIVES: The objective of this research program is to apply model-based signal processing methods to enhance the performance of computation electromagnetics (CEM) simulators for shipboard antenna design. While recent advances in CEM algorithms has significantly reduced the simulation cost of modeling complex radiation and scattering phenomena, real-world engineering design and optimization often require that calculations be carried out repeatedly over large parameter spaces such as frequency and aspect angle, making the computation cost still exceedingly high. The goal of this research is to apply model-based signal processing algorithms to CEM simulators to overcome such computational bottleneck and achieve higher design throughput. In particular, we address the issue of how to interpolate and extrapolate the frequency and angular behaviors of antenna characteristics based on a sparse set of computed data. We develop algorithms to extract sparse and physical models of the relevant physics embedded in CEM data to facilitate design and synthesis. Finally, we explore the transportability of the methodology to other applications such as radar signatures and wireless channel characteristics.

B. SUMMARY OF RESULTS AND SIGNIFICANT ACCOMPLISHMENTS: Our research during the three-year duration of this program has been focused on three topics. First, we have developed a number of model-based algorithms to extrapolate and interpolate the frequency and angular behaviors of antenna radiation and scattering characteristics on complex platforms. These algorithms can lead to orders of magnitude

reduction in computation time in populating a large data set from a limited number of computed data. Second, we have developed algorithms to extract sparse and highly physical models of antenna radiation data on complex platforms from CEM data. The extracted features can be used to pinpoint the locations of platform scattering for engineering design and optimization. Third, we have investigated the effect of mutual coupling and platform interaction on the performance of antenna arrays mounted on complex platforms. Both theoretical analysis and measurements have been carried out to assess the near-field effect of the mounting environment on the direction finding performance of antenna arrays. In addition to these three main topics, we have also carried out exploratory research in two areas. First, we have proposed and implemented algorithms to improve the speed and accuracy of CEM solvers based on the fast multipole method. We have proposed a new set of triangular basis functions to improve the accuracy of the traditional Rao-Wilton-Glisson basis. We have also proposed a low-complexity, wavelet-based preconditioner to accelerate the convergence rate of iterative solvers. Second, we have explored the use of genetic algorithm together with CEM solvers to design antenna structures for optimal performance. This work leverages the results of this research program for actual design synthesis. Below we shall describe the five topics in more detail. Emphasis will be placed on our progress during the last year of the program.

Model-Based Extrapolation and Interpolation of Radiation and Scattering Data for Complex Platforms. In antenna design and analysis, the mounting platform can have significant impact on the resulting antenna radiation characteristics. Rigorous numerical solution of the radiation problem over a complex platform is very time consuming, and the computation complexity increases dramatically as the frequency increases. During the first year of this program, we developed a model-based frequency extrapolation technique, with which the radiated field over a broad band of frequencies can be obtained using rigorously computed results at low frequencies. Our approach entailed fitting the currents computed at low frequencies to a time-of-arrival model and determining the model coefficients using the superresolution algorithm ESPRIT [1]. The currents and the radiation characteristics were then extrapolated from the resulting model.

Some initial results were obtained during the first year but the accuracy of the extrapolated results was not satisfactory.

During the second year, we improved the algorithm significantly by adopting a frequency-dependent model for the induced current. The different time-of-arrival terms correspond to different incident wave mechanisms from both the direct antenna radiation and higher-order scattering from other parts of the platform. These different mechanisms in general have different frequency dependencies. For canonical platform shapes, their exact frequency dependencies are known through the geometrical theory of diffraction (GTD) [2]. However, for more complex structures, they must be determined numerically. We devised a pre-multiplication scheme in conjunction with the complex time-of-arrival estimation from ESPRIT to determine the additional frequency-dependent factors [27]. The performance of the algorithm in the presence of noise was evaluated based on simulated data and errors in the estimation of model parameters were quantified. Our results showed that the method was quite robust. The algorithm was also extended in order to simultaneously extrapolate frequency and aspect data in scattering problems [19].

We also investigated the interpolation problem for CEM data. Although the potential payoff of an interpolation algorithm is not as great as extrapolation, it provides a more robust way to achieve computational savings. To achieve the parameterization in the frequency dimension, we again utilized the multiple-arrival model for the induced current. To obtain the model parameters from the computed data, we adopted an algorithm termed adaptive feature extraction (AFE). This algorithm was originally devised by us to construct the inverse synthetic aperture radar (ISAR) image from radar measurement data that was undersampled in the aspect dimension [15]. The essential idea of the AFE algorithm is to search and extract out individual scattering features from the data set one at a time. During each iteration, the strongest feature is identified and removed from the original data. The procedure is then iterated until the data is well parameterized by the feature set. In this manner, the interference between different scattering features, which is significant for undersampled data, can be largely avoided. Since the features in our model are exponential functions of frequency and aspect, random sampling was used during the collection of the original computation data in order

to avoid the ambiguity in selecting the strongest feature. This algorithm was extended to interpolate 2-dimensional frequency and angle data [26]. In this case, a more general time-of-arrival and angle-of-arrival model was used to parameterize the current. The 2D algorithm was used in conjunction with the fast multipole code FISC [3] to predict the radar image of the benchmark VFY-218 airplane at UHF band [4]. Excellent agreement with measured data was obtained. The resulting computation time savings was about two orders of magnitude lower than the brute-force computation.

In the third year, we focused our attention on the resonant behaviors of antenna-platform configurations. This topic was motivated by the interest of the Navy SPAWAR Center in HF antennas where ship body resonances could dominate antenna frequency characteristics. In the lower frequency regime, the scattering phenomenology differs from ray-optical characteristics. Consequently, the time-of-arrival model we had utilized successfully was no longer efficient in this regime. We proposed a hybridization of the multiple-arrival model and the rational function model [21]. The AFE algorithm was again used to extract the parameters in the multiple-arrival model, while the parameters in the rational function model were obtained using the Cauchy method [5]. At each point on the target, we first parameterized the induced current using both the AFE and Cauchy algorithms separately. The model that best matched the scattering physics at that location was automatically chosen based on the resulting interpolation error. Consequently, those regions on the target that could best be described by ray-optical phenomena were interpolated by the multiple-arrival model, while those regions that exhibited resonance phenomena were interpolated by the rational function model. Numerical results for a target containing complex features were generated. It was shown that the hybrid model resulted in more accurate interpolation than either of the two models alone. Extension of this algorithm to 3-D, non-conducting targets was also attempted.

Extraction of Sparse Representation of Antenna Radiation Data. The previous topic is focused on the utilization of model-based processing to extrapolate or interpolate CEM data for the “forward” solution of electromagnetic radiation and scattering problems involving complex platforms. An equally important problem from the design perspective is the “inverse” algorithm of spatially pinpointing the locations of platform

scattering based on CEM data. During the first year, we developed a method to extract a sparse model of the antenna radiation pattern on a complex platform [17]. This representation is based on a point radiator model that describes the radiation pattern by a collection of "radiation centers" on the platform. The methodology for obtaining the radiation center model entailed first generating the 3-D antenna synthetic aperture radar (ASAR) imagery of the platform, and then parameterizing the resulting image by a collection of point radiators via the CLEAN algorithm [6]. Once such a representation was obtained, we could rapidly reconstruct antenna radiation patterns over frequencies and aspects with good fidelity. Thus such a model could be used for real-time reconstruction of complex antenna patterns in high-level system simulations. Furthermore, the resulting radiation center information could be used to pinpoint cause-and-effect in platform scattering and provide important design guidelines for antenna placement and optimization. Experimental verification of the ASAR concept was reported recently in [7].

The ASAR method is a Fourier-based algorithm that relies on a number of small-angle, small-bandwidth approximations. Furthermore, the concept was only demonstrated using high-frequency ray-tracing simulation but not more rigorous CEM data. During the second year, we overcame the above deficiencies by developing a more generalized matching pursuit algorithm [8] in the frequency-aspect domain based on a point radiator basis [18]. We also demonstrated the feasibility of extracting a sparse model of the antenna-platform interaction using CEM data from FISC. The matching pursuit algorithm was implemented based on the radiation center basis. To speed up the parameterization time of the matching pursuit algorithm, we estimated the location of the radiation centers by utilizing the Fourier-based ASAR algorithm. The point with the highest intensity was first located in the ASAR image and its amplitude and coordinates were determined to serve as an estimate of the strongest radiation center. We next zoomed in on the precise location of the radiation center via a fine search. We then subtracted the contribution of this radiation center from the total radiated field and iterated the process until the energy in the residual signal had reached a sufficiently small level. Our results showed that radiation patterns from a complex ship-like platform could be well represented by a very sparse set of radiation centers.

Finally, we also investigated ways to predict the near-field radar cross section (RCS) of a target by taking advantage of the far-field scattering centers [14]. The basic idea was to extract the far-field 3D scattering centers once and then use the strengths and positions of the extracted scattering centers to reconstruct the near-field RCS at different transceiver locations. Since the extraction was done only at the far-field range and the reconstruction could be carried out in near real-time for a variety of sensor parameters, this method is a very efficient way to generate near-field RCS data. Although only near-field monostatic scattering was considered, the method could be easily extended to handle more general bistatic scenarios.

Effect of Mutual Coupling and Platform Effects on Antenna Arrays. During the third year of this program, we initiated an investigation into mutual coupling and platform effects for antenna arrays mounted on complex platforms. First, the effect of mutual coupling on direction finding performance of circular arrays was simulated using electromagnetic computation and the MUSIC superresolution algorithm [20]. The various scenarios studied included element spacing, noise level, antenna gain and delay, and platform effects. Our results showed quantitatively the effects of mutual coupling on the direction of arrival estimates. The compensation of the coupling effect using the coupling matrix approach was also examined. This approach was found to be quite satisfactory in most cases, except when the array calibration data contained high noise level, or when strong platform effects were present.

As a follow-up to the theoretical study, we also made measurements using the 7-element circular array testbed operated by the wireless group at the University of Texas [22]. Previous experimental studies by this group using the array had shown anomalous DOA results [9]. For a single mobile user in an open field environment, the spatial spectra using the array showed a large "rebound" sidelobe not corresponding to any signal multipath or interference. In our study, we computed the array response including mutual coupling effects using the Numerical Electromagnetics Code (NEC). This computed array response was then applied to DOA estimation using measurement data collected from the antenna array. Our results showed that the rebound sidelobe was significantly reduced when mutual coupling was taken into consideration. The same

study of two co-channel mobile users was also carried out and improved DOA performance was achieved [29].

As a step toward investigating platform effects on array performance, we examined two commonly used approaches to determine the coupling matrix and their limitations [23]. The coupling matrix obtained from the minimum mean square error matching of the active and stand-alone element patterns was shown to be more effective than the mutual impedance approach. Furthermore, we proposed an extended coupling matrix model for more complex antenna arrays where parasitic elements were present. Finally, we devised a combined model to model antenna array response including both mutual coupling and platform effects [33]. The mutual coupling was described by a coupling matrix while the modification to the incident field due to the platform was modeled using the point scatterer model. A matching pursuit algorithm was employed to determine the model coefficients. Numerical results showed that the active element patterns predicted by the model were in good agreement with the rigorously simulated patterns. The advantage of the new combined model is that it provides physical insights into platform effects by pinpointing the locations of the dominant scattering mechanisms on the platform.

Improving the Speed and Accuracy of Fast Multipole Solvers. In addition to the three main topics described above, we also proposed and implemented algorithms to improve the speed and accuracy of CEM solvers based on the fast multipole method. First, we devised a new set of triangular basis functions to improve the accuracy of the traditional Rao-Wilton-Glisson (RWG) basis [10,30,32]. In the computation of surface currents and near field data, we found that the traditional RWG triangular patch basis did not provide sufficient accuracy. The basic underlying problem is that RWG basis is not complete and thus cannot represent an arbitrary linear current distribution on a patch. Subsequently, we devised an enhanced set of triangular patch basis functions. It was shown that these new basis functions provided a much better representation of the current distribution than the RWG basis while keeping the same computational complexity. In the examples we analyzed, we always obtained, for the same triangulation scheme, a better result using the new basis functions in terms of RCS prediction. In terms of current distribution, the comparative performance was even better for this new formulation. For

such application as determining the near field distribution, this set of basis functions can result in significant accuracy improvement over the traditional RWG basis. The computational complexity involved was about the same as the RWG basis. Therefore, existing computer codes can be adapted to use them with minimal modifications.

Second, we proposed a low-complexity, wavelet-based preconditioner to accelerate the convergence rate of iterative CEM solvers [25,28,34]. As pointed out earlier, ship body resonances can dominate antenna frequency characteristics in the lower frequency regime. An important problem related to the study of resonant region using an iterative CEM solver is that when the platform exhibits strong resonance effect, the iteration number required for an accurate solution can become large. A good preconditioner for the moment matrix is needed to alleviate this problem. We had previously investigated the use of wavelet packet basis for the sparsification of moment matrix [11,12]. We extended our work by devising an approximate-inverse preconditioner to the moment equation using the wavelet representation. In our approach, we constructed the approximate-inverse preconditioner in the wavelet domain where both the moment matrix and its inverse exhibit sparse, multilevel finger structures. The inversion was carried out as a Forbenius-norm minimization problem. Numerical results on a 3-D cavity showed that the iteration numbers were significantly reduced with the preconditioned system. More importantly, the computational cost of the preconditioner was kept under $O(N\log N)$, making it compatible with the fast multipole method.

Antenna Design and Optimization Using Genetic Algorithms. As an exploratory effort during the last year of the this program, we initiated a study into applying genetic algorithms (GA) for the design and optimization of antenna structures. Genetic algorithms are stochastic search methods based on the concept of natural selection and evolution. This class of algorithms is particularly attractive for finding an approximate global optimum in a very high-dimensional space. Research in the application of GA for antenna design has been ongoing since the early 1990s [13]. In contrast to a local optimization algorithm, GA allows the design space to be more fully explored (at the expense of computational cost). In the GA step, the parameters to be optimized are first encoded into a binary string known as a chromosome. Chromosomes in the population

are ranked according to a chosen cost function and a new generation of children chromosomes is produced through the rules of heredity and mutation. This process is repeated until a satisfactory set of parameters is found that best meets the design criteria.

We carried out a preliminary GA study to optimize the shape of microstrip antenna for broadband operation [24,31]. The geometry of the patch was discretized into a two-dimensional binary map and GA was used to search for the optimal patch shape that maximized bandwidth. A fast CEM code specifically tailored for microstrip structures was used. Several schemes were utilized to accelerate the convergence of the GA including 2-point crossover and geometrical filtering through the use of median filter. The optimized shape showed a four-fold improvement in bandwidth when compared to a standard square microstrip antenna. This result was verified by laboratory measurement. The basic operating principle of the optimized shape was interpreted in terms of a combination of dual-mode operation and ragged edge shape.

We also explored the use of GA for model extraction. In particular, we addressed the problem of finding the equivalent impedance boundary condition (IBC) for a corrugated material coating structure [16]. In our approach, rigorous solutions of the reflection coefficients at a number of incident angles were first calculated using a periodic method of moments (MoM) solver. The IBC model was used to predict the reflection coefficients at the same observation angles. The model coefficients were then optimized using GA so that the difference between the approximated and the MoM-predicted reflection coefficients was minimized. The genetic algorithm proved efficient in obtaining an optimal IBC model. It was also shown that the resulting IBC model could be readily incorporated into an existing CEM code to assess the performance of the corrugated coating when mounted on complex platforms.

C. FOLLOW-UP STATEMENT:

It is well known that antenna characteristics such as input impedance, mutual coupling and radiation pattern can be drastically altered by the platform that supports the antenna structure. In order that platform effects are properly accounted for, the platform must be considered together with the antenna structure during simulation and optimization. This usually makes the design process a laborious and time-consuming

task. It is therefore desirable to develop a systematic framework where such design processes are highly streamlined. It is with this goal that we have carried out our research under the H-infinity Program. To accelerate repeated CEM calculations over large parameter spaces such as frequency, position and aspect angle, we have developed a number of model-based extrapolation/interpolation algorithms to populate the antenna characteristics data based on a very sparse set of CEM calculations. We have also developed algorithms to extract sparse models of the relevant physics embedded in the CEM data to facilitate design and synthesis.

In the follow-on research program, we shall move on to explore the use of genetic algorithms (GA) for shipboard antenna design, placement and optimization. Three problems of relevance to shipboard antenna design will be addressed. First, we propose to investigate the optimal design of electrically small wire antennas in the low HF frequency range, where the mounting platform plays a prominent role. Second, we propose to study the antenna array synthesis and placement problem in the presence of mutual coupling and platform effects. Third, we propose to investigate the shape design of microstrip antenna elements for broadband, wide-angle scanning array applications. While GA is an efficient global optimizer ideally suited for exploring very complex design problems such as those outlined above, it typically requires a very large number of cost function evaluations. We will leverage off our existing research to minimize the number of CEM calculations needed for cost function computation. Particular attention will be paid to the close coupling between GA and the CEM simulator to establish a framework in which the design process can be streamlined. The potential impact of the proposed research is that novel design concepts will be uncovered that can significantly outperform conventional designs for shipboard antenna problems.

D. REFERENCES:

1. R. Roy, A. Paulraj and T. Kailath, "ESPRIT – a subspace rotation approach to estimation of parameters of cisoids in noise," *IEEE Trans. Acoust., Speech, Signal Processing*, vol. ASSP-34, pp. 1340-1342, Oct. 1986.
2. L. C. Potter, D. Chiang, R. Carriere and M. J. Gerry, "A GTD-based parametric model for radar scattering," *IEEE Trans. Antennas Propagat.*, vol. 43, pp. 1058-1067, Oct. 1995.

3. J. Song, C. C. Lu and W. C. Chew, "Multilevel fast multipole algorithm for electromagnetic scattering by large complex objects," *IEEE Trans. Antennas Propagat.*, vol. 45, no. 10, pp. 1488-1493, Oct. 1997.
4. H. T. G. Wang, M. L. Sanders and A. Woo, "Radar cross section measurement data of the VFY 218 configuration," *Tech. Rept. NAWCWPNS TM-7621*, Naval Air Warfare Center, China Lake, CA, Jan. 1994.
5. R. S. Adve, T. K. Sarkar, D. M. Rao, E. K. Miller, and D. R. Pflug, "Application of the Cauchy method for extrapolating/interpolating narrow band system responses," *IEEE Trans. Microwave Theory Tech.*, vol. 45, pp. 837-845, May 1997.
6. J. Tsao and B.D. Steinberg, "Reduction of sidelobe and speckle artifacts in microwave imaging: the CLEAN technique," *IEEE Trans. Antennas Propagat.*, vol. AP-36, pp. 543-556, Apr. 1988.
7. T. H. Chu, "Microwave diversity imaging using ASAR approach," International IEEE Antennas and Propagation Symposium, Salt Lake City, UT, July 2000.
8. S. G. Mallat and Z. Zhang, "Matching pursuit with time-frequency dictionaries," *IEEE Trans. Signal Processing*, vol. 41, pp. 3397-3415, Dec. 1993.
9. A. Kavak, *Vector Propagation Channel Studies for Smart Antenna Wireless Communication Systems*, Ph.D. Dissertation, The University of Texas at Austin, Jan. 2000.
10. S. M. Rao, D. R. Wilton, and A. W. Glisson, "Electromagnetic scattering by surfaces of arbitrary shape," *IEEE Trans. Antennas Propagat.*, vol. 30, pp. 409-418, May 1982.
11. H. Deng and H. Ling, "Fast solution of electromagnetic integral equations using adaptive wavelet packet transform," *IEEE Trans. Antennas Propagat.*, vol. AP-47, pp. 674-682, Apr. 1999.
12. H. Deng and H. Ling, "On a class of pre-defined wavelet packet bases for efficient representation of electromagnetic integral equations," *IEEE Trans. Antennas Propagat.*, vol. AP-47, pp. 1772-1779, Dec. 1999.
13. Y. Rahmat-Samii and E. Michielssen, *Electromagnetic Optimization by Genetic Algorithms*, John Wiley & Sons: New York, 1999.

E. PUBLICATIONS:

I. LIST OF JOURNAL ARTICLES (ONR supported in whole or in part)

14. R. Bhalla and H. Ling, "Near-field signature prediction using far-field scattering centers extracted from the shooting and bouncing ray technique," *IEEE Trans. Antennas Propagat.*, vol. AP-48, pp. 337-338, February 2000.
15. Y. Wang and H. Ling, "Adaptive ISAR image construction from unevenly undersampled data," *IEEE Trans. Antennas Propagat.*, vol. AP-48, pp. 329-331, February 2000.
16. T. Su and H. Ling, "Determining the equivalent impedance boundary condition for corrugated coatings based on the genetic algorithm," *IEEE Trans. Antennas Propagat.*, vol. AP-48, pp. 374-382, March 2000.
17. C. Ozdemir, R. Bhalla and H. Ling, "A radiation center representation of antenna radiation pattern on a complex platform," *IEEE Trans. Antennas Propagat.*, vol. AP-48, pp. 992-1000, June 2000.
18. T. Su, C. Ozdemir and H. Ling, "On extracting the radiation center representation of antenna radiation patterns on a complex platform," *Microwave Optical Tech. Lett.*, vol. 26, pp. 4-7, July 2000.
19. Y. Wang and H. Ling, "A frequency-aspect extrapolation algorithm for ISAR image simulation based on two-dimensional ESPRIT," *IEEE Trans. Geo. Science and Remote Sensing*, vol. 38, pp. 1743-1748, July 2000.
20. T. Su, K. Dandekar and H. Ling, "Simulation of mutual coupling effect in circular arrays for direction finding applications," *Microwave Optical Tech. Lett.*, vol. 26, pp. 331-336, September 2000.
21. B. Jiang, T. Su and H. Ling, "Frequency interpolation of electromagnetic scattering data using a hybrid model," *Microwave Optical Tech. Lett.*, vol. 27, pp. 307-312, December 2000.
22. K. R. Dandekar, H. Ling and G. Xu, "The effect of mutual coupling on direction finding in smart antenna applications," to appear in *Elect. Lett.*, December 2000.
23. T. Su and H. Ling, "On modeling mutual coupling in antenna arrays using the coupling matrix," to appear in *Microwave Optical Tech. Lett.*, February 2001.
24. H. Choo, A. Hutani, L. C. Trintinalia and H. Ling, "Shape optimization of broadband microstrip antennas using the genetic algorithm," accepted for publication in *Elect. Lett.*, November 2000.
25. H. Deng and H. Ling, "A wavelet-based preconditioner for three-dimensional electromagnetic integral equations," accepted for publication in *Elect. Lett.*, November 2000.

26. Y. Wang and H. Ling, "Efficient radar signature prediction using a frequency-aspect interpolation technique based on adaptive feature extraction," submitted for publication in *IEEE Trans. Antennas Propagat.*, June 1999.
27. T. Su, Y. Wang and H. Ling, "A frequency extrapolation technique for computing antenna-platform radiation problems," submitted for publication in *IEEE Trans. Antennas Propagat.*, September 1999.
28. H. Deng and H. Ling, "An efficient preconditioner for electromagnetic integral equations using pre-defined wavelet packet basis," submitted for publication in *IEEE Trans. Antennas Propagat.*, November 1999.
29. K. R. Dandekar, H. Ling and G. Xu, "Experimental study of mutual coupling compensation in smart antenna applications," submitted for publication in *IEEE Trans. Communications*, August 2000.
30. L. C. Trintinalia and H. Ling, "Enhanced triangular patch basis functions for electromagnetic scattering analysis," submitted for publication in *IEEE Trans. Antennas Propagat.*, October 2000.

II. LIST OF CONFERENCE PROCEEDINGS (ONR supported in whole or in part)

31. H. Choo, T. Su, L. C. Trintinalia and H. Ling, "Shape optimization of printed patch structures using the genetic algorithm," URSI National Radio Science Meeting, p. 78, Salt Lake City, UT, July 2000.
32. L. C. Trintinalia and H. Ling, "An improved triangular patch basis for the method of moments," International IEEE AP-S Symposium, pp. 2306-2309, Salt Lake City, UT, July 2000.
33. T. Su and H. Ling, "A model for the active element pattern of array elements including both mutual coupling and platform effects," International IEEE AP-S Symposium, pp. 2130-2133, Salt Lake City, UT, July 2000.
34. H. Deng and H. Ling, "A wavelet-packet based preconditioner for iterative solution of electromagnetic integral equations," International IEEE AP-S Symposium, pp. 1810-1813, Salt Lake City, UT, July 2000.

III. LIST OF RELATED PRESENTATIONS

35. "Scattering from periodic surfaces – analysis, design and optimization," Lockheed Fort Worth Company, Fort Worth, Texas, April 10, 2000.

36. "Fast postprocessing algorithms for fast CEM solvers," 2000 Electromagnetics Code Consortium Annual Meeting, Boeing Phantomworks, St. Louis, Missouri, May 9, 2000.
37. "Application of model-based signal processing for antenna design, placement and optimization," Navy H-Infinity Program Workshop, US Naval Academy, Annapolis, Maryland, October 26, 2000.

IV. LIST OF THESES AND DISSERTATIONS

Ph.D.

I. Y. Kelly, "The multipath fingerprint method for wireless E-911 location finding," May 2000.

H. Deng, "Applications of wavelet packet bases to computational electromagnetics and radar imaging," August 2000.

M.S.

J. A. Dobbins, "Folded conical helix antenna," May 2000.

B. Jiang, "Model-based interpolation algorithms for electromagnetic scattering by complex objects," May 2000.

H. Choo, "Shape optimization of printed patch structures using the genetic algorithm," August 2000.

V. CONTRACTS AND GRANTS

H. Ling, "Application of model-based signal processing methods to computational electromagnetics simulators," Office of Naval Research, December 1, 1997 - November 30, 2000.

H. Ling, "MURI center for computational electromagnetics research," Air Force Office of Scientific Research (via Univ. of Illinois), December 15, 1995 - December 14, 2000.

H. Ling, "Radar image enhancement, feature extraction and motion compensation using joint time-frequency techniques," Office of Naval Research, April 15, 1998 - September 30, 2001.

H. Ling, "Electromagnetic scattering from periodic surfaces," Lockheed Martin Corporate Grant, November 15, 1998 - December 31, 1999.

D. T. Jaffe and H. Ling, "High index grisms for mid-infrared spectroscopy," NASA, June 1, 1999 - May 31, 2001.

G. Xu, H. Ling and H. D. Foltz, "Development of wideband vector channel models and testbed for 3rd generation wireless mobile systems," Texas Advanced Technology Program, January 1, 2000 - December 31, 2001.

F. INTERACTIONS/COLLABORATIONS WITH NAVY SCIENTISTS:

The third H-infinity workshop was held at the Naval Academy on October 26, 2000. In addition to reporting our progress and exchanging ideas with the other team members of the H-infinity program, new collaborative opportunities were explored. We continue to interact closely with Dr. Victor Chen of Naval Research Lab on a separate ONR program in applying joint time-frequency processing to inverse synthetic aperture radar imagery. We expect to generate cross-fertilization of ideas with the H-infinity program since a good physical understanding of electromagnetic scattering and radiation phenomena is the basis of our work in both programs.

G. NEW DISCOVERIES, INVENTIONS, OR PATENT DISCLOSURES:

None.

H. HONORS AND AWARDS:

None.

APPENDIX

Publications Supported by ONR Grant

Near-Field Signature Prediction Using Far-Field Scattering Centers Extracted from the Shooting and Bouncing Ray Technique

Rajan Bhalla and Hao Ling

Abstract—We present a technique to predict the near-field radar cross section (RCS) of a target using the far-field scattering centers extracted from the shooting and bouncing ray (SBR) technique. The results generated using this methodology are verified against the brute-force SBR calculations for near-field scenarios. It is demonstrated that this technique is a fairly accurate and very efficient way to generate near-field RCS data provided that the transceiver is not very close to the target.

Index Terms—Radar, ray shooting, scattering centers, target identification.

I. INTRODUCTION

For many radar applications the transmitting and receiving antennas are located in the near-field zone of the target. Under this situation, the distance between the transmitting antenna and the target may not be large enough to treat the incident field arriving at the target as a plane wave. Similarly, the distance between the receiving antenna and the target may not be large enough to treat the scattered field arriving at the receiver as a plane wave. Hence, the far-field assumption is not valid and a near-field analysis is necessary. One of the existing methodologies to compute near-field radar cross section (RCS) is to use the shooting and bouncing ray (SBR) technique [1], [2]. In the SBR technique, rays are launched at the target from the phase center of the transmitting antenna and are traced according to the law of geometrical optics. At the exit point of each ray, a ray-tube integration is performed to find its contribution to the total scattered field at the receiving antenna, taking into account of the distance from the ray tube to the receiver location. Although the SBR methodology is straightforward, for typical radar applications the problem involved often contains a large number of parameter combinations. For example, in typical missile engagement simulations, the scattered field is of interest at different transceiver locations and for different antenna patterns. Each combination is a new problem and requires that the whole computation be carried out each time. This can lead to an inordinately large amount of computation time. In this letter, we present a technique to predict the near-field RCS of a target by taking advantage of the far-field scattering centers extracted using the existing capability of the SBR technique [3], [4]. The basic idea is to extract the far-field three-dimensional (3-D) scattering centers once and then use the strengths and positions of the extracted scattering centers to reconstruct the near-field RCS at different transceiver locations. Since the extraction is done only at the far-field range and the reconstruction can be carried out very quickly, this methodology is potentially a very efficient way to compute near-field RCS.

II. NEAR-FIELD RCS PREDICTION USING FAR-FIELD SCATTERING CENTERS

It is well known that the scattered far field from an electrically large target can be modeled by a discrete set of scattering centers on the

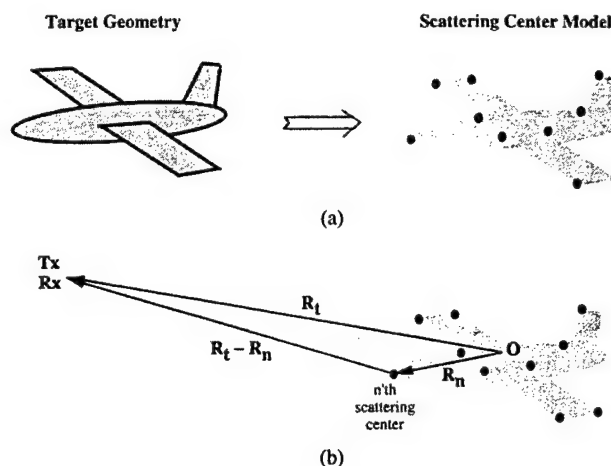


Fig. 1. (a) Three-dimensional far-field scattering center model of a target. (b) Near-field RCS prediction based on far-field scattering centers.

target [see Fig. 1(a)]. The monostatic 3-D scattering centers at a given incident direction can be sparsely represented by a set of numbers $\{A_n, R_n\}$, where A_n is the strength of a scattering center and R_n is its 3-D location. The 3-D scattering center extraction methodology of a target using the SBR technique has been developed recently in [3] and [4]. To predict near-field data using the far-field scattering centers, we argue that each scattering center models the interaction between the incident electromagnetic wave and a localized portion of the target. The portion of the target that gives rise to each scattering center is much smaller than the whole target. Consequently, the scattering phenomenon represented by each scattering center is expected to be valid at a distance much closer than the usual far-field range criterion of $L = 2D^2/\lambda$, where D is the maximum target dimension and λ is the wavelength. At very closed-in ranges the scattering centers themselves will be defocused and this interpretation may no longer be valid.

Next, we provide the formula to reconstruct the monostatic near-field from the monostatic far-field scattering centers. To reconstruct the scattered field, E^s at a frequency f for a transceiver located at R_t , we sum up the contribution of each scattering center as [see Fig. 1(b)]

$$E^s(f, R_t) = \sum_n A_n \exp\left(-j \frac{4\pi f}{c} |R_t - R_n|\right) \cdot \left\{ \frac{R_t^2}{|R_t - R_n|^2} \right\} \quad (1)$$

Notice that in addition to the phase term to take into account of the near-field effect, we also use a range correction for the amplitude of each scattering center. The scattered field defined in (1) has been normalized so that it will reduce to the far-field RCS as R_t approaches the far-field range [5], [6]. If the antenna pattern is not isotropic, the effect of the antenna pattern can also be accounted for in (1). In addition, although only the monostatic scattering is considered in this paper, the methodology is extendible to the more general bistatic scenario. It should also be noted that the reconstruction in (1) is based on single-bounce scattering mechanisms and is not very accurate for scattering centers whose contribution comes from high multibounce mechanism.

III. RESULTS

Two numerical examples are presented to demonstrate the accuracy of this technique. The reconstructed near-field RCS from far-field scattering centers is compared to the brute-force SBR results as a function

Manuscript received December 31, 1997.

R. Bhalla was with the University of Texas at Austin, Austin, TX 78712-1084 USA. He is now with SAIC-DEMCO, Boston, MA 01880 USA.

H. Ling is with the Department of Electrical and Computer Engineering, the University of Texas at Austin, Austin, TX 78712-1084 USA.

Publisher Item Identifier S 0018-926X(00)01282-5.

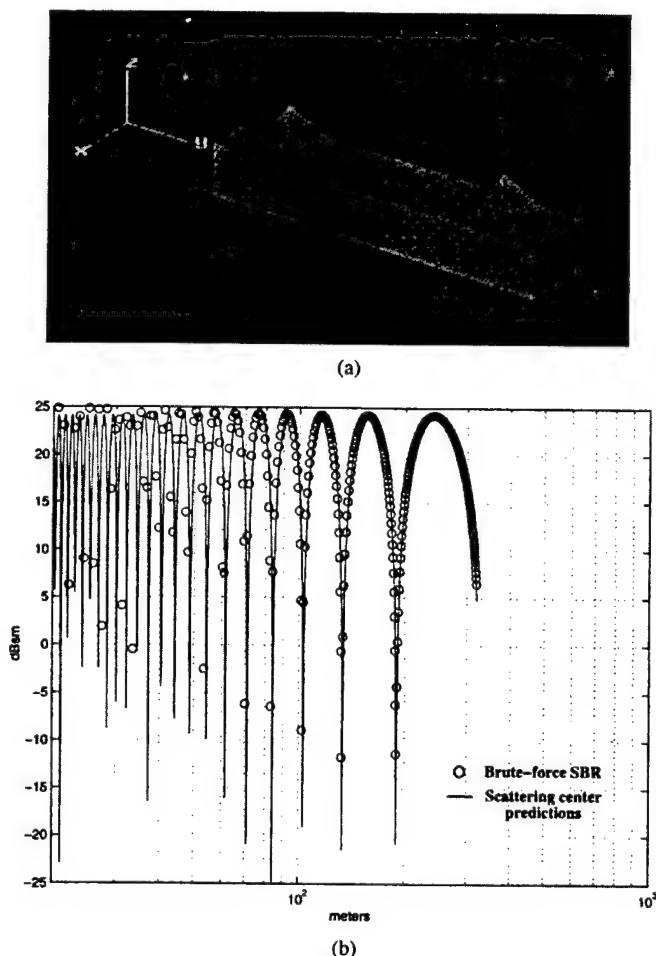


Fig. 2. Comparison of the near-field RCS computed by brute-force SBR and by scattering center prediction for a conical target. (a) Target geometry. (b) Near-field RCS versus range.

of range of the transceiver. The antenna pattern of the transceiver is assumed to be isotropic and horizontally polarized. The first example is a simple canonical target comprising of two triplates mounted on an elongated box as shown in Fig. 2(a). The monostatic 3-D scattering centers are extracted at an incident azimuth angle of -15° and an elevation angle of 15° . The far-field criterion for this 3-m target is 760 m at 12.65 GHz. The near-field RCS is computed as the transceiver is moved closer to the target at the same fixed incident angle of $(-15^\circ, 15^\circ)$ and the range was varied from 320 to 15 m. Fig. 2(b) shows the near-field RCS comparison between the brute-force computation and the scattering center reconstruction plotted on a logarithmic scale of the range. The agreement between the two profiles is very good, even up to a very closed-in range of 50 m. The pattern observed in the RCS profile is consistent with the beating of two strong scattering centers at the two triplate positions.

The second example is a full-size airplane. The monostatic 3-D scattering centers are extracted at an incident (AZ, EL) angle of $(120^\circ, -18^\circ)$. The far-field distance for this 20-m target is 27 000 m at 10 GHz. The near-field RCS is computed as the transceiver is moved closer to the target at the same fixed incident angle of $(120^\circ, -18^\circ)$ and the range was varied from 25 000 to 200 m. Fig. 3 shows the near-field RCS comparison between the brute-force SBR computation and the scattering center reconstruction plotted on a logarithmic scale of range. Even though this target has some multibounce returns from inlet ducts whose reconstruction will not be very accurate using scattering center predictions, the reconstructed RCS captures the salient feature of the brute-

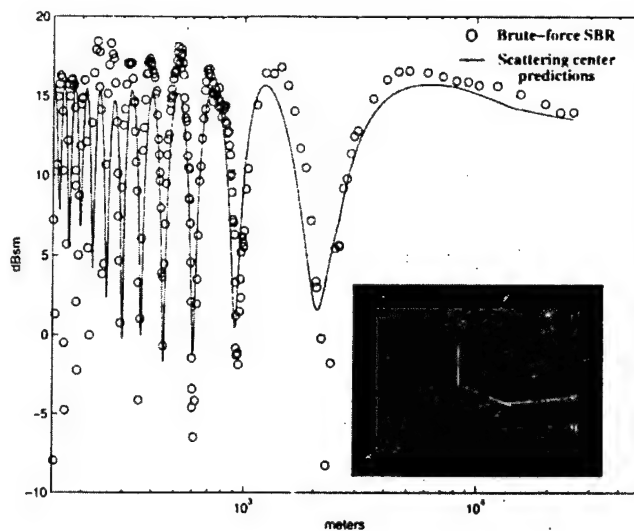


Fig. 3. Comparison of the near-field RCS computed by brute-force SBR and by scattering center prediction for a full-size airplane.

force SBR computation. The comparison degrades as we get closer to the target. In terms of computation time, the brute-force computation takes roughly 30 min/range point on an SGI R4400 workstation. The scattering center extraction itself can be carried out in about 30 min. Once the scattering centers are extracted, however, the reconstruction can be done in seconds at all the range values. Hence, the scattering centers offer tremendous computation time savings for the computation of near-field RCS.

IV. CONCLUSION

In this paper, we presented an efficient technique to predict near-field RCS using far-field scattering centers extracted from the SBR technique. Such a scheme allows us to generate the near-field RCS in real time for a variety of input parameters such as range and antenna patterns. For very closed-in ranges, however, this scheme is expected to break down as the scattering centers become defocused. In addition, such prediction is based on single-bounce scattering and will not be as accurate for multibounce returns. Although only near-field monostatic scattering is considered in this paper, the methodology can be extended to handle more general bistatic scenarios.

REFERENCES

- [1] C. L. Yu, R. Kipp, D. J. Andersh, and S. W. Lee, "Near-field electromagnetic modeling and analysis," in *IEEE Antennas Propagat. Symp. Dig.*, Montreal, Canada, July 1997, pp. 1168–1171.
- [2] S. K. Jeng, "Near-field scattering by physical theory of diffraction and bouncing rays," in *1997 IEEE Antennas Propagat. Symp. Dig.*, Montreal, Canada, July 1997, pp. 1176–1179.
- [3] R. Bhalla and H. Ling, "3-D scattering center extraction using the shooting and bouncing ray technique," *IEEE Trans. Antennas Propagat.*, vol. 44, pp. 1445–1453, Nov. 1996.
- [4] R. Bhalla, J. Moore, and H. Ling, "A global scattering center representation of complex targets using the shooting and bouncing ray technique," *IEEE Trans. Antennas Propagat.*, vol. 45, pp. 1850–1856, Dec. 1997.
- [5] S. W. Lee and S. K. Jeng, *NcPTD 1.2—A High Frequency Near-Field RCS Computation Code Based on Physical Theory of Diffraction*. Champaign, IL: DEMACO Inc., June 1991, vol. 6.
- [6] J. M. Taylor and A. J. Terzuoli, "On the concept of near-field radar cross section," in *1997 IEEE Antennas Propagat. Symp. Dig.*, Montreal, Canada, July 1997, pp. 1172–1175.

Adaptive ISAR Image Construction from Nonuniformly Undersampled Data

Yuanxun Wang and Hao Ling

Abstract—An adaptive approach is proposed to construct ISAR images from nonuniformly undersampled data in the angular domain. The algorithm uses an adaptive scattering feature extraction engine in place of the Fourier transform in the image construction procedure. The algorithm entails searching and extracting out individual target scattering features one at a time in an iterative fashion. The interference between different target scattering features is thus avoided and a clean ISAR image without the aliasing effect can be obtained. The algorithm is verified by constructing the ISAR image from the chamber measurement data of the model VFY-218 airplane.

Index Terms—Image reconstruction, synthetic aperture radar.

I. INTRODUCTION

Constructing an inverse synthetic aperture radar (ISAR) image of a target requires data collection in both the frequency and angular dimensions. If the data are uniformly sampled and the sampling rate is dense enough, an ISAR image can be obtained by using a two-dimensional (2-D) fast Fourier transform (FFT) algorithm [1]. In this paper, we address the case when the angular data are nonuniformly undersampled. This scenario may arise in real-world data collection when the target is fast maneuvering with respect to the radar pulse repetition interval so that the angular look on the target by the radar is not dense enough to satisfy the Nyquist sampling rate. We propose an algorithm to overcome the aliasing effect in the cross-range dimension and construct ISAR images from seriously undersampled data. The algorithm uses an adaptive scattering feature extraction engine in place of the Fourier transform in the image construction process. The original concept of adaptive feature extraction was proposed in [2] and [3]. It has been applied to ISAR image processing in the joint time-frequency space for resonant scattering mechanism extraction [4], target motion compensation [5], and Doppler interference removal [6]. In contrast to the Fourier transform, where the signal is projected to all the image-domain bases simultaneously, the adaptive algorithm searches and extracts the individual target scattering features one at a time in an iterative fashion. When applied to the present problem, the aliasing error caused by the interference between different target scattering features can be avoided. Therefore, after all the main features are extracted, they can be displayed in the ISAR image plane without the aliasing effect. We verify this algorithm by constructing the ISAR image using the chamber measurement data of the model VFY-218 airplane [7]. It is found that a reasonable ISAR image can be constructed from seriously undersampled data.

II. ADAPTIVE FEATURE EXTRACTION (AFE) ALGORITHM

In standard ISAR image construction, the target is assumed to be a collection of point scattering centers. Under the small-angle approx-

Manuscript received January 4, 1999; revised August 10, 1999. This work was supported by the Air Force MURI Center for Computational Electromagnetics under Contract AFOSR F49620-96-1-0025 and the Office of Naval Research under Contract N00014-98-1-0178 and N00014-98-1-0615.

The authors are with the Department of Electrical and Computer Engineering, The University of Texas at Austin, Austin, TX 78712-1084 USA.

Publisher Item Identifier S 0018-926X(00)01656-2.

imation, the scattered field from the target observed as a function of frequency and angle can be written as

$$\begin{aligned} E(f, \theta) &= \sum_{i=1}^N O(x_i, y_i) e^{-2jk_x x_i \cos \theta - 2jk_y y_i \sin \theta} \\ &\cong \sum_{i=1}^N O(x_i, y_i) e^{-2jk_x x_i - 2jk_c y_i} \end{aligned} \quad (1)$$

where $O(x_i, y_i)$ is the amplitude of the i th scattering center, k is the free-space wave number, and k_c corresponds to the wave number at the center frequency. x_i and y_i denote the down range and cross-range dimensions, respectively. We assume that the sampling in frequency is uniformly spaced and dense enough to satisfy the Nyquist criterion since it is completely controlled by the radar. Thus, the range profile versus angle data can be generated from the frequency-aspect data by applying a one-dimensional (1-D) Fourier transform along the frequency dimension. We shall denote the result as $R(x, \theta)$

$$R(x, \theta) = \sum_{i=1}^N O(x_i, y_i) S_x(x - x_i) e^{-2jk_c y_i \theta}. \quad (2)$$

In the above expression, $S_x(x - x_i)$ is the down-range point spread function due to the finite-length frequency domain data. Similarly, the cross-range information can also be obtained from angular data via a 1-D Fourier transform of $R(x, \theta)$ along the angular dimension. The resulting image $I(x, y)$ is

$$\begin{aligned} I(x, y) &= \int R(x, \theta) e^{2jk_c y \theta} d\theta \\ &= \sum_{i=1}^N O(x_i, y_i) S_x(x - x_i) \int e^{2jk_c \theta (y - y_i)} d\theta \\ &= \sum_{i=1}^N O(x_i, y_i) S_x(x - x_i) S_y(y - y_i) \end{aligned} \quad (3a)$$

where

$$S_y(y - y_i) = \int e^{2jk_c \theta (y - y_i)} d\theta \quad (3b)$$

is the cross-range point spread function due to the finite-length angular domain data. If the data are sampled densely enough such that the numerical integration can be carried out accurately, the point-spread function S_y should be a well-localized function with its peak at y_i , while rapidly decaying away from the peak. The resulting image $I(x, y)$ will be a clean image with good indication of the amplitudes and positions of the target point scattering features. However, when the data are undersampled, the numerical integration in (3b) will result in large aliasing error that shows up as high sidelobes in S_y . Consequently, the constructed image will contain strong interference between the scattering features. This effect can be interpreted as the loss of orthogonality of the Fourier bases under the undersampled condition.

In the proposed approach, we use an adaptive feature extraction algorithm in place of the Fourier processing. Instead of projecting the signal onto all the exponential bases simultaneously, we search out the strongest point scattering feature in the cross-range domain and remove it from the original signal. Then the search is repeated for the remainder signal and the point-scattering features are extracted one at a time until the energy of the residue signal is smaller than a preset threshold. The search procedure is carried out by calculating the integral in (3b) for all points in cross range but saving only the maximum value and position, i.e.,

$$[B_p, y_p] = \max_{y_p} [I_p(x, y)] \quad (4)$$

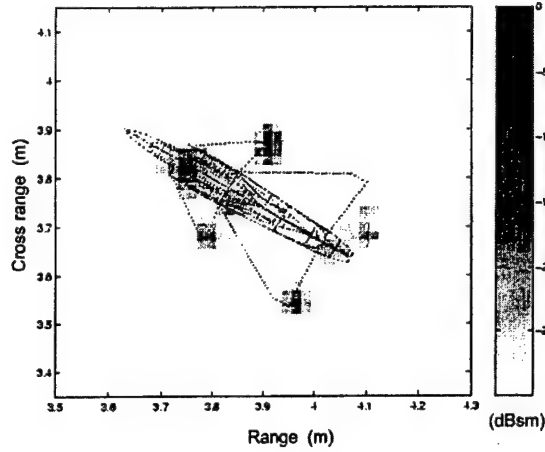


Fig. 1. The ISAR image constructed at 30° azimuth from the original data using FFT.

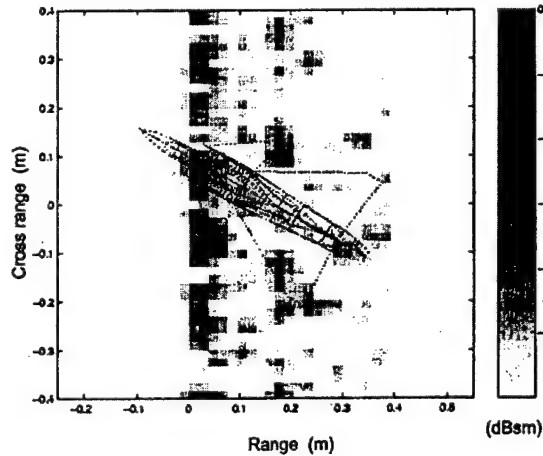


Fig. 2. The ISAR image constructed at 30° azimuth from randomly undersampled data using Fourier transform.

where p denotes the stage of the iterative procedure. The remainder signal is produced by subtracting out the p th feature

$$R_{p+1}(x, \theta) = R_p(x, \theta) - B_p e^{-2jk_c y_p \theta}. \quad (5)$$

The convergence of the above procedure is guaranteed and the mathematical proof is given in [2]. The advantage of such an iterative procedure is that each time we extract out the strongest feature, we also eliminate its interference on the other features. It should be noted that nonuniform sampling is a prerequisite to ensure that there is no ambiguity in the strongest features since uniformly undersampled data will result in multiple positions of the strongest features. For simplicity, the algorithm is repeated for each range cell of the image. A 2-D algorithm in frequency and aspect can also be developed, if the search is carried out for both the range and cross-range parameters. After all the features are extracted out, we can construct an ISAR image using the amplitudes and positions of the point scatterers.

III. RESULTS AND DISCUSSION

To examine the applicability of the algorithm on real target scattering data, we reconstruct the radar image of a model (1 : 30 scale) VFY-218 airplane using undersampled chamber measurement data [7]. The measurement data consist of an aspect window from 10° to 50° and a frequency range from 8 to 16 GHz. To construct an ISAR image, we first

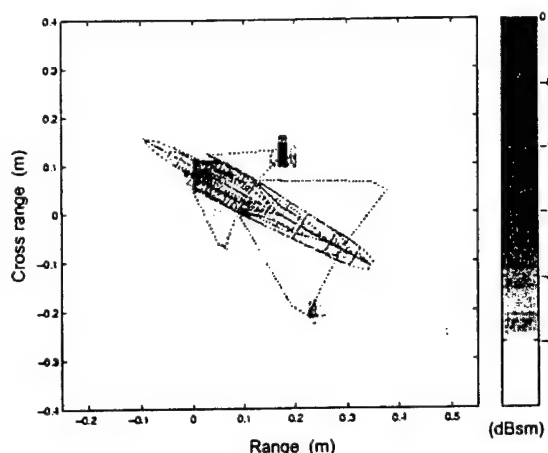


Fig. 3. The ISAR image constructed at 30° azimuth from randomly undersampled data using the AFE algorithm.

polar reformat the frequency-aspect data to the (K_x, K_y) space. The reformatted data consist of 401 samples in K_x and 438 samples in K_y . The ISAR image is first generated by fast Fourier transform (FFT) and shown with the airplane overlay in Fig. 1. The point-scattering features can clearly be seen. Next, we test our algorithm by generating an undersampled data set in K_y . This is approximately the same as undersampling in angle. (Note that for full size targets, this approximation gets better.) The Nyquist sampling rate requires about 36 sampling points in K_y and we randomly select only 24 out of the 438 points. The maximum sampling interval used is about four times the size of the Nyquist sampling interval. Therefore, serious aliasing will occur if the Fourier transform algorithm is used, as shown by the ISAR image displayed in Fig. 2. All the features are overlapped with sidelobe noise such that the point scattering features on the airplane can no longer be distinguished. Next, we apply the adaptive feature extraction (AFE) algorithm to each range cell of the image. The image is reconstructed and shown in Fig. 3. Comparing Fig. 3 with Fig. 1, we can see the main features of the airplane in Fig. 3 are all well reconstructed in Fig. 1. We do observe some noisy spots outside the target at the lower dynamic ranges in Fig. 3. This low-level noise occurs at about 25 dB down from the key features and presents a dynamic range limitation of the present AFE algorithm. The algorithm has also been tested on measured data from in-flight targets with good success.

REFERENCES

- [1] D. A. Ausherman, A. Kozma, J. L. Walker, H. M. Jones, and E. C. Poggio, "Developments in radar imaging," *IEEE Trans. Aerosp. Electron. Syst.*, vol. AES-20, pp. 363-400, July 1984.
- [2] S. Qian and D. Chen, "Signal regression using adaptive normalized Gaussian functions," *Signal Processing*, vol. 36, pp. 1-11, Mar. 1994.
- [3] S. G. Mallat and Z. Zhang, "Matching pursuits with time-frequency dictionaries," *IEEE Trans. Signal Processing*, vol. 41, pp. 3397-3415, Dec. 1993.
- [4] L. C. Trintinalia and H. Ling, "Joint time-frequency ISAR using adaptive processing," *IEEE Trans. Antennas Propagat.*, vol. 45, pp. 221-227, Feb. 1997.
- [5] Y. Wang, H. Ling, and V. C. Chen, "ISAR motion compensation via adaptive joint time-frequency techniques," *IEEE Trans. Aerosp. Electron. Syst.*, vol. 34, pp. 670-677, Apr. 1998.
- [6] —, "Application of adaptive joint time-frequency processing to ISAR image enhancement and Doppler feature extraction for targets with rotating parts," in *SPIE Proc. Radar Processing, Technol. Applicat.* San Diego, CA, July 1998, vol. 3462.

Determining the Equivalent Impedance Boundary Condition for Corrugated Coatings Based on the Genetic Algorithm

Tao Su, *Student Member, IEEE*, and Hao Ling

Abstract—A methodology based on the genetic algorithm (GA) is proposed to determine the equivalent impedance boundary condition (IBC) for corrugated material coating structures. In this approach, rigorous solutions of the reflection coefficients at a number of incident angles are first calculated using a periodic method of moments (MoM) solver. The IBC model is used to predict the reflection coefficients at the same observation angles. The model coefficients are then optimized using the GA so that the difference between the approximated and the MoM predicted reflection coefficients is minimized. The GA proves efficient in obtaining an optimal IBC model. The resulting IBC model can be readily incorporated into an existing computational electromagnetics code to assess the performance of the corrugated coating when mounted on complex platforms.

Index Terms—Coatings, genetic algorithm, gratings, impedance boundary conditions.

I. INTRODUCTION

IT is well known that the impedance boundary condition (IBC) approximation is an efficient way to model complex structures such as material coatings and subskinline features [1]–[3]. It replaces the original volumetric structure with a surface impedance so that the problem dimension is reduced by one. Thus, large savings in computational resources can be achieved in the analysis of the original problem. However, to determine a simple IBC for an arbitrary structure that is valid over a wide range of incident angles, polarizations and frequencies is a nontrivial task. In this paper, we set out to develop a methodology to determine the equivalent IBC model for a corrugated coating structure backed by a conducting surface (see Fig. 1). The corrugation of the surface is assumed to be periodic in one dimension along the x -axis. Of interest is an IBC model that is valid over a large range of incident angles in both the θ and ϕ directions. Our objective is to establish a robust methodology such that the resulting IBC model can be used in place of the actual coating structure in subsequent analysis and design involving complex platforms.

The problem at hand is difficult since the scattering characteristics of the corrugated surface is strongly dependent on po-

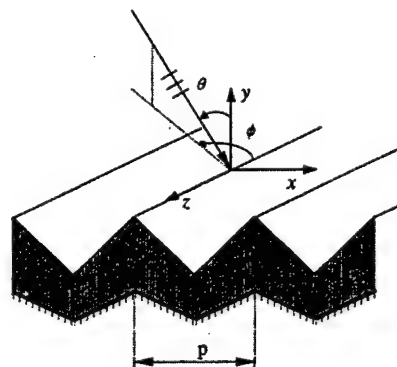


Fig. 1. Scattering from a corrugated coating structure backed by a conducting surface.

larization and incident angle. The standard IBC used for flat coatings accounts for neither the anisotropic nor the angular behavior of the scattering characteristics of the corrugated surface. Some improved impedance boundary conditions have been proposed in the literature, including the tensor impedance boundary condition (TIBC) [1] and the generalized impedance boundary condition (GIBC) [2], [4]. TIBC usually works only for a very limited range of incident angles. GIBC improves the accuracy of the IBC model by including higher order derivatives of the fields on the surface. However, it cannot be easily implemented in existing MoM solvers since it requires further reformulation in the integral equation. A resistive boundary condition (RBC) has been reported that works well over large incident angles for two-dimensional (2-D) planar periodic surfaces [5]. However, it is limited to surfaces with very small periods. Furthermore, the choice for the position of the equivalent impedance surface is not obvious for the corrugated structure.

Our proposed approach to this problem is based on the genetic algorithm (GA). First, we compute the reflection coefficients from the corrugated surface over a number of incident angles and polarizations using a periodic method of moments (MoM) solver [6]. The resulting reflection coefficients constitute our reference data base. Next, a simple periodic IBC model is proposed from which we can derive an expression for the reflection coefficients. In the GA step, we optimize the model coefficients so that the difference between the IBC-predicted and the MoM-predicted reflection coefficients is minimized. GA searches the entire parameter space in a way similar to natural evolution and arrives, after many generations, at the best parameters for the model.

Manuscript received May 26, 1998; revised August 10, 1999. This work was supported by a Lockheed Martin Cooperation Research Grant; in part by the Air Force MURI Center for Computational Electromagnetics under Contract AFOSR F49620-96-1-0025; and in part by the Office of Naval Research under Contract N00014-98-1-0178.

The authors are with the Department of Electrical and Computer Engineering, University of Texas at Austin, Austin, TX 78712 USA.

Publisher Item Identifier S 0018-926X(00)02452-2.

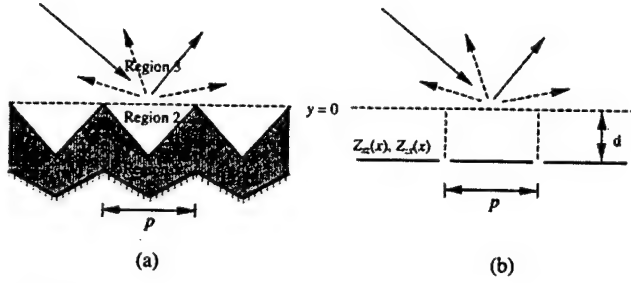


Fig. 2. Equivalent impedance boundary problem, (a) Original structure, (b) IBC Approximation.

This paper is organized as follows. In Section II, the MoM solution of the problem, the IBC model formulation and the GA optimization are discussed as the steps of the IBC determination. Numerical results are provided in Section III to verify the effectiveness of the approach in a number of corrugated geometries. A 3-D scattering example is also given to demonstrate the utility of the resulting IBC model.

II. METHODOLOGY FOR DETERMINING THE OPTIMAL IBC MODEL

In this section, we describe the proposed methodology for determining the equivalent IBC of a corrugated coating using the GA. In the first step, the reflection coefficients from the coating are computed using the MoM at multiple incident angles to serve as the reference data of the model. The MoM solution for the corrugated coating structure in Fig. 1 has been formulated earlier in [6]. The formulation entails dividing one cell of the grating into different homogeneous regions according to the material layers as shown in Fig. 2(a). Boundary integral equations are first obtained for each region. Field continuity at region interfaces and periodic boundary conditions at cell boundaries are then enforced. The fields in the top half-space are expanded into a sum of Floquet harmonics and are matched to the fields in the lower region so that the reflection coefficients can be found.

In the next step, a periodic IBC model is proposed, from which we can derive an expression for the reflection coefficients. In the final step, the optimal parameters for the IBC model are obtained by minimizing the mean squared error between the two sets of reflection coefficients based on the GA. These steps are described in detail below.

A. Periodic IBC Model

The equivalent IBC relating the tangential electric and magnetic fields for a planar coated surface can be written as [1]:

$$\begin{bmatrix} E_z \\ E_x \end{bmatrix} = \begin{bmatrix} Z_{zz} & Z_{zx} \\ Z_{zx} & Z_{xx} \end{bmatrix} \begin{bmatrix} H_z \\ H_x \end{bmatrix} \quad (1)$$

We shall adopt this model for the corrugated problem due to its simplicity and usefulness for our applications. The model parameters will then be optimized to emulate the properties of the exact structure. Note that since the corrugated surface exhibits anisotropic scattering characteristics, the equivalent IBC must also in general be anisotropic. Therefore, the cross impedance terms Z_{zx} and Z_{xz} are kept in our formulation to assess their importance. The boundary impedance Z_{zz} , Z_{zx} , Z_{xz} , and Z_{xx} are

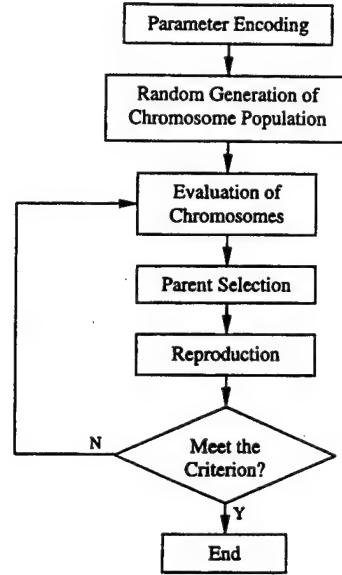


Fig. 3. Flow chart of the GA.

in general functions of incident angle and spatial position. For the IBC model to be useful for subsequent electromagnetic analysis, however, it is much preferable to model the boundary impedances as functions of spatial position only. We cannot prove theoretically the existence of such a model for an arbitrary corrugated structure. Instead, the applicability and limitation of this approach will be explored numerically in Section III.

In our IBC model, the periodic grating structure with period p , as shown in Fig. 2(a), is replaced by an equivalent impedance boundary condition, which also has a period p , as illustrated in Fig. 2(b). Each surface impedance term can be expanded into a Fourier series. Since the cross impedance terms Z_{zx} and Z_{xz} are usually very small, we shall treat them as constants and only expand the impedances Z_{xx} and Z_{zz} as

$$Z_{xx} = \sum_{n=-\infty}^{\infty} a_n e^{-j\frac{2\pi}{p}nx}, \quad Z_{zz} = \sum_{n=-\infty}^{\infty} b_n e^{-j\frac{2\pi}{p}nx}. \quad (2)$$

Therefore, to fully describe the IBC model, we must determine the Fourier series coefficients $\{a_n\}$ and $\{b_n\}$.

B. Solution to the Forward Problem of Scattering by the IBC Model

Next, we derive the reflection coefficients resulting from the plane wave scattering from the IBC model given above. Under plane wave incidence where

$$\begin{aligned} k_{x0}^i &= k_0 \sin \theta \sin \phi, & k_{y0}^i &= -k_0 \cos \theta & \text{and} \\ k_{z0}^i &= k_0 \sin \theta \cos \phi \end{aligned}$$

each component of the tangential electric and magnetic fields at the impedance surface can be expanded into a sum of Floquet harmonics [7]. For example, the tangential electric field in the z direction is expanded as

$$E_z = E_z^i e^{-jk_{z0}x} + \sum_{n=-\infty}^{\infty} E_{zn}^r e^{-jk_{zn}x} \quad (3)$$

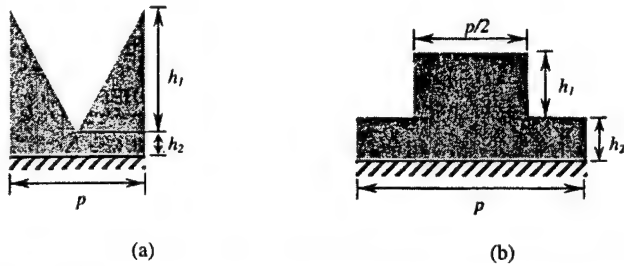


Fig. 4. Grating geometry for (a) triangular groove and (b) rectangular groove.

where

$$k_{xn} = k_{x0} + n \frac{2\pi}{p}$$

is the propagation constant of the n th order harmonic along the x -direction. This Floquet harmonic is a reflected wave with propagation constants (k_{xn}, k_{yn}^r, k_z) , where $k_{yn}^r = \sqrt{k_0^2 - k_z^2 - k_{xn}^2}$ with the square root taken as positive real or negative imaginary. The superscripts i and r denote respectively the incident and reflected field throughout this paper. The harmonic term $e^{j\omega t} e^{-jk_z z}$ is suppressed in (3) and y is set to zero at the impedance surface for convenience. Assuming that the coefficients of the higher order Floquet harmonics are negligible and applying this to other tangential field components we get

$$F = F^i e^{-jk_{z0}x} + \sum_{n=-N}^N F_n^r e^{-jk_{zn}x} \quad (4)$$

where F can be E_z , H_z , E_x or H_x , and N is a positive integer. Substituting (2) and (4) into (1) and matching the coefficients of the exponential terms, we obtain a set of equations relating E_{zn} , H_{zn} and H_{zn}

$$\begin{aligned} E_z^i \delta_{n0} + E_{zn}^r \\ = Z_{zz} H_{zn}^r + \sum_{m=-N}^N a_{n-m} H_{xm}^r + a_n H_x^i + Z_{zz} H_z^i \delta_{n0} \end{aligned} \quad (5)$$

for $n = -N$ to N . δ_{n0} is the Kronecker delta. This set of equations can be written in matrix form as

$$E_z^i \mathbf{u}_N + \mathbf{E}_z^r = Z_{zz} \mathbf{H}_z^r + \mathbf{A} \mathbf{H}_x^r + H_x^i \mathbf{a} + Z_{zz} H_z^i \mathbf{u}_N \quad (6)$$

where

$$\begin{aligned} \mathbf{E}_z^r &= [E_{z,-N}^r \cdots E_{z0}^r \cdots E_{z,N}^r]^T \\ \mathbf{H}_z^r &= [H_{z,-N}^r \cdots H_{z0}^r \cdots H_{z,N}^r]^T \\ \mathbf{H}_x^r &= [H_{x,-N}^r \cdots H_{x0}^r \cdots H_{x,N}^r]^T \\ \mathbf{A} &= \begin{bmatrix} a_0 & \cdots & a_{-N} & \cdots & a_{-2N} \\ \vdots & \ddots & \vdots & \ddots & \vdots \\ a_N & \cdots & a_0 & \cdots & a_{-N} \\ \vdots & \ddots & \vdots & \ddots & \vdots \\ a_{2N} & \cdots & a_N & \cdots & a_0 \end{bmatrix}, \quad \mathbf{a} = \begin{bmatrix} a_{-N} \\ \vdots \\ a_0 \\ \vdots \\ a_N \end{bmatrix} \end{aligned}$$

and

$$\mathbf{u}_N = [u_{-N} \cdots u_0 \cdots u_N]^T, \quad u_n = \delta_{n0}.$$

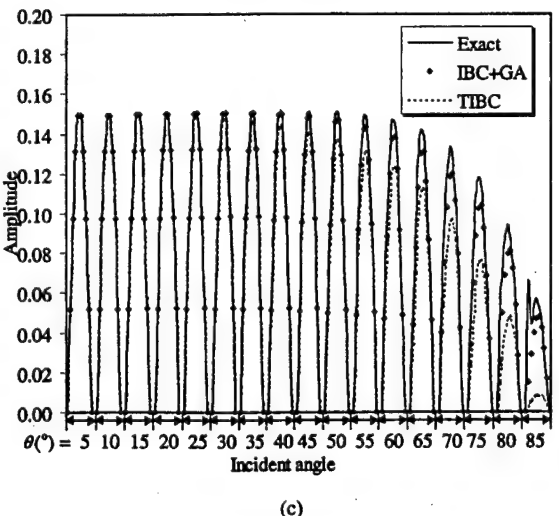
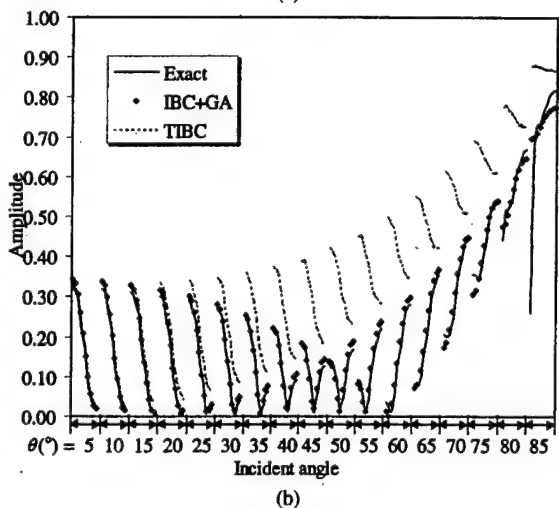
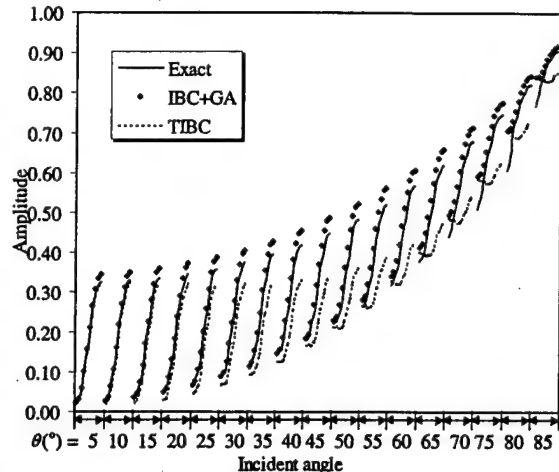


Fig. 5. Comparison of reflection coefficients versus angle among: 1) the exact MOM result; 2) the IBC derived from GA; and 3) the TIBC result. (a) H-polarization. (b) V-polarization. (c) H-V cross polarization.

Following the same steps, we also arrive at the relationship for E_{zn} , H_{zn} , and H_{zn}

$$\mathbf{B} \mathbf{H}_z^r = \mathbf{E}_x^r - Z_{xx} \mathbf{H}_x^r + E_x^i \mathbf{u}_N - Z_{xx} H_x^i \mathbf{u}_N - H_z^i \mathbf{b} \quad (7)$$

where

$$\mathbf{B} = \begin{bmatrix} b_0 & \cdots & b_{-N} & \cdots & b_{-2N} \\ \vdots & \ddots & \vdots & \ddots & \vdots \\ b_N & \cdots & b_0 & \cdots & b_{-N} \\ \vdots & \ddots & \vdots & \ddots & \vdots \\ b_{2N} & \cdots & b_N & \cdots & b_0 \end{bmatrix}, \quad \mathbf{b} = \begin{bmatrix} b_{-N} \\ \vdots \\ b_0 \\ \vdots \\ b_N \end{bmatrix}.$$

For a plane wave, the tangential components of the fields in the x -direction E_x , H_x can be expressed in terms of E_z and H_z as

$$\begin{bmatrix} E_x^r \\ H_x^r \end{bmatrix} = [\mathbf{T}] \begin{bmatrix} E_z^r \\ H_z^r \end{bmatrix}, \quad \text{and} \quad \begin{bmatrix} E_x^i \\ H_x^i \end{bmatrix} = [\mathbf{T}^i] \begin{bmatrix} E_z^i \\ H_z^i \end{bmatrix} \quad (8)$$

where

$$\mathbf{T} = \begin{bmatrix} -\frac{k_{x,-N}k_z}{k_t^2} & 0 & -\frac{k_{y,-N}k_0}{k_t^2}\eta_0 & 0 \\ \vdots & \ddots & \vdots & \vdots \\ 0 & -\frac{k_{x,N}k_z}{k_t^2} & 0 & -\frac{k_{y,N}k_0}{k_t^2}\eta_0 \\ \frac{k_{y,-N}k_0}{k_t^2\eta_0} & 0 & -\frac{k_{x,-N}k_z}{k_t^2} & 0 \\ \vdots & \ddots & \vdots & \vdots \\ 0 & \frac{k_{y,N}k_0}{k_t^2\eta_0} & 0 & -\frac{k_{x,N}k_z}{k_t^2} \end{bmatrix}$$

and

$$\mathbf{T}^i = \begin{bmatrix} -\frac{k_{x,0}k_z}{k_t^2} & -\frac{k_{y,0}k_0}{k_t^2}\eta_0 \\ \frac{k_{y,0}k_0}{\eta_0 k_t^2} & -\frac{k_{x,0}k_z}{k_t^2} \end{bmatrix}, \quad \left(k_t = \sqrt{k_0^2 - k_z^2} \right).$$

Combine (6)–(8), the matrix relationship between the incident and reflected fields is written as

$$\begin{bmatrix} E_z^r \\ H_z^r \end{bmatrix} = \left(\begin{bmatrix} \mathbf{I} & -Z_{zz}\mathbf{I} \\ 0 & \mathbf{B} \end{bmatrix} - \begin{bmatrix} 0 & \mathbf{A} \\ \mathbf{I} & -Z_{xx}\mathbf{I} \end{bmatrix} [\mathbf{T}] \right)^{-1} \\ \times \left(\begin{bmatrix} 0 & \mathbf{a} \\ \mathbf{u}_N & -Z_{zz}\mathbf{u}_N \end{bmatrix} [\mathbf{T}^i] + \begin{bmatrix} -\mathbf{u}_N & -Z_{xx}\mathbf{u}_N \\ 0 & \mathbf{b} \end{bmatrix} \right) \\ \times \begin{bmatrix} E_z^i \\ H_z^i \end{bmatrix}. \quad (9)$$

In (9), the z components of the scattered field can be directly related to those of the incident field. We can therefore define the reflection coefficients for the different polarizations as

$$R_n^{\text{TM-TM}} = \frac{E_{zn}^r}{E_{zn}^i} \Big|_{H_z^i=0}, \quad R_n^{\text{TM-TE}} = -\frac{\eta_0 H_{zn}^r}{E_{zn}^i} \Big|_{H_z^i=0} \\ R_n^{\text{TE-TE}} = -\frac{H_{zn}^r}{H_z^i} \Big|_{E_z^i=0}, \quad R_n^{\text{TE-TM}} = \frac{E_{zn}^r}{\eta_0 H_z^i} \Big|_{E_z^i=0}. \quad (10)$$

To summarize, the reflection coefficients from the IBC model can be calculated by using (9) and (10) if a_n and b_n are given. This relationship is utilized by the GA to calculate the reflection coefficients for a given sample of $\{a_n\}$ and $\{b_n\}$ and compare them with the reference data obtained from the MoM solution to optimize the model parameters.

Two comments are in order. First, although the reflection coefficients are derived for the TE_z/TM_z polarizations, they can be easily transformed to the more conventional vertical (V)/horizontal (H) polarizations with respect to the surface. Second, we have assumed the position of the IBC surface is at $y = 0$ in the above formulation. However, if the IBC surface is at the position $y = -d$ [as shown in Fig. 2(b)], a factor of $e^{-j2k_y d}$ should be

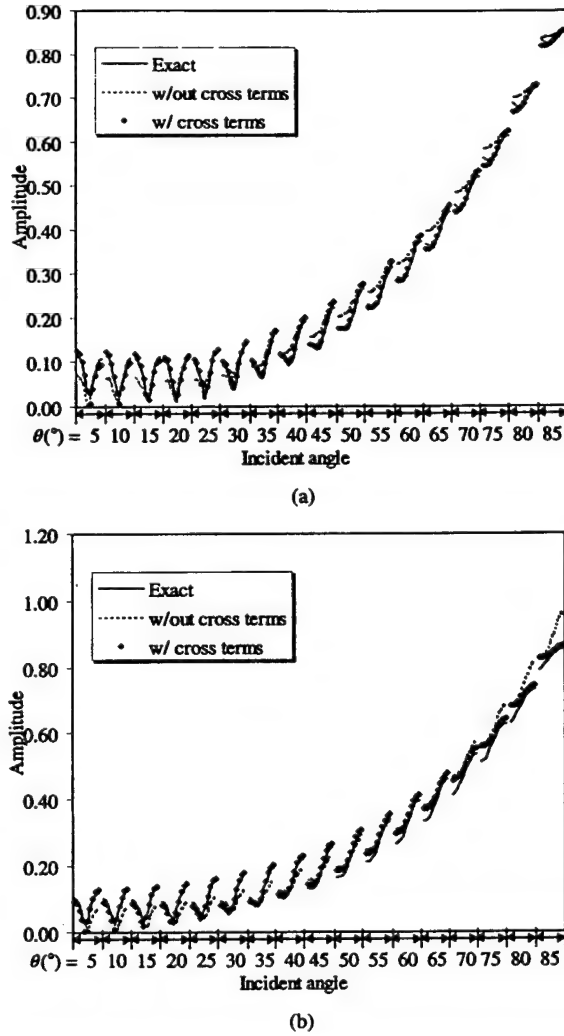


Fig. 6. Effect of incorporating the cross impedance terms in the IBC model generated from GA, (a) H-polarization, (b) V-polarization.

multiplied to each of the reflection coefficients to arrive at the correct answer. It is well known that in general layered coating problems, there is not a preferred position for the impedance surface. The solution can sometimes be improved by applying the IBC at a position other than a natural interface in the structure [4]. Therefore, by including the position of the IBC surface as an additional tuning parameter in our IBC model, we can further improve the accuracy of the model.

C. Genetic Algorithm to Determine the Optimal IBC Parameters

In the GA, the parameters to be optimized are first encoded into binary form. A set of the encoded parameters is known as a chromosome. The basic idea of GA is to generate a pool of chromosomes, discard the bad ones, keep the best ones and let them evolve to produce better chromosomes. The evaluation of each chromosome is performed by a cost function which, in this case, is chosen to be the mean-squared error between the MoM computed reflection coefficients and those solved using (9) and (10) with the $(Z_{zz}, a_n, b_n, Z_{xx}, d)$ parameters decoded from the corresponding chromosome. Chromosomes in the pool are ranked according to the cost function. The best ones are selected in pairs

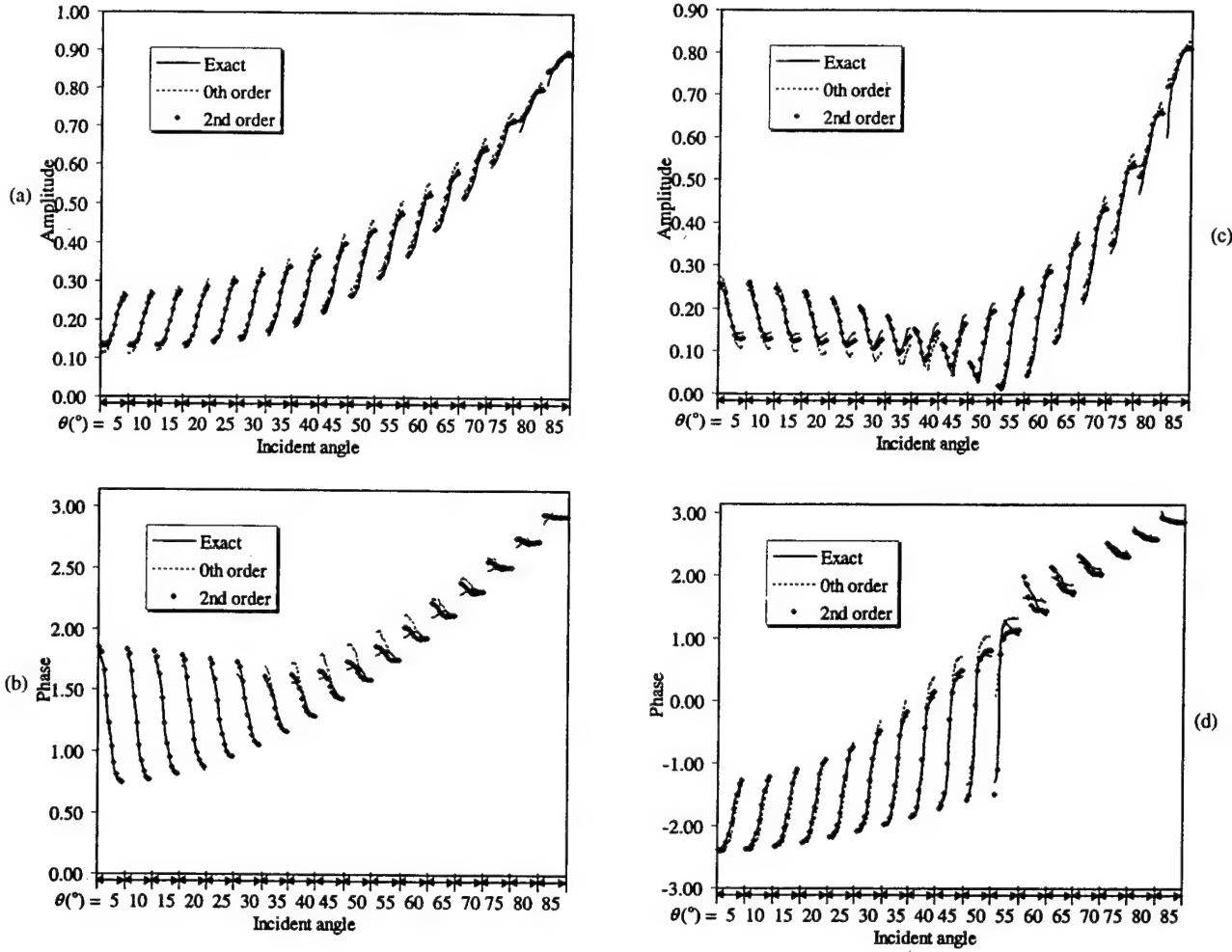


Fig. 7. Effect of increasing the model order in the IBC model generated from GA. (a) Amplitude, H-polarization. (b) Phase, H-polarization. (c) Amplitude, V-polarization. (d) Phase, V-polarization.

to act as parents of the next generation. Reproduction of children chromosomes is based on specific rules of heredity and mutation. The process of selection and reproduction is repeated until a set of satisfactory parameters is found or the generation limit is reached. The flow chart of the GA is shown in Fig. 3. Detailed discussion of the GAs can be found in [8].

In the IBC model for the corrugated coating, the parameters to be optimized are the coefficients of the Fourier expansion a_n and b_n , the cross impedances Z_{zz} , Z_{xx} and the position of the impedance surface d . Each of the parameters a_n , b_n , Z_{zz} and Z_{xx} consists of a real part and an imaginary part. We assume a symmetric structure so that $a_n = a_{-n}$, $b_n = b_{-n}$. For an approximation truncated to the N th order, the total number of real numbers is $4N + 9$. The number of bits contained in each parameter B is adjustable. If B is too large, the convergence of GA will be slow. If B is too small, the accuracy of the calculation will suffer. In the examples given in this paper, we choose $B = 8$ to be efficient in both speed and accuracy. In order to encode the unknown parameters into binary form, the minimum and maximum possible values of each parameter are required. For example, the values for the real and imaginary parts of the Fourier series a_n and b_n are estimated to be in the range from $-3\eta_0$ to $3\eta_0$, which is found to be reasonable in the numerical ex-

amples. Thus, the eight-bit binary 00000000 denotes $-3\eta_0$ and 11111111 represents $3\eta_0$. Z_{zz} and Z_{xx} are relatively small and their real and imaginary parts vary from $-0.1\eta_0$ to $0.1\eta_0$. The distance d is limited between the upper and lower boundaries of the coating so that the resulting IBC model will not cause any ambiguity in its applications.

In the beginning of the GA, a number of chromosomes are randomly generated. Each chromosome is decoded into parameters Z_{zz} , a_n , b_n , Z_{xx} and d . The reflection coefficients are then computed using (9) and (10). The cost function gives the mean-squared error between these reflection coefficients and their corresponding MoM solution

$$\text{Cost} = \sum_{\theta, \phi} \sum_{P_1, P_2} \left| R^{P_1-P_2} - R_0^{P_1-P_2} \right|^2$$

where R_0 denotes the MoM solution of the reflection coefficients at a specific observation angle (θ, ϕ) and P_1, P_2 is the polarization TE_z/TM_z (or V/H). The fitness value of each chromosome is given by

$$f(C_i) = c_1 - c_2 \text{Cost}(C_i)$$

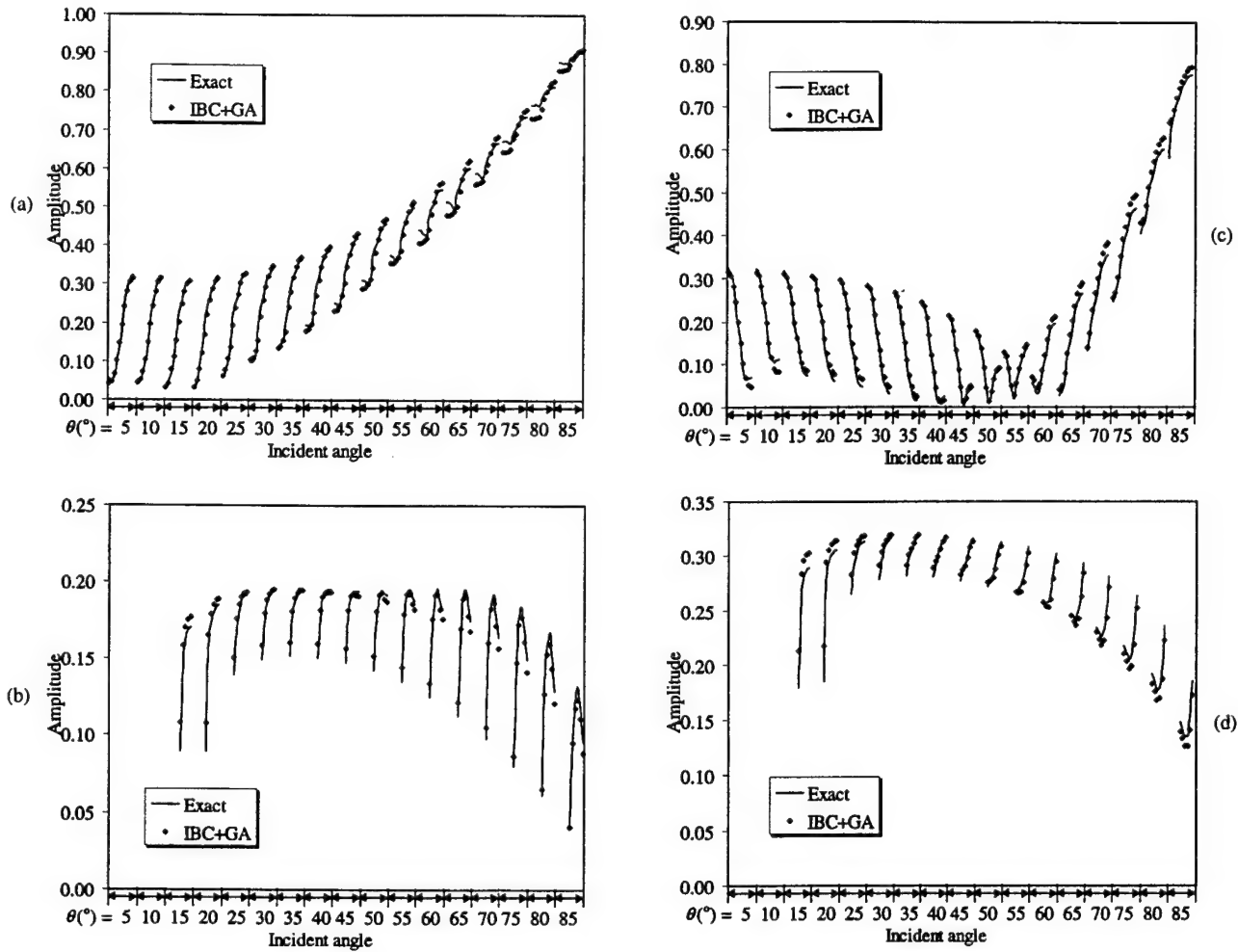


Fig. 8. Higher order reflection coefficients simulated by the IBC model. (a) 0th order, H-pol. (b) First order, H-pol. (c) 0th order, V-pol. (d) 1st order, V-pol.

where c_1 and c_2 are constants and C_i is the i th chromosome in the population. This fitness value is used in ranking the chromosomes and selecting of parents for the next generation [8]–[11]. There are several standard ways of selection. In this paper, the roulette wheel selection is used in which the probability of each chromosome to be selected is proportional to its fitness value.

After two chromosomes are selected, they mate to generate children. This is realized by the process of crossover in which a break point is randomly chosen in the chromosomes and the two chromosomes are switched at that point. Mutation is imposed at this point so that new genes appear in the next generation. The mutation rate, which is the portion of bits to be randomly changed, is also an important parameter in GA. Experiments show that a mutation rate of 5–8% is often efficient in the calculation.

The process of evaluation, selection, and reproduction is repeated until a desired mean-squared error is achieved or a maximum generation is reached. For a population of 400 chromosomes, the 0th order IBC (i.e., $N = 0$) takes 10–20 generations to converge to the optimum while the second-order IBC takes 200–400 generations.

III. NUMERICAL EXAMPLES

In this section, some examples are presented to demonstrate the effectiveness of the method. The first example is a deep triangular grooved grating with relatively small period. The geometry of one cell of the grating is shown in Fig. 4(a) where the period $p = 0.067\lambda_0$ and $h_1 = 0.22\lambda_0$, $h_2 = 0.017\lambda_0$. The coating material is MagRAM with material constants $\epsilon_r = 14.35 - j0.28$ and $\mu_r = 1.525 - j1.347$ at the frequency of 10 GHz. Seventeen observation angles are selected which include normal incidence and the combination of $\theta = 20^\circ, 40^\circ, 60^\circ, 80^\circ$ and $\phi = 0^\circ, 30^\circ, 60^\circ, 90^\circ$. In this example, we set Z_{xx} and Z_{zz} in (1) to zero and $N = 0$ in (4) to make the model comparable with TIBC. The co-polarization reflection coefficients for the H-pol and V-pol incidence are plotted in Fig. 5(a) and (b), respectively, and the H–V cross-polarization reflection coefficients are plotted in Fig. 5(c). In the figures, the x -axis is divided into sections of different incident angle θ , which varies from 5° to 85° in steps of 10° . In each of the θ section, the grating angle ϕ varies from 0° to 90° . The matching of the reflection coefficients between the GA approach and MoM solution is good at most incident angles, even near grazing incidence. The value of

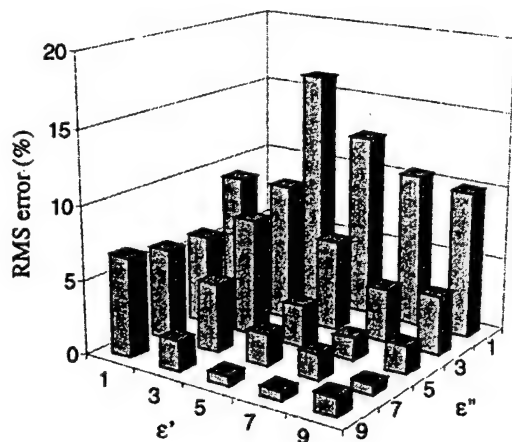


Fig. 9. Error of the IBC model as a function of material constant $\epsilon = \epsilon' - j\epsilon''$.

d is found to be $0.027\lambda_0$ from the tip of the groove or $0.21\lambda_0$ above the ground plane. The TIBC result is also generated by using the reflection coefficient at normal incidence to derive the equivalent boundary condition. The impedance surface is placed at the plane of the conductor backing. It can be seen that the TIBC results deviate significantly from the reference solution away from normal incidence. With the same complexity of the boundary condition, GA achieves a much better matching because more observation points are used in the modeling and because of the additional degree of freedom in the position of the IBC surface.

Next, we compare the IBC approximations with and without the cross impedance terms Z_{xx} and Z_{zz} . The structure is a rectangular groove as shown in Fig. 4(b) with a period $p = 0.17\lambda_0$ and a groove depth of $h_1 = h_2 = 0.042\lambda_0$. The material constants are $\epsilon_r = 8.3 - j2.4$ and $\mu_r = 2 - j0.9$ at 10 GHz. The same observation points are used as in the previous example. The 0th order ($N = 0$) IBC is determined and the comparison between the reflection coefficients is illustrated in Fig. 6. With the cross impedance included, the accuracy of the approximation is improved.

In the third example, the IBC of different orders are obtained for the structure shown in Fig. 4(b) where $p = 0.42\lambda_0$, $h_1 = 0.25\lambda_0$ and $h_2 = 0.17\lambda_0$. The coating material is the same as that in example 2 but the period is much larger and the groove is deeper. The reflection coefficients predicted by the 0th-order and second-order model are plotted in Fig. 7. While the approximation by the 0th-order model is fairly satisfactory, the second-order model further improves the result and the matching is better at most incident angles. The price of the improvement is the computation time. For the 0th-order modeling, it takes only a few minutes for the GA to converge while the second-order IBC takes more than 1 h on an SGI O2 workstation (R10000/155 MHz). Another consequence as the order of the model is increased is that the resulting IBC will show more spatial variation. This implies that when the IBC model is utilized in subsequent analysis using numerical electromagnetics solvers, the impedance surface must be divided more finely to faithfully

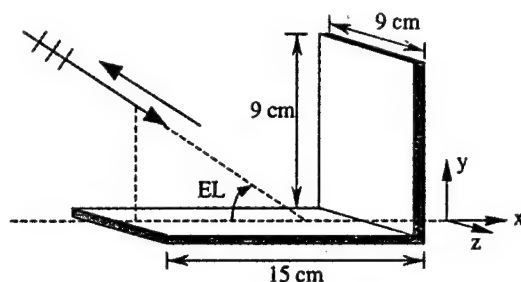


Fig. 10. Geometry of the corner reflector.

describe the IBC. This will lead to a higher computation cost. Thus, the higher order model is not recommended unless the 0th-order one is intolerable or the period is large compared to the wavelength. Generally speaking, the IBC model can be improved by increasing the model order whether or not the cross-impedance terms exist. But with the cross-impedance terms, the required model order is usually smaller than that without them.

We further investigate a structure with a period larger than half a wavelength, which results in higher order Floquet-mode reflection at some incident angles. The rectangular groove shown in Fig. 4(b) has a period $p = 0.85\lambda_0$ and $h_1 = h_2 = 0.42\lambda_0$. The material constant are $\epsilon_r = 10.5 - j2.2$ and $\mu_r = 2 - j0.3$. The 0th and 1st order reflection coefficients are plotted in Fig. 8(a) and (b), respectively. It is shown that the Floquet modes are also well characterized.

In the final example, we investigate the limitation of the IBC model. We consider a triangular groove shown in Fig. 4(a) with $p = 0.33\lambda_0$ and $h_1 = h_2 = 0.08\lambda_0$. The optimal IBC model is found using the GA for different coating materials. A second-order IBC model with cross impedance terms is used and the optimal model parameters are determined by running GA to convergence. After the model is found, the root mean squared (RMS) error of the IBC-predicted reflection coefficients over the selected angles are computed. Fig. 9 shows the RMS error of the optimal IBC model as a function of ϵ'_r and ϵ''_r , which are the real and imaginary parts of the coating relative permittivity ϵ_r . μ_r is set to one for all the coatings. We observe that the IBC model works best for high-contrast high-loss materials. For low-contrast or low-loss materials, the model error can be large. This behavior is very similar to conventional IBC models for planar coatings.

We now apply our derived IBC model to a three-dimensional (3-D) scattering problem. Consider the corner reflector as shown in Fig. 10. The monostatic radar cross section (RCS) is calculated for both the uncoated reflector and that coated with the MagRAM structure described in example 1. The groove of the coating is either parallel or perpendicular to the incident direction. Both cases are computed for comparison. Note that the solution for such a structure is very complicated if we try to use the exact MoM formulation. Instead, we use the 0th-order impedance boundary condition obtained from example 1 to replace the corrugated

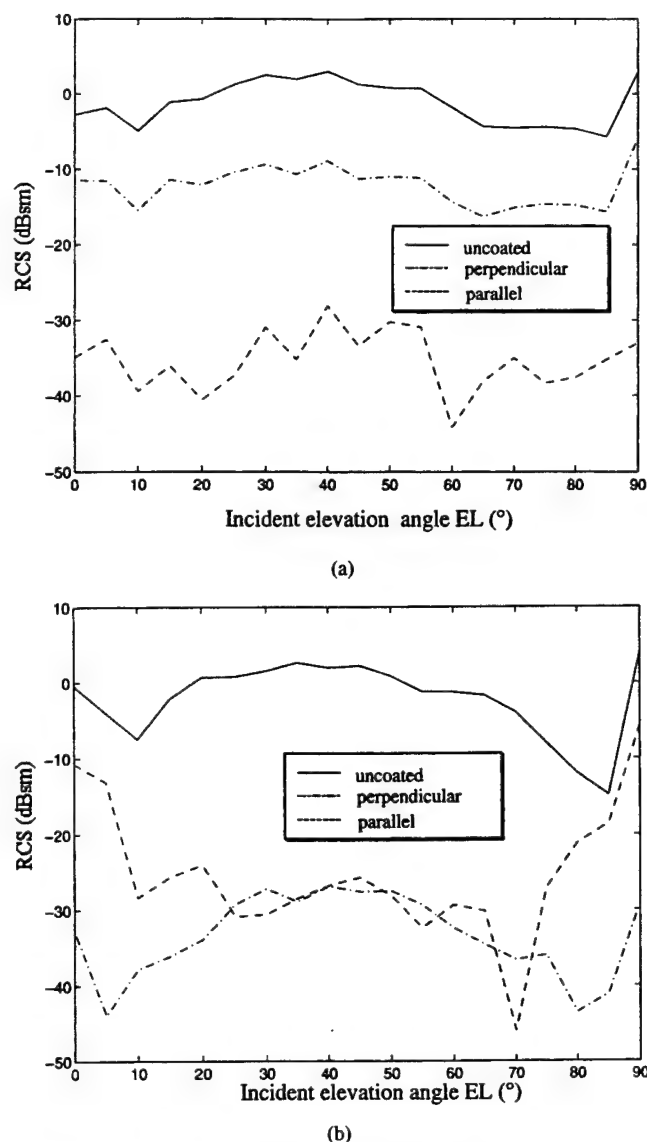


Fig. 11. RCS of the corner reflector ($f = 10$ GHz). (a) H-polarization. (b) V-polarization.

absorber. We assume that the size of the plate remain the same after the IBC replacement. The RCS is computed using FISC [12], which is a 3-D MoM code based on the fast multipole method [13]. Comparisons of the RCS at several elevation angles are shown in Fig. 11 for both the H- and V-polarizations. The result shows the effect of coating, which lowers the overall RCS level for both polarizations. We further observe that a 30-dB RCS reduction can be achieved for both polarizations over the range of elevation angles from 20° to 75° if the grating is oriented parallel to the incident wave.

IV. CONCLUSION

In this paper, an impedance boundary condition model is derived based on the GA to approximate arbitrary corrugated

coating structures in scattering problems. The periodic structure is replaced by a periodic IBC on a virtual surface. The boundary impedance and the position of the surface are optimized by matching the reflection coefficients to the rigorous numerical solution at a number of incident angles. Similar to traditional IBC models, this approach is most effective when the coating material is high loss and of high contrast. The resulting IBC model generated by this algorithm can be incorporated into an existing computational electromagnetics code to assess the performance of the corrugated coating when mounted on complex platforms.

Compared with other IBC approaches, the method described above has several advantages. First, the boundary impedance is assumed to be anisotropic so that the same model can be applied to oblique incidence from any arbitrary angles. Second, it is possible to build in spatial variation of the boundary impedance by adjusting the number of terms used in the Fourier series expansion. By using more terms, the IBC model can be made more accurate. In addition, the position of the impedance surface can also be optimized. By solving for the best position of the impedance surface as one of the model parameters, the accuracy of the model can be improved.

Numerical experiments show that the IBC approximation can be improved if some of the parameters of the GA are carefully chosen. These parameters include the incident angles at which the rigorous solution is obtained, the range of each model parameter, and the mutation rate, etc. The GA can also be accelerated with carefully chosen parameters and a well-designed cost function.

REFERENCES

- [1] D. J. Hoppe and Y. Rahmat-Samii, *Impedance Boundary Conditions in Electromagnetics*. Bristol, PA: Taylor Francis, 1995.
- [2] T. B. A. Senior and J. L. Volakis, *Approximate Boundary Conditions in Electromagnetics*. London, U.K.: Inst. Elect. Eng., 1995.
- [3] G. Pelosi and P. Y. Ufimtsev, "The impedance-boundary condition," *IEEE Antennas Propagat. Mag.*, vol. 38, pp. 31–34, Feb. 1996.
- [4] T. B. A. Senior and J. L. Volakis, "Derivation and application of a class of generalized boundary conditions," *IEEE Trans. Antennas Propagat.*, vol. 37, pp. 1566–1572, Dec. 1989.
- [5] K. W. Whites and R. Mittra, "Equivalent boundary-condition model for lossy planar periodic structures at low frequencies," *IEEE Trans. Antennas Propagat.*, vol. 44, pp. 1617–1629, Dec. 1996.
- [6] J. Moore, H. Ling, and C. S. Liang, "The scattering and absorption characteristics of material-coated periodic grating under oblique incidence," *IEEE Trans. Antennas Propagat.*, vol. 41, pp. 1281–1288, Sept. 1993.
- [7] R. Petit, Ed., *Electromagnetic Theory of Gratings*. New York: Springer-Verlag, 1980.
- [8] *Handbook of Genetic Algorithms*, L. Davis, Ed., Van Nostrand Reinhold, New York, 1991.
- [9] R. L. Haupt, "An introduction to genetic algorithms for electromagnetics," *IEEE Antennas Propagat. Mag.*, vol. 37, pp. 7–15, Apr. 1995.
- [10] D. S. Weile and E. Michielssen, "Genetic algorithm optimization applied to electromagnetics: A review," *IEEE Trans. Antennas Propagat.*, vol. 45, pp. 343–353, Mar. 1997.
- [11] G. Winter, J. Periaux, M. Galan, and P. Cuesta, *Genetic Algorithms in Engineering and Computer Science*. New York: Wiley, 1995.
- [12] User's Manual for FISC (Fast Illinois Solver Code), Ctr. Computat. Electromagn., Univ. Illinois and DEMACO, Champaign, IL, Jan. 1997.
- [13] J. M. Song and W. C. Chew, "Fast multipole method solution using parametric geometry," *Microwave Opt. Tech. Lett.*, vol. 7, pp. 760–765, Nov. 1994.



Tao Su (S'97) was born in Beijing, China, in 1973. He received the B.S. degree in electronics engineering from Tsinghua University, Beijing, in 1996, and the M.S. degree in electrical engineering from the University of Texas at Austin in 1997. He is currently working toward the Ph.D. degree at the University of Texas at Austin.

Since 1996, he has been working as a Graduate Research Assistant in the Department of Electrical and Computer Engineering, University of Texas at Austin. His research interests include simulation and

modeling of antenna-platform radiation, model based parameter estimation in scattering and radiation problems, optimization methods in computational electromagnetics, and the coupling effect in array signal processing.



Hao Ling (S'83-M'86-SM'92-F'99) was born in Taichung, Taiwan, on September 26, 1959. He received the B.S. degrees in electrical engineering and physics from the Massachusetts Institute of Technology, Cambridge, in 1982, and the M.S. and Ph.D. degrees in electrical engineering from the University of Illinois at Urbana-Champaign, in 1983 and 1986, respectively.

In September 1986, he joined the faculty of the University of Texas at Austin and is currently a Professor of electrical and computer engineering.

In 1982 he was associated with the IBM Thomas J. Watson Research Center, Yorktown Heights, NY, where he conducted low-temperature experiments in the Josephson Program. He participated in the Summer Visiting Faculty Program in 1987 at the Lawrence Livermore National Laboratory, CA. In 1990 he was an Air Force Summer Fellow at the Rome Air Development Center, Hanscom Air Force Base, MA. His research interests are in radar signature prediction, computational techniques, and radar signal analysis for scattering mechanism interpretation and target identification.

Dr. Ling was a recipient of the National Science Foundation Presidential Young Investigator Award in 19987, the NASA Certificate of Appreciation in 1991, and the Archie Straiton Junior Faculty Teaching Excellence Award in 1993 and holder of the Chevron Centennial Fellowship in Engineering.

A Radiation Center Representation of Antenna Radiation Patterns on a Complex Platform

Caner Ozdemir, *Member, IEEE*, Rajan Bhalla, and Hao Ling, *Fellow, IEEE*

Abstract—A sparse model of the antenna radiation pattern on a complex platform is presented. This representation is based on a point radiator model that describes the radiation pattern by a collection of radiation centers on the platform. The methodology for obtaining the radiation center model is presented. It entails first generating the three-dimensional (3-D) antenna synthetic aperture radar (ASAR) imagery of the platform and then parameterizing the resulting image by a collection of point radiators via the CLEAN algorithm. It is shown that once such a representation is obtained, we can reconstruct and extrapolate antenna radiation patterns over frequencies and aspects with good fidelity, thus achieving high data compression ratio. Furthermore, it is shown that the resulting radiation center information can be used to pinpoint cause-and-effect in platform scattering and provide important guidelines for reducing platform effects.

Index Terms—Antenna radiation patterns, scattering centers.

I. INTRODUCTION

IT IS well known that the platform structure that supports an antenna can dramatically alter its radiation characteristics. Recently, we developed an imaging algorithm, termed antenna synthetic aperture radar (ASAR) imaging, to pinpoint the locations of secondary scattering off a mounting platform from the antenna radiation data [1]. Our approach is similar to the inverse synthetic aperture radar (ISAR) concept. Contrary to conventional ISAR imaging, a key complication of the ASAR imaging scenario is that the antenna is located in the near field of the platform. It was shown that under the small-angle approximation and single-bounce assumption, a Fourier transform relationship exists between multifrequency, multi-aspect radiation data and the three-dimensional (3-D) positions and strengths of the secondary scatterers on the platform. Therefore, a 3-D image showing the spatial locations of platform scattering can be constructed via Fourier inversion of the radiation data. This concept was demonstrated using the computed radiation data from the code Apatch [2], which employs the shooting and bouncing ray (SBR) technique [3]–[6]. Fig. 1 shows the CAD model of an airplane with a small vertical dipole antenna placed above the cockpit. The entire airplane is assumed to be perfectly conducting. By collecting the multiple frequency

(10-GHz with 0.56-GHz bandwidth) and multiple aspect (3.33° azimuth window and 1.72° elevation window about the nose) radiation pattern, a 3-D image can be formed from the ASAR algorithm. Shown in Fig. 2(a) is the 3-D ASAR image viewed along various horizontal cuts through the airplane. The key scattering locations near the nose and wings of the airplane can be clearly identified. This is very similar to an ISAR image in which the strong scattering locations on the target are displayed to facilitate signature reduction and target identification applications.

In this paper, we extend the work in [1] by extracting a sparse representation of the ASAR imagery. This is motivated by the observation that similar to an ISAR image, ASAR images exhibit strong point-scatterer like behavior. Since it is well known that the backscattered signature can be modeled by a very sparse set of scattering centers on the target [6]–[9], we believe it is also possible to parameterize the radiation patterns of an antenna mounted on a complex platform via a set of “radiation centers.” Using an approach similar to our recent work on scattering center extraction [6], we utilize the CLEAN algorithm [10], [11] to carry out the radiation center extraction process from an ASAR image. It is shown that once such a representation is obtained, we can reconstruct and extrapolate antenna radiation patterns over frequencies and angles with good fidelity, thus achieving high data compression ratio. Furthermore, it is shown that when coupled with the SBR simulation engine, the resulting radiation center information can be used to pinpoint cause-and-effect in platform scattering and provide important guidelines for reducing platform effects.

This paper is organized as follows. In Section II, we first review the ASAR image formation algorithm and present the radiation center model of the antenna radiation data. Next, we apply the CLEAN algorithm to carry out the extraction process and examine the sparseness of the model and the fidelity of the reconstructed data in frequency and aspect. In Section III, we demonstrate two utilities of the radiation center representation. In the first example, we show that the antenna radiation pattern can be extrapolated over aspect due to the angular stability of the radiation center model. Consequently, it is possible to represent the complex radiation pattern over all observable angles using the radiation centers extracted at only a limited number of angles. In the second example, we carry out a study to reduce platform effects. It is shown that the extracted radiation center information from the SBR simulation engine can be exploited to identify those parts of the target that give rise to significant secondary radiation. Consequently, by placing absorbers over a limited portions of the platform, it is possible to suppress a majority of the platform scattering.

Manuscript received September 30, 1997; March 8, 2000. This work was supported by the Air Force MURI Center for Computational Electromagnetics under Contract AFOSR F49620-96-1-0025 and in part by the Office of Naval Research under Contract N00014-98-1-0178.

C. Ozdemir is with the Department of Electrical and Electronics Engineering, Mersin University, 33342 Mersin, Turkey.

R. Bhalla is with SAIC-DEMCO, Boston, MA 01880 USA.

H. Ling is with the Department of Electrical and Computer Engineering, The University of Texas at Austin, Austin, TX 78712-1084 USA.

Publisher Item Identifier S 0018-926X(00)05785-9.

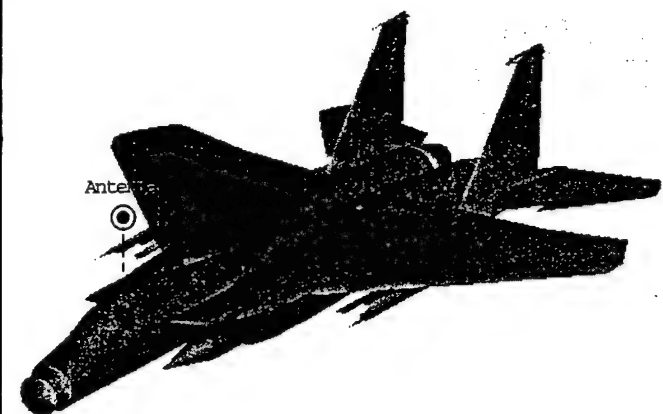


Fig. 1. CAD model of an airplane with a small vertical dipole antenna placed above the cockpit.

It should be noted that the numerical results used throughout this paper will be based on the SBR code Apatch, which does not include higher order scattering phenomena such as higher order diffractions and surface/creeping waves. Furthermore, the example configurations (e.g., dipole above aircraft) considered in this paper may not be construed as practical. However, we believe these limitations do not significantly detract from the main point of this paper, which is the concept of radiation center representation for modeling platform effects.

II. RADIATION CENTER EXTRACTION

A. ASAR Image Formation Algorithm and Radiation Center Model

Before presenting the radiation center model for antenna radiation data, we shall first review the ASAR image formation algorithm presented earlier in [1] and provide some motivations for the radiation center model. To form an ASAR image from antenna radiation data, we first assume the antenna is located at the origin as shown in Fig. 3. The scattered electric field around $-x$ direction from a scattering point $P(x_o, y_o, z_o)$ on the platform can be approximated by

$$E^s(\omega, \phi, \theta) \cong A \cdot e^{-jk(r_o+x_o)} \cdot e^{-jk_o\phi y_o} \cdot e^{-jk_o\theta z_o} \quad (1)$$

where A is the strength of the scattered signal, $r_o = \sqrt{x_o^2 + y_o^2 + z_o^2}$ is the path traveled by the radiated signal from the antenna to point P , k is the free-space wave number, and k_o is the wave number at the center frequency. A small-angle small-bandwidth approximation is used to arrive at the above expression. By setting $u = r + x$ and utilizing the linear dependence of the phase terms in (1) on frequency and angles, we can take the 3-D inverse Fourier transform of the scattered electric field with respect to k , $k_o\phi$, and $k_o\theta$ to generate a 3-D ASAR image as follows:

$$\begin{aligned} \text{ASAR}(u, y, z) &= \text{IFT}_3\{E^s(\omega, \phi, \theta)\} \\ &= \text{IFT}_3\{A \cdot e^{-jk u_o} \cdot e^{-jk_o\phi y_o} \cdot e^{-jk_o\theta z_o}\} \\ &= A \cdot \delta(u - u_o) \cdot \delta(y - y_o) \cdot \delta(z - z_o). \end{aligned} \quad (2)$$

To convert the image into the original xyz -space from the uyz -space, we can use the transformation formula

$$x = \frac{1}{2} \left(u - \frac{(y^2 + z^2)}{u} \right). \quad (3)$$

Therefore, by Fourier processing of the multifrequency multi-aspect radiation data, the point P on the platform can be mapped to a peak in the image at its correct spatial location (x_o, y_o, z_o) . To summarize, the ASAR imaging process consists of 3 steps: 1) collect multifrequency multi-aspect radiation field data $E^s(\omega, \phi, \theta)$; 2) take the 3-D inverse Fourier transform to form the image in the (u, y, z) domain; and 3) use the u -to- x transformation in (3) to generate the final image in the desired (x, y, z) domain.

Although the ASAR formation methodology outlined above can be applied to general radiation data from either measurement or simulation, we have also developed an algorithm especially tailored for the SBR technique called the image-domain formulation. This derivation will serve as the basis of our radiation center model. In applying the SBR technique to the antenna radiation problem, rays are first shot from the phase center of the antenna and traced according to geometrical optics. At the exit point of each ray before they leave the platform altogether, a ray-tube integration is carried out to find the contribution of each ray to the total radiated field at various frequencies and observation angles. Therefore, the radiated field can be expressed as a weighted sum of all the rays that have been shot from the antenna

$$E^s(\omega, \phi, \theta) = \sum_{i \text{ rays}} \alpha_i \cdot e^{-jk u_i} \cdot e^{-jk_o\phi y_i} \cdot e^{-jk_o\theta z_i} \quad (4)$$

where α_i is proportional to the field strength at the exit ray-tube and is only weakly dependent on aspect and frequency. (x_i, y_i, z_i) is the location of the last hit point, and $u_i = d_i + x_i$, where d_i is the total path traveled by i th ray from the antenna to the last hit point. Since the ASAR image is generated from multifrequency multi-aspect data via Fourier inversion, we can interchange the order of the inverse Fourier transform and the ray summation and carry out the inverse Fourier transform for each ray in closed form. The resulting ASAR image is given by

$$\text{ASAR}(x, y, z) = \sum_{i \text{ rays}} \beta_i \cdot h(x - x_i, y - y_i, z - z_i) \quad (5)$$

where

$$\begin{aligned} h(x, y, z) &= e^{-jk_o(r+x)} \text{sinc}(\Delta k x) \\ &\quad \cdot \text{sinc}(k_o\Delta\phi y) \cdot \text{sinc}(k_o\Delta\theta z). \end{aligned} \quad (6)$$

The detailed derivation of this image-domain formula can be found in [1] and will not be repeated here. In the expression, (x_i, y_i, z_i) is the location of the hit point on the target for the i th ray. (For a multiple-bounce ray, it can be shown that its down range x_i is delayed by the additional travel distance from the antenna to the last hit point, while its cross range positions y_i and z_i correspond to those of the last time point.) β_i is the ray amplitude Δk , $\Delta\phi$, $\Delta\theta$ are the half-bandwidths in the k -, ϕ - and

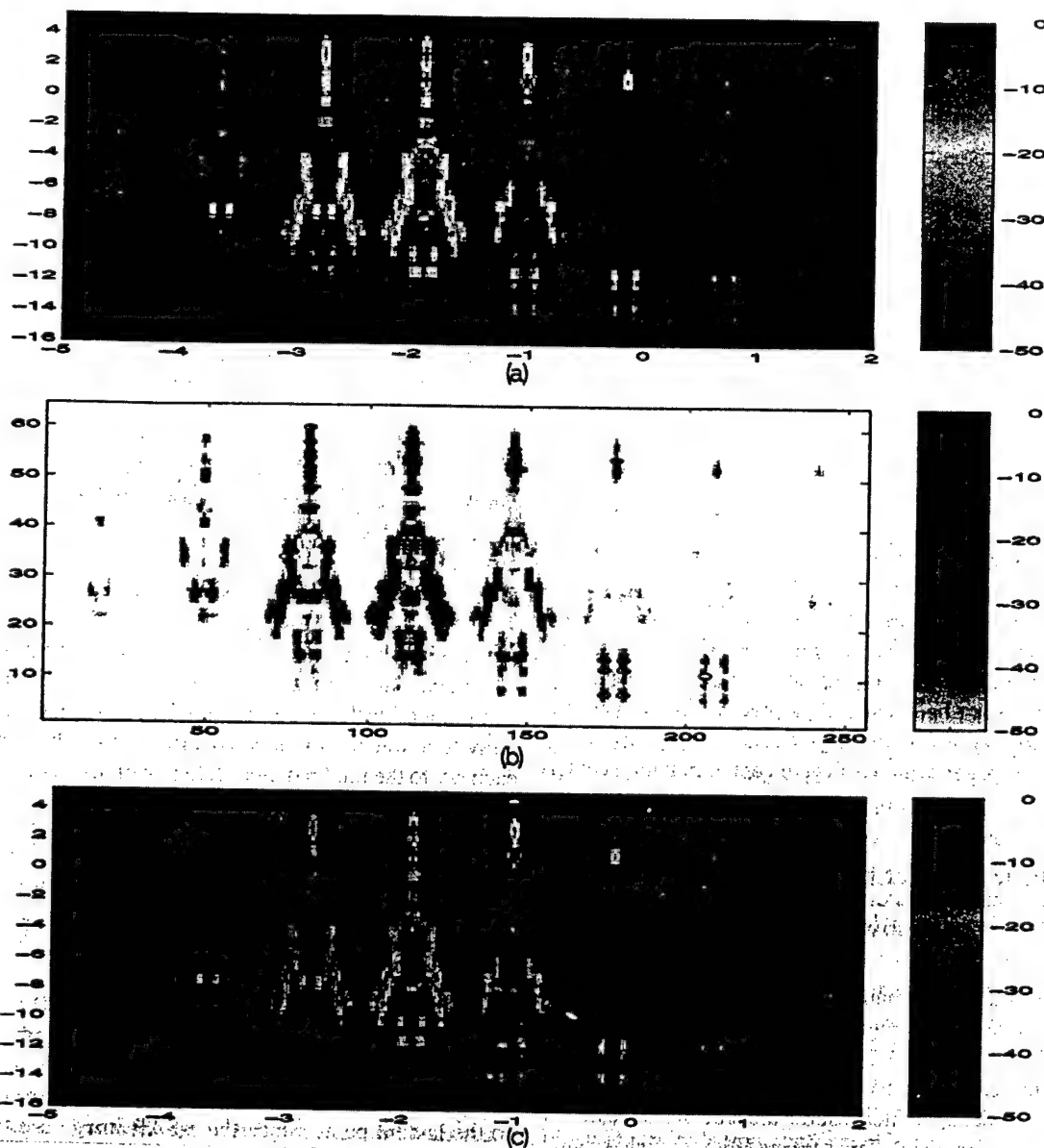


Fig. 2. (a) 3-D ASAR image of the platform generated from the simulated frequency-aspect radiation data about the nose using the code Apatch. (b) The locations of the 150 radiation centers extracted from the 3-D ASAR image using CLEAN. (c) Reconstructed 3-D ASAR image using the extracted radiation centers.

θ -domains, respectively. A key observation from (5) and (6) is that we can form the ASAR image using SBR on a ray-by-ray basis directly in the image domain. Each ray contributes to a spot centered about (x_i, y_i, z_i) in the ASAR image, with the footprint of the spot governed by the 3-D ray spread function h , which plays a role similar to the point-spread function used in the radar community. Therefore, we have shown based on SBR that the ASAR image is composed of a collection of point radiators.

Since tens of thousands of rays are traced in the SBR process, this may imply that tens of thousands of point radiators are needed to adequately represent an ASAR image. However, as we have observed from Fig. 3(a), the ASAR image of a complex platform is actually quite sparse. This is because rays interfere with one another to give rise to strong coherent scattering over only a small localized portion of the target. Therefore, an ASAR image can be accurately represented by only a limited number

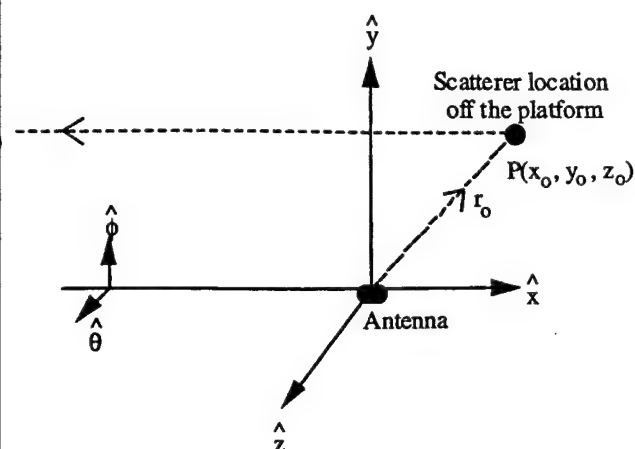
of radiating centers. We adopt a point radiator model which has exactly the same form as (5) to parameterize the ASAR data

$$\text{ASAR}(x, y, z) \approx \sum_{n \text{ radiation centers}} A_n h(x - x_n, y - y_n, z - z_n) \quad (7)$$

where $h(x, y, z)$ is given in (6). The remaining task is to determine (x_n, y_n, z_n) , the locations of the radiation centers, and A_n , their corresponding strengths.

B. Extraction and Reconstruction Algorithms

To carry out the parameterization in (7), we apply the image processing algorithm CLEAN. The CLEAN algorithm is a popular deconvolution technique in radio astronomy [10] and has been successfully utilized for scattering center extraction [6].

Fig. 3. Path of the radiated signal due to a scattering point P on the platform.

It is a robust iterative procedure that successively picks out the highest point in the image, assumes it is a radiating center with the corresponding strength, and removes its point spread response from the image. At the n th iteration, if A_n is the strength of the highest point in the image with locations (x_n, y_n, z_n) , the 3-D residual image is found by

$$\begin{aligned} \text{3-D Residual Image}_{n+1} &= [\text{3-D Residual Image}]_n \\ &\quad - [A_n \cdot h(x - x_n, y - y_n, z - z_n)]. \end{aligned} \quad (8)$$

The extraction process is iterated until the maximum in the residual image reaches a user-defined threshold. Typically, the energy in the residual image decreases quickly during the initial stages of the iteration and tapers off after reaching a noise floor.

As an example, the 3-D ASAR image in Fig. 2(a) is parameterized using the 3-D CLEAN algorithm. The ASAR image is formed using the multifrequency multi-aspect radiation data computed using Apatch for the dipole-airplane configuration shown in Fig. 1. The center frequency is 10 GHz with 0.56 GHz of bandwidth sampled over 64 frequencies. The observation angles are centered about the nose of the airplane and range between -1.67° and 1.67° in azimuth sampled over 32 points and between -0.86° and 0.86° in elevation over eight points. In the ASAR image formation, we use only the scattered field from the airplane and not the direct radiation from the antenna. Therefore, only the platform effect is imaged. Fig. 2(b) shows the locations of the extracted radiation centers from the 3-D ASAR image of Fig. 2(a) using the 3-D CLEAN algorithm. A total of 150 radiation centers are extracted from the image and their locations are plotted in Fig. 2(b) as small circles. We observe that most of them are concentrated around the $z = -2$ m cut which corresponds to the top surface of the airplane. The remainders are located on the two tails. Fig. 2(c) shows the reconstructed ASAR image from the 150 extracted radiating centers. The agreement between the original image and the reconstructed one is quite good over a dynamic range of 50 dB. Once we have extracted the radiation center model from the ASAR image, we can reconstruct the frequency and aspect radiation patterns of the antenna-platform structure. The reconstruction

formula is essentially the Fourier transform of (7) and is given by

$$E^s(\omega, \phi, \theta) = \sum_n A_n \cdot e^{-jk(r_n + x_n)} \cdot e^{-jk_o \phi y_n} \cdot e^{-jk_o \theta z_n}. \quad (9)$$

By applying the above formula, we reconstruct the platform radiation patterns in frequency and aspect using the 150 radiation centers. Fig. 4(a) shows the comparison between the reconstructed frequency domain data and the original Apatch data calculated over the 0.56-GHz bandwidth about 10 GHz. The observation angle is along the nose. Fig. 4(b) shows the comparison between the reconstructed azimuth data calculated over the 3.33° window about the nose. The frequency is 10 GHz and the elevation angle is 0° . As shown from the graphs, good agreement is achieved between the reconstructed data and the original data over the frequency and aspect from which the radiation center model was generated.

III. RADIATION CENTER APPLICATIONS

In the previous section, it is shown that the radiation center model for an arbitrary antenna-platform configuration can be extracted using the ASAR-CLEAN methodology. In this section, we present two examples of the utilities of such radiation center representation.

A. Radiation Data Compression

The antenna radiation pattern on an electrically large platform is, in general, a very rapidly varying function of frequency and aspect. In this example, we shall demonstrate how the radiation center concept developed in the last section can be utilized to create a sparse model of the antenna-platform radiation over frequencies and aspect angles, thus achieving data compression. Note that for a complex platform, the radiation center model extracted at a particular observation angle is not expected to be valid over large angular extent. This is due to shadowing and other complex multiple scattering phenomena. Therefore, to fully characterize the antenna-platform radiation at all aspects, we need to extract 3-D radiation center models at various angles on a uniform grid in both elevation and azimuth. Once the radiation center models are extracted at all the angles on the grid, we can obtain the radiated field at any arbitrary angle by table lookup and reconstruction. The key question in this construct is the granularity of the grid, which, in practice, will depend on the platform complexity as well as the needed accuracy in the reconstruction. In our example, we restrict our attention to the azimuth direction, as shown in Fig. 5. The antenna-platform configuration is the same that shown in Fig. 1. First, the 3-D ASAR images for different observation angles in the azimuth direction are generated using Apatch. The angular granularity is chosen to be 5° so that a total of 72 images are generated in covering the full 360° azimuth in the zero elevation plane. Notice that only a one-time ray shoot is needed from the antenna in constructing the 72 ASAR images because of the bistatic nature of the ASAR scenario. This is contrary to the monostatic radar signature studies we have carried out previously [12]. We use a center frequency of 10 GHz and a bandwidth of 0.49 GHz. To

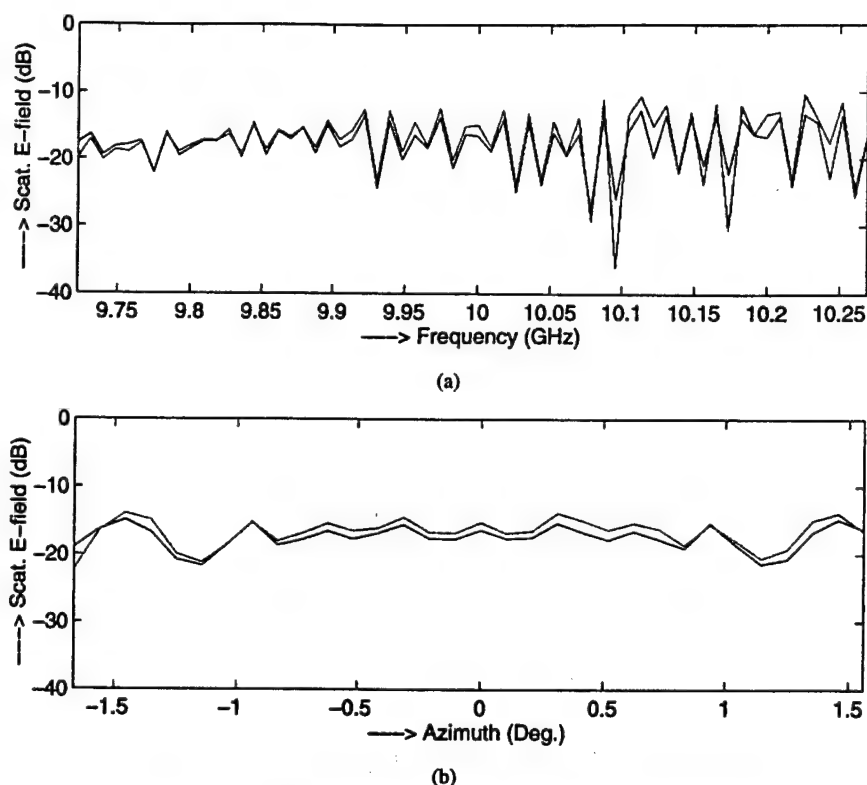


Fig. 4. Comparison of the original and the reconstructed radiation patterns. (a) Frequency sweep. (b) Azimuth sweep.

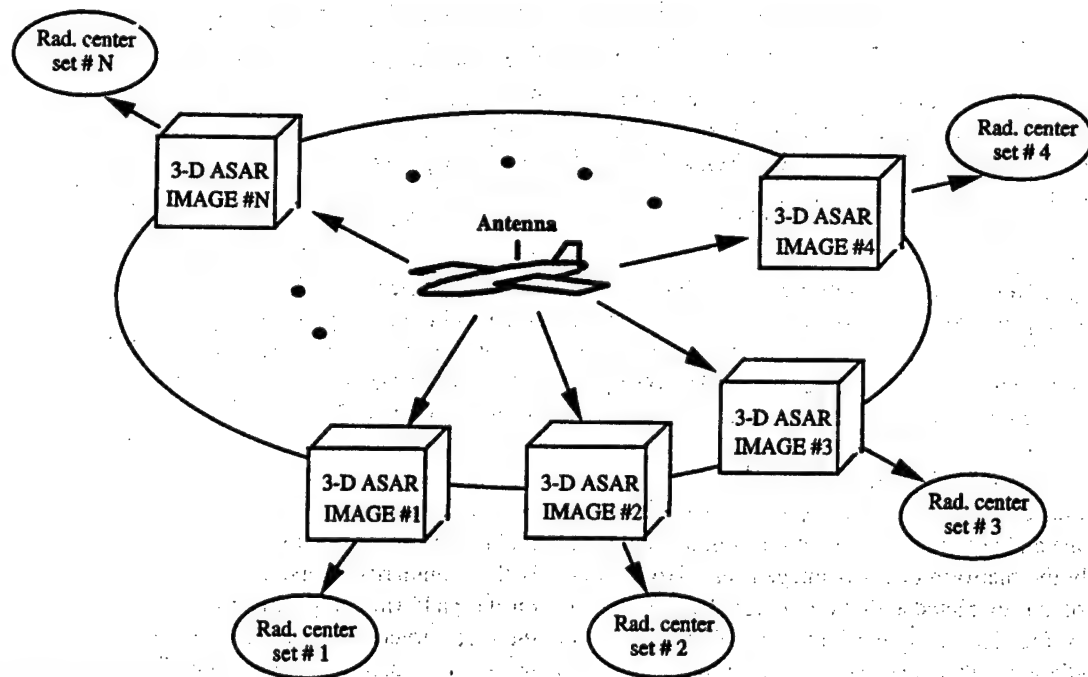


Fig. 5. Global radiation center representation of the radiation pattern along the azimuth cut obtained via ASAR image formation and radiation center extraction at various angles.

generate each ASAR image, the azimuth bandwidth is chosen to be 2.22° and the elevation bandwidth is taken as 2.46° .

Next, we extract 100 radiation centers from each of the 72 3-D ASAR images using CLEAN. Shown in Fig. 6 are four reconstructed ASAR images at 0° , 30° , 60° , and 90° with respect to the nose of the airplane. They are 2-D projected images

formed by summing up all the z -slices of the original 3-D images. We observe that there are some persistent hot spots on the nose and the right wing of the airplane, which appear to be visible in all four images, while other features have smaller visibility extent. To test the validity of the model, the platform radiation pattern in the 0° – 180° azimuth range is reconstructed

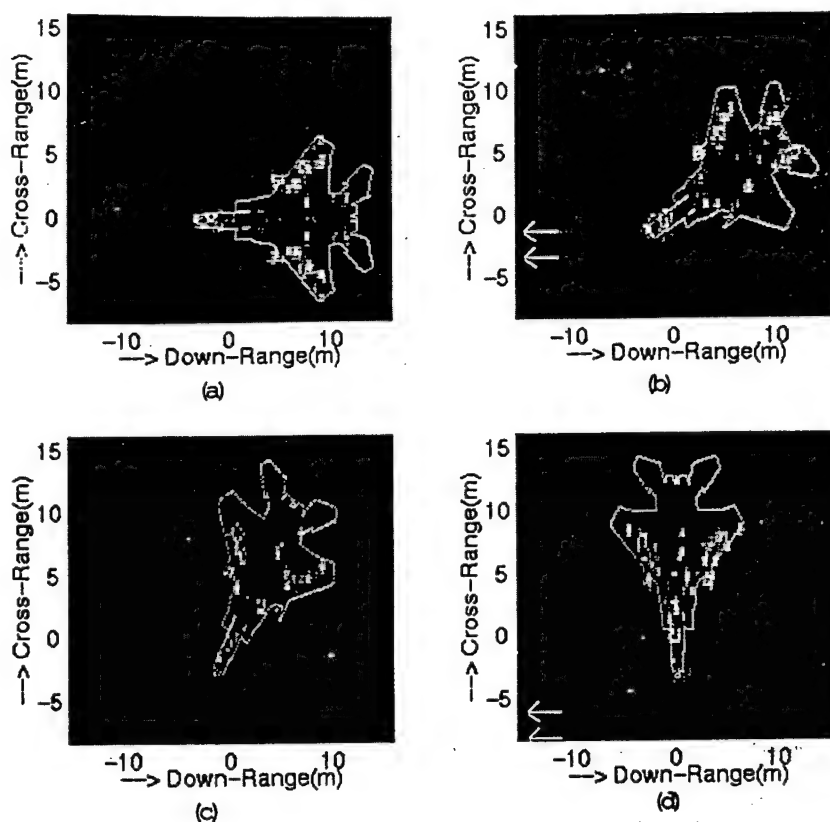


Fig. 6. 2-D projected ASAR images reconstructed from the radiation center model at different observation angles. (a) 0°. (b) 30°. (c) 60°. (d) 90°.

over each 5° sector by using the extracted radiation centers and (9). It is shown as the solid line in Fig. 7(a). Also plotted in dashed line in the figure is the original azimuth radiation pattern computed using Apatch at a granularity of 1°. Note that the reconstructed data can be computed to any desired fine angular granularity very rapidly from the radiation center model. The Apatch data, on the other hand, are computed very coarsely as it is very time-consuming to generate. The two curves show some agreement in overall trend, although the exact Apatch data are too grossly undersampled. In Fig. 7(b), the comparison between the two curves computed on the same fine granularity of 0.07° over the 30°–35° sector is shown. The reconstructed data from 30°–32.5° are reconstructed from one set of radiation centers while those from 32.5°–35° are reconstructed from another set. Note that the data between 31.11° and 33.89° correspond to “extrapolated” data based on the nearest-neighbor radiation center model. The overall agreement between the two sets of data are fairly good, even in the extrapolated region. We have also attempted to extend the extrapolation to a 10° window, and have noticed significant degradation in the outer regions of extrapolation. Therefore, the 5° granularity seems to be a good choice for this example. Reconstruction fidelity can be improved by using more radiation centers in the CLEAN procedure and by reducing the angular granularity. This, of course, is at the expense of model sparsity. Finally, the same philosophy can also be applied to the elevation direction to fully exploit the scheme for data compression. The data compression ratio achievable using the 3-D radiation center model can be roughly estimated as follows. We assume the original radiation data cover the entire vis-

ible sphere and 64 frequency samples. The original complex radiation data set, sampled at a granularity of 0.1°, requires a total storage space of $(360/0.1) * (180/0.1) * (64) * (8 \text{ bytes}) = 3.3 \text{ Gb}$. The radiation center model contains 100 radiation centers per angle, with each radiation center requiring the storage of five real numbers (three for the location and two for the complex amplitude). By using a 5° granularity to cover the entire visible sphere, the storage space required for the radiation center set amounts to $(360/5) * (180/5) * (100) * (5) * (4 \text{ bytes}) = 5.2 \text{ Mb}$. The data compression ratio is about 640 : 1. To summarize, we have shown that a global sparse radiation center model can be constructed. Once available, it can be used to reconstruct radiation data to a very fine granularity with good fidelity.

B. Platform Effect Reduction

In the second example, we shall utilize the radiation center representation to carry out a platform effect reduction study. Since the radiation centers pinpoint the locations of the dominant secondary scattering on the platform, one way to mitigate such undesirable effects is to place absorbers at those locations. This is analogous to carrying out signature reduction work using ISAR images as a guide. We use the same example as that in Section III-A and first generate the radiation center representations of the scattered field over 360° azimuth at 5° angular granularity. Next, those radiation centers that contribute more than -25 dB to the radiated field are pinpointed. To eliminate these radiation centers, we identify the facets on the target that correspond to the locations of the radiation centers and convert them from perfect conductors into perfect absorbers. By using this

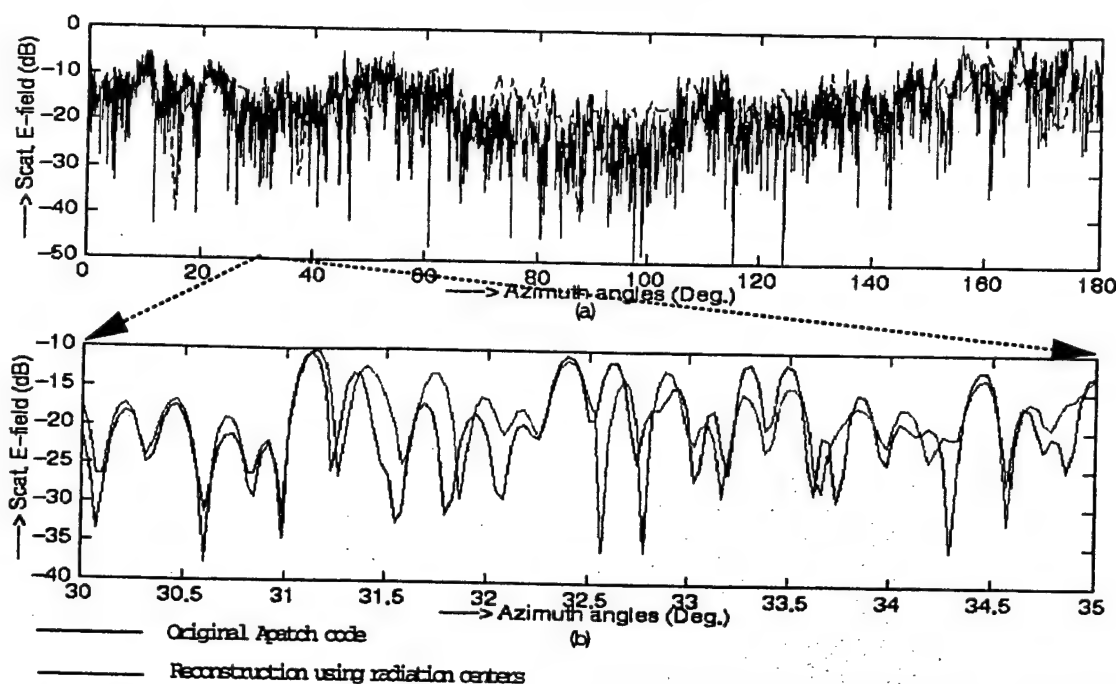


Fig. 7. Comparison of the azimuth radiation patterns from the original data and the reconstructed data based on radiation centers. (a) Coarse comparison between 0° and 180° . The original data are sampled at 1° while the reconstructed data are sampled at 0.07° . (b) Detailed comparison between 30° and 35° at the same fine angular granularity.

logic, we end up with 387 absorbing facets on the platform out of approximately 8000 facets that describe the airplane. The new CAD file is shown in Fig. 8(a), where the absorbing facets are marked in a darker shade. Fig. 9(a) shows the azimuth radiation pattern from the platform before and after the absorber coating. The patterns are computed by Apatch. We observe that the platform scattering is significantly reduced by using the absorbers. However, the resulting platform radiation level is not suppressed below the -25 -dB design level as expected. In particular the platform scattering near the 20° and 170° directions remains quite high. This can be explained by the fact that the ASAR imaging algorithm is based on the single-bounce assumption. Multiple-bounce mechanisms are not correctly mapped to the platform in the ASAR image, but are rather delayed in the down-range direction [1].

To circumvent this problem and further reduce the platform scattering from multiple bounce mechanisms, we devise a scheme to tie each radiation center back to the ray mechanism that gave rise to it. The basic idea is to save the hit point information of the ray which contributes the largest amount of energy to a particular ASAR image pixel during the SBR-based image formation process in (5). Consequently, during the CLEAN procedure, each extracted radiation center has an associated "hit point list" to allow tie-back of the radiation center to the specific hit point locations on the platform. Such tie-back information is only approximate, but has been found to be very useful in radar signature and target identification applications [12]. It is important to point out that this information can be extracted only if an SBR-based approach is used to generate the ASAR image. Using this new tie-back information for each radiation center, we can now place absorbers on those facets associated with the hit points on the target. In fact, we only need

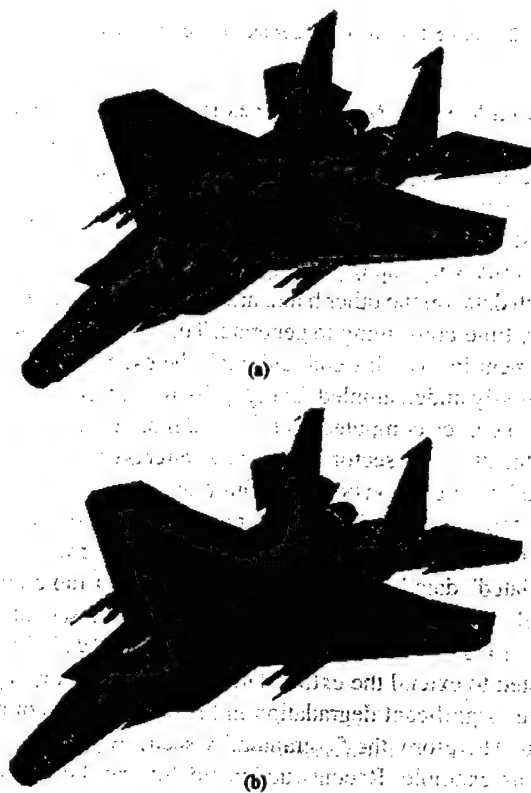


Fig. 8. CAD models with the absorbing facets shown in a darker shade. (a) Absorber placement using the first scheme in which the facet closest to a radiation center is changed into an absorber. (b) Absorber placement using the second scheme in which the hit point list for a radiation center is found via SBR and the facet from the first hit is changed into an absorber.

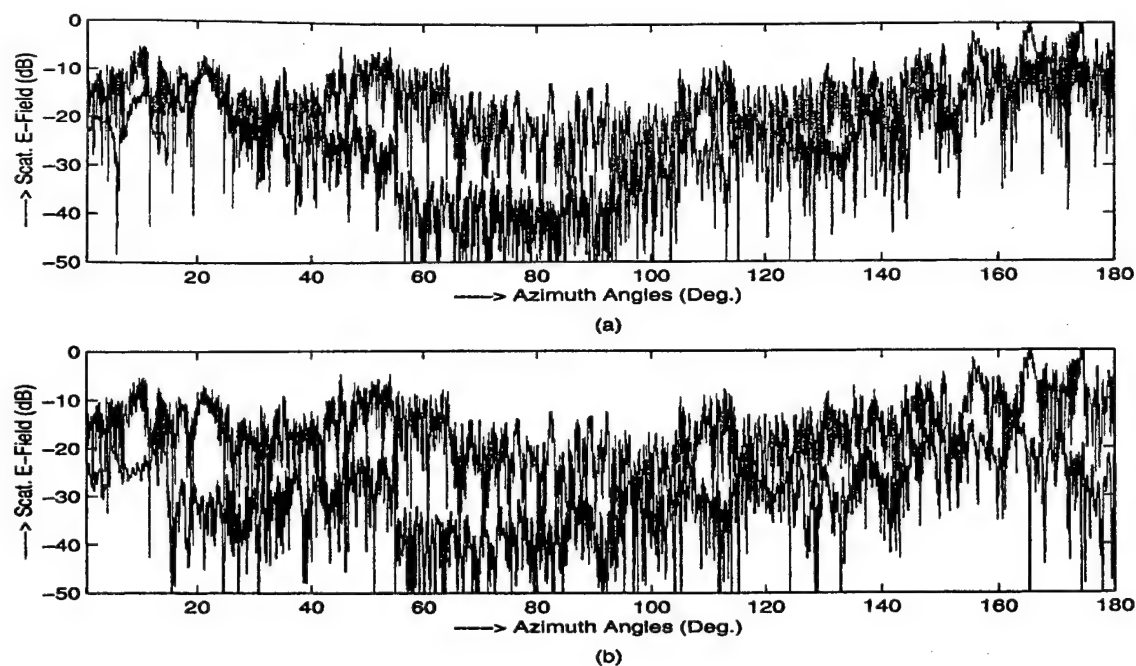


Fig. 9. Azimuth radiation patterns before and after putting absorbers on the platform. (a) Absorber placement according to the first scheme. (b) Absorber placement according to the second scheme.

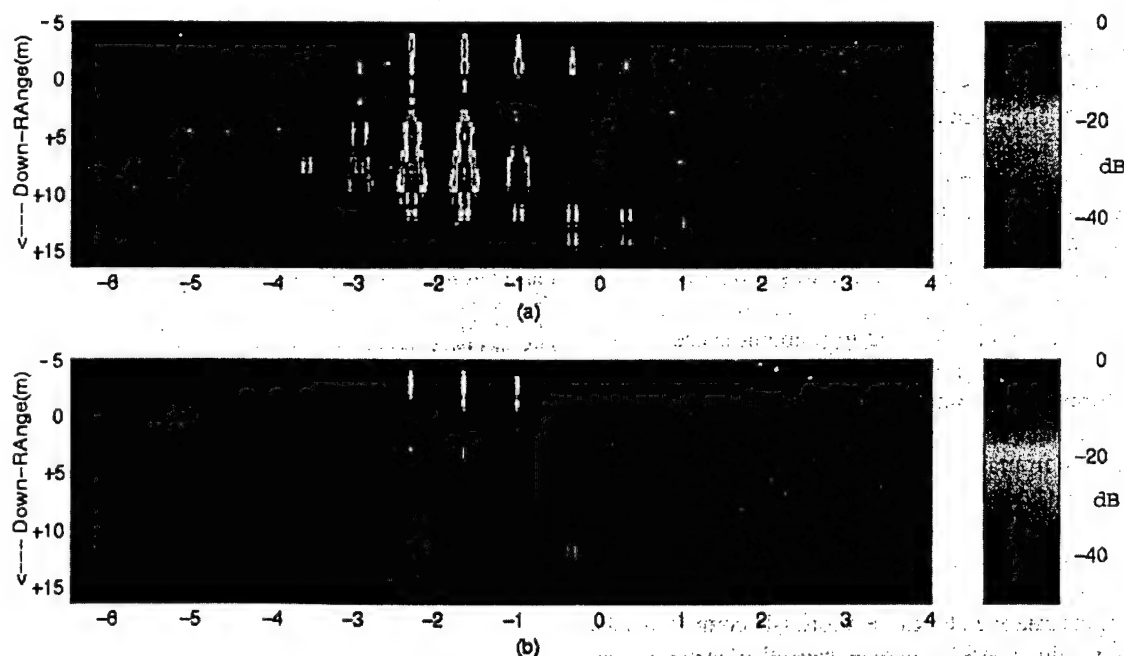


Fig. 10. 3-D ASAR images observed along the nose sector. (a) No absorbers. (b) With absorbers.

to put an absorber on any one of the hit points to eliminate the contribution. We have chosen to do so for all the first-bounce facets. A total of 403 absorbing facets on the platform are selected in this manner out of the 8000 facets. Fig. 8(b) shows the absorber-coated airplane model. Note the difference in the absorbing facet locations in Fig. 8(a) and (b). Fig. 9(b) shows the platform scattering pattern resulting from this approach. The scattering pattern of the uncoated platform is again plotted in the figure for reference. We can see that the radiation from the platform is now much better suppressed when compared to

the first scheme. The scattered field from the platform comes fairly close to meeting the -25 -dB design level at most of the angles. In particular the platform scattering at 20° and 170° directions is well suppressed. Fig. 10(a) and (b) shows the 3-D ASAR images of the platform scattering along the nose sector before and after the absorber treatment, respectively. We observe that the platform image nearly vanishes after the absorber coating, with the remaining stray radiation coming from the nose portion of the airplane. Note that in this example the absorber coating is placed on only one facet for each

radiation center selected, no matter how small the facet. Since a radiation center is formed by the coherent radiation from the induced current over some finite region of the platform, some minimum area may be required to more effectively eliminate the radiation from each scattering center. We believe this is the cause for the remaining stray radiation, especially near the nose and the back of the airplane, where the facets in the CAD model are very small.

In this example, we have carried out an exercise to suppress platform radiation by selectively coating the platform from the radiation center information. The first scheme is simply based on placing absorbers at the radiation center location. It works well for suppressing the single-bounce mechanisms. The second improved scheme is based on the hit point list generated during the radiation center extraction procedure. It improves performance by more effectively tracking the locations of the multibounce mechanisms. However, this scheme is more restrictive since it requires the SBR simulation algorithm be used for ASAR image formation.

IV. CONCLUSION

In this paper, we presented a sparse representation of antenna radiation pattern on a complex platform. This representation is based on a point radiator model that describes the radiation pattern by a collection of radiation centers on the platform. The methodology for obtaining the radiation center model is to first generate the 3-D antenna synthetic aperture radar imagery of the platform and then to parameterize the resulting image by a collection of point radiators via the CLEAN algorithm. It was shown that once such a representation is obtained, we can reconstruct and extrapolate antenna radiation patterns over frequencies and aspects with good fidelity, thus achieving high data compression ratio. Furthermore, it was shown that when coupled with the SBR simulation engine, the resulting radiation center information can be used to pinpoint cause-and-effect in platform scattering and provide important guidelines for reducing platform effects. Finally, we should point out that the data used throughout this paper were based on ray-tracing simulation. Validation from measurement or more rigorous numerical data was not attempted. However, we have since carried out the same radiation center modeling using the computational electromagnetics data from a full-wave simulator. That result is being reported in [13]. It is shown that the conclusions reached in this paper holds true even for more rigorously computed data. Measurement results of ASAR images have also been reported recently in []

REFERENCES

- [1] C. Ozdemir, R. Bhalla, L. C. Trintinalia, and H. Ling, "ASAR—Antenna synthetic aperture radar imaging," *IEEE Trans. Antennas Propagat.*, vol. 46, pp. 1845–1852, Dec. 1998.
- [2] S. W. Lee, *User's Manual for APATCH*. Champaign, IL: DEMACO, Inc., Oct. 1992, version 1.0.
- [3] H. Ling, R. Chou, and S. W. Lee, "Shooting and bouncing rays: Calculating the RCS of an arbitrary shaped cavity," *IEEE Trans. Antennas Propagat.*, vol. 37, pp. 194–205, Feb. 1989.
- [4] J. Baldauf, S. W. Lee, L. Lin, S. K. Jeng, S. M. Scarborough, and C. L. Yu, "High frequency scattering from trihedral corner reflectors and other benchmark targets: SBR versus experiment," *IEEE Trans. Antennas Propagat.*, vol. 39, pp. 1345–1351, Sept. 1991.
- [5] R. Bhalla and H. Ling, "A fast algorithm for signature prediction and image formation using the shooting and bouncing ray technique," *IEEE Trans. Antennas Propagat.*, vol. 43, pp. 727–731, July 1995.
- [6] —, "Three-dimensional scattering center extraction using the shooting and bouncing ray technique," *IEEE Trans. Antennas Propagat.*, vol. 44, pp. 1445–1453, Nov. 1996.
- [7] W. P. Yu, L. G. To, and K. Ooi, "N-point scatterer model RCS/glint reconstruction from high-resolution ISAR target imaging," in *Proc. End Game Measurement and Modeling Conference*, Point Mugu, CA, Jan. 1991, pp. 197–212.
- [8] N. Y. Tseng and W. D. Burnside, "A very efficient RCS data compression and reconstruction technique," *ElectroSci. Lab., Ohio State Univ., Columbus, OH, Tech. Rep. 722 780-4*, Nov. 1992.
- [9] S. Y. Wang and S. K. Jeng, "Generation of point scatterer models using PTD/SBR technique," in *IEEE Antennas Propagat. Symp. Dig.*, Newport Beach, CA, June 1995, pp. 1914–1917.
- [10] A. Selalovitz and B. D. Frieden, "A 'CLEAN'-type deconvolution algorithm," *Astronom. Astrophys.*, vol. 70, pp. 335–343, 1978.
- [11] J. Tsao and B. D. Steinberg, "Reduction of sidelobe and speckle artifacts in microwave imaging: The CLEAN technique," *IEEE Trans. Antennas Propagat.*, vol. 36, pp. 543–556, Apr. 1988.
- [12] R. Bhalla, J. Moore, and H. Ling, "A global scattering center representation of complex targets using the shooting and bouncing ray technique," *IEEE Trans. Antennas Propagat.*, vol. 45, pp. 1850–1856, Dec. 1997.
- [13] T. Su, C. Ozdemir, and H. Ling, "On extracting the radiation center representation of antenna radiation patterns on a complex platform," *Microwave Opt. Tech. Lett.*, vol. 26, pp. 4–7, July 2000.
- [14] T.-H. Chu and C.-J. Pan, "Microwave diversity imaging using ASAR approach," *IEEE Antennas Propagat. Symp. Dig.*, pp. 1952–1955, July 2000.

Caner Ozdemir (S'95–M'97) was born in Edremit, Turkey, on March 29, 1971. He received the B.S. degree in electrical and electronics engineering in 1992, from the Middle-East Technical University (METU), Ankara, Turkey, and the M.S. and Ph.D. degrees in electrical and computer engineering from the University of Texas at Austin, in 1995 and 1998, respectively.

From 1992 to 1993, he worked as a Project Engineer at the electronic warfare office of the Turkish Military Electronics Industries (ASELSAN), Ankara, Turkey. From 1998 to 2000 he was a Research Scientist at Advanced Systems Technology Group (ASTG), Honeywell, Inc., Columbia, MD. Currently, he is a Faculty Member at the Electrical and Electronics Engineering Department, Mersin University, Mersin, Turkey. His primary research interests are radar signal processing and imaging, electromagnetic scattering, antenna design techniques, and computational electromagnetic.

Rajan Bhalla, photograph and biography not available at time of publication.

Hao Ling (S'83–M'86–SM'92–F'99), photograph and biography not available at time of publication.

ON EXTRACTING THE RADIATION CENTER REPRESENTATION OF ANTENNA RADIATION PATTERNS ON A COMPLEX PLATFORM

Tao Su¹, C. Ozdemir,² and Hao Ling¹

¹ Department of Electrical and Computer Engineering
University of Texas at Austin
Austin, Texas 78712

² Dept. of Electrical Engineering
Mersin University, Turkey

Received 2 February 2000

ABSTRACT: Using full-wave computational electromagnetics data, we demonstrate that the radiated field from an antenna on a complex platform can be sparsely represented by a radiation center model. An extraction scheme based on the matching-pursuit algorithm is devised to extract the model parameters from multifrequency, multiaspect radiation data. To accelerate the parameterization procedure, the previously developed antenna synthetic aperture radar imaging algorithm is used to provide an initial estimate of the radiation center position during the search. It is shown that the resulting radiation center model provides a sparse, physical representation of the antenna-platform interaction. © 2000 John Wiley & Sons, Inc. *Microwave Opt Technol Lett* 26: 4–7, 2000.

Key words: radiation center model; antenna-platform interaction; matching-pursuit algorithm

I. INTRODUCTION

In antenna analysis and design, the mounting platform can have a significant effect on the antenna radiation characteristics. In addition to the forward problem of characterizing the antenna radiation in the presence of the platform, also of importance is the development of a sparse model to describe the radiation physics in antenna-platform interaction. Toward this end, we have previously proposed a point radiator model to represent the complex radiation patterns resulting from antenna-platform interactions [1, 2]. In this model, we assume that the platform scattering due to the primary antenna radiation can be approximately described by a set of "radiation centers" on the platform. This concept is similar to the scattering center model widely used in radar scattering, where the high-frequency scattering from a complex target often can be modeled efficiently by a sparse set of point scatterers on the target [3–6]. To extract the radiation center model from a multifrequency, multiaspect antenna radiation pattern, we have proposed a parameterization scheme based on microwave imaging. The procedure entails first generating the 3-D antenna synthetic aperture radar (ASAR) imagery of the platform, and then parameterizing the resulting image by a collection of point radiators via the CLEAN algorithm. It was shown that, once such a representation is obtained, we can rapidly reconstruct antenna radiation patterns over frequencies and aspects with good fidelity. Thus, such a model can be used for the real-time reconstruction of complex antenna patterns in high-level system simulations. Furthermore, the resulting radiation center information can be used to pinpoint cause-and-effect in platform scattering, and to provide design guidelines for antenna placement and optimization. However, the method was based on a Fourier-based

Contract grant sponsor: Office of Naval Research

Contract grant number: N00014-98-1-0178

algorithm that relied on a number of small-angle, small-bandwidth approximations. When these conditions are not met, the resulting parameterization is no longer sparse. In addition, the concept was only tested using data from high-frequency ray-tracing simulation [7].

In this paper, we overcome the above deficiencies by: 1) developing a more generalized algorithm based on matching pursuit [8] to extract the radiation center model from frequency-aspect data, and 2) demonstrating the algorithm using computational electromagnetics (CEM) data from the full-wave numerical solver FISC [9]. In the matching-pursuit algorithm, the radiation center model is extracted via an iterative projection process. During each stage of the iteration, the basis function associated with each possible radiation center position is projected onto the radiation data. The point that maximizes the projection coefficient is selected as a radiation center, and its contribution is subtracted from the total radiated field. This process is repeated until the energy in the residual signal has reached a sufficiently small level. To accelerate the exhaustive search process during each iteration, the ASAR image is used to obtain an initial estimate of the radiation center position before the fine search for its precise location. By applying this algorithm to full-wave CEM simulation data, we demonstrate that the secondary radiation from a complex platform can be compactly represented by a relatively small number of radiation centers.

II. RADIATION CENTER MODEL AND ITS PARAMETERIZATION

The model that we will adopt assumes that the secondary radiation from the platform due to the primary radiation from an antenna can be described by a set of radiation centers. For each radiation center located at position (x_0, y_0, z_0) (see Fig. 1), the corresponding radiated field as a function of frequency and aspect can be written as

$$E^r(f, \theta_1, \theta_2) = Ae^{-jkr_0} e^{jk(x_0 \cos \theta_1 \cos \theta_2 + y_0 \cos \theta_1 \sin \theta_2 + z_0 \sin \theta_1)} \quad (1)$$

where $k = 2\pi f/c$ is the wavenumber, $r_0 = \sqrt{x_0^2 + y_0^2 + z_0^2}$ is the distance from the antenna to the radiation center, and the angles θ_1 and θ_2 are defined with respect to the local coordinate system in which the x -axis points toward the central observation direction (see Fig. 1). Note that the phase factor in (1) accounts for the path delay from the antenna to the radiation center, and then to the observation direction in the far field. When this model is used to describe the secondary radiation from a complex platform, the total field can be expressed as a sum of the fields due to all of the radiation

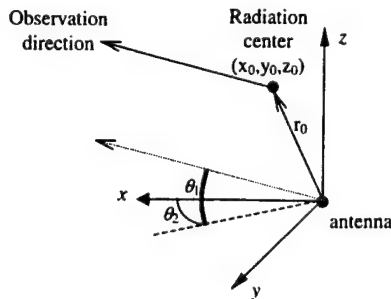


Figure 1 Radiation center model for the secondary platform radiation

centers:

$$\begin{aligned} E_{\text{total}}^r(f, \theta_1, \theta_2) &= \sum_i E_i^r(f, \theta_1, \theta_2) \\ &= \sum_i A_i \Phi_i(f, \theta_1, \theta_2, x_i, y_i, z_i). \end{aligned} \quad (2)$$

The function Φ_i includes the exponential terms in (1), and is the basis function due to the i th radiation center. Given the radiated field as a function of frequency and aspect, our goal is to determine a model that best approximates the radiated field with as few radiation centers as possible. The unknown parameters are the position of the radiation centers (x_i, y_i, z_i) and their strength A_i .

Note that, due to the presence of the e^{-jkr_0} term, the usual Fourier relationship does not exist between the frequency-aspect variables and the position of the radiation centers. In addition, since the basis functions are not strictly orthogonal, the simultaneous projection of the radiation data onto these bases will result in strong interference among the bases. To overcome this problem, we adopt the matching-pursuit algorithm [8] to extract the model parameters iteratively. In each step of the iteration, we project the radiated field onto every possible radiation center basis in 3-D space. The location that gives the largest projection is chosen as the strongest radiation center. The search can be expressed as

$$A = \max_{(x, y, z)} \{ \langle E^r, \Phi(x, y, z) \rangle \} \quad (3)$$

where the inner product is defined as

$$\langle E^r, \Phi \rangle = \int_f \int_{\theta_1} \int_{\theta_2} E^r \Phi^* df d\theta_1 d\theta_2. \quad (4)$$

Once the strongest radiation center is determined, its associated radiated field is subtracted from the total radiated field to generate

$$E_{i+1}^r = E_i^r - A_i \Phi_i. \quad (5)$$

Since the strongest radiation center is removed from the signal, its interference on the weaker radiation centers is minimized. This process is repeated to search for subsequent radiation centers, and the process terminates when the remainder of the energy in the radiated field has reached a sufficiently small level. At the end of the iteration process, a radiation center representation is obtained to represent the original radiated field.

A problem with the matching-pursuit algorithm is that it requires exhaustive search over 3-D space during each iteration of the extraction procedure. This can be prohibitively time consuming. To reduce the search time, we apply the approximate Fourier-based ASAR algorithm [1] to first estimate the position of the strongest radiation center before carrying out an exhaustive fine search around this neighborhood. The ASAR imaging algorithm is derived by applying the small-bandwidth, small-aspect approximations to the phase terms in (1):

$$\begin{aligned} k_x &= k \cos \theta_1 \cos \theta_2 \approx k \\ k_y &= k \cos \theta_1 \sin \theta_2 \approx k_c \theta_2 \\ k_z &= k \sin \theta_1 \approx k_c \theta_1 \end{aligned} \quad (6)$$

where k_c is the wavenumber at the center frequency. Substituting (6) into (1), we can write the radiated field as

$$E'(f, \theta_1, \theta_2) = Ae^{-jk(r_0-x_0)}e^{jk\theta_2 y_0}e^{jk\theta_1 z_0}. \quad (7)$$

Note that (7) implies a Fourier relationship between $(r_0 - x_0, y_0, z_0)$ and (f, θ_1, θ_2) . Therefore, by Fourier transforming the radiated field, we obtain an image in the $(r - x, y, z)$ space. The point with the highest value in the image is associated with the strongest radiation center. We can further obtain its (x, y, z) position by using the transformation

$$x = \frac{1}{2} \left(\frac{(y^2 + z^2)}{u} - u \right) \quad (8)$$

where $u = r - x$. We found that, when the small-bandwidth, small-angle conditions are not satisfied, the ASAR image still provided a fair estimate of the strongest radiation center position. Therefore, during the search process in the matching pursuit, we use the ASAR algorithm to carry out a fast, coarse search of the position of the strongest radiation center. We then zoom in on the precise location of the radiation center via a fine search. As a result, the total number of search points is reduced, and the resolution can be improved.

III. NUMERICAL RESULTS

In this section, we validate the radiation center model with antenna-platform radiation data generated via CEM simulation. The computation is carried out with FISC [8], which is a method-of-moments solver based on the multilevel fast multipole method. The layout of the antenna-platform structure is shown in Figure 2. The ship-like platform is 10 m in length and 2.5 m in height. The antenna is a short dipole, and is placed 2 m above the deck. We compute the radiated field with FISC at a center frequency of 1.0 GHz and a bandwidth of 500 MHz. The center observation angle is $\phi_{el} = 40^\circ$, $\phi_{az} = 50^\circ$, and the angular range is about 23° in both azimuth and elevation angles. To reduce the error in the ASAR algorithm resulting from applying the small-angle approximation to a fairly large observation range (23°), we use the actual wavenumbers (k_x, k_y, k_z) to replace the frequency and angles (k, θ_1, θ_2) in (7). The radiated field is computed uniformly in the (k_x, k_y, k_z) space.

We first consider the source dipole parallel to the deck, and extract the radiation centers using the procedure described in the previous section. The first 20 radiation centers are shown in Figure 3. The strengths of the radiation centers are represented by different colors. We observe that the

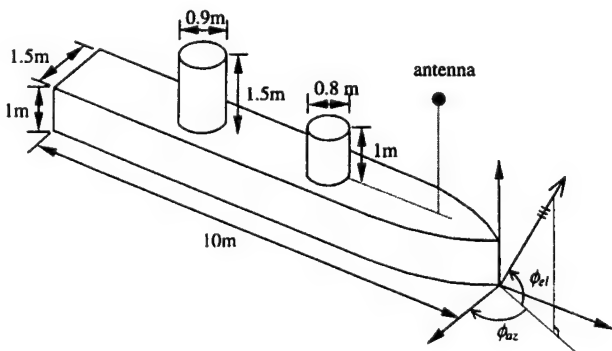


Figure 2 Layout of the antenna-platform radiation problem

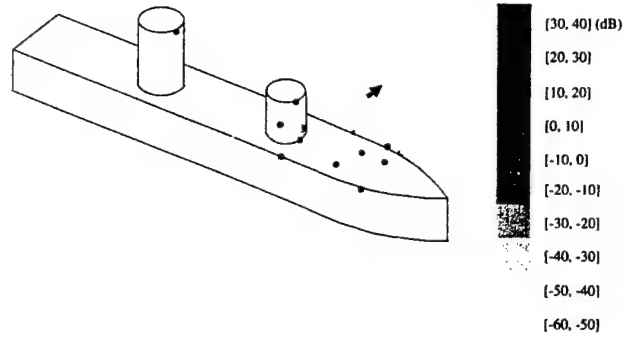


Figure 3 Extracted point scatterers for horizontal dipole antenna on the platform

dominant platform scattering comes from the bow of the ship and the top-hat structure formed by the cylinder and deck. Once the radiation center model is obtained, the radiated field easily can be reconstructed using the model. Figure 4(a) is a plot of the original radiated field as a function of k_x and k_y which, according to (6), are approximately proportional to

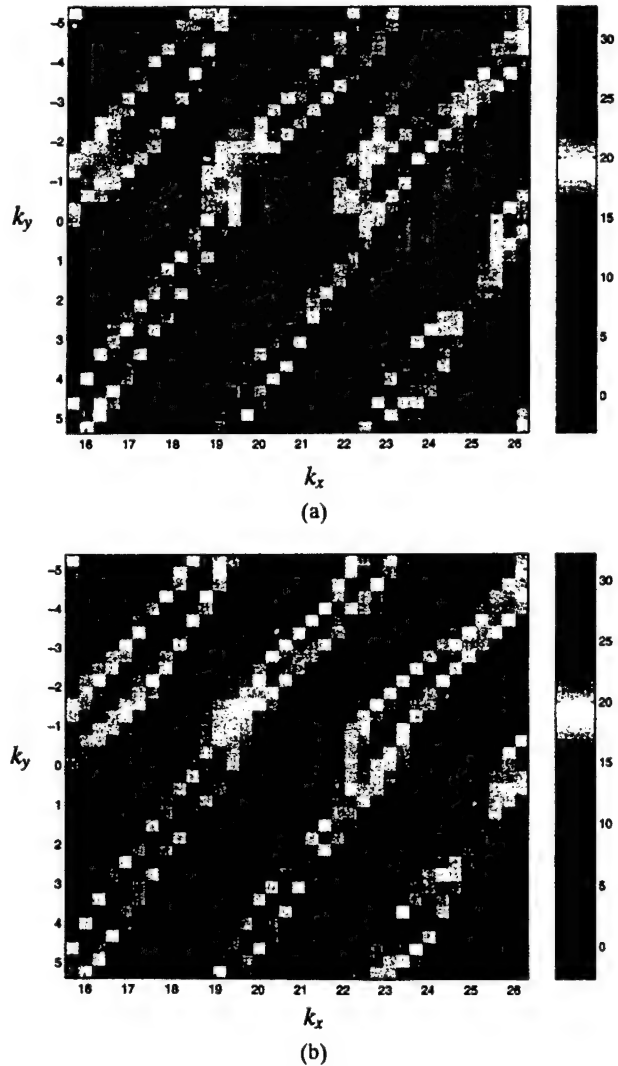


Figure 4 Comparison of original and reconstructed radiation pattern at $k_z = 0$. (a) Computed by FISC. (b) Reconstructed from radiation center model

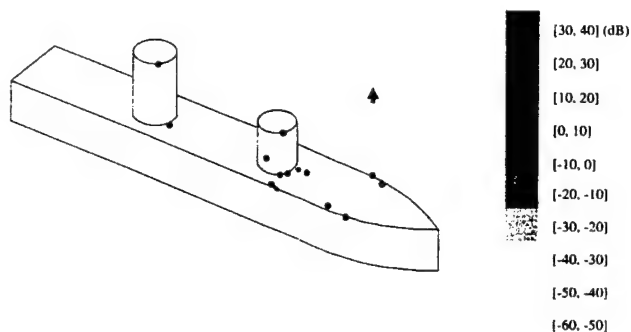


Figure 5 Extracted radiation centers for vertical dipole antenna on the platform

the frequency and relative azimuth angle, respectively. k_z is set to be 0. The field reconstructed from the first 20 radiation centers is shown in Figure 4(b). We observe that the qualitative agreement between Figure 4(a) and (b) is good. We also compute the correlation index between the two figures using

the formula

$$R = \frac{\int \int E_1^*(k_x, k_y) E_2(k_x, k_y) dk_x dk_y}{\frac{1}{2} \int \int (|E_1(k_x, k_y)|^2 + |E_2(k_x, k_y)|^2) dk_x dk_y} \quad (9)$$

The resulting correlation index is 0.958, showing quantitatively that the actual field can be fairly well reconstructed by the radiation center model.

Next, we consider the dipole vertical to the deck, and repeat the same procedure. The first 20 radiation centers are plotted in Figure 5. Their positions indicate that a strong interaction still comes from the edges and corners of the platform. But compared to the horizontal dipole example, there are no radiation centers on the deck directly under the antenna. This is because the radiated field from the vertical dipole is small in that direction. The original radiated field is plotted in Figure 6(a) as a function of k_y and k_z , which are approximately proportional to the relative azimuth and elevation angles, respectively. k_x is set to be 0. The field reconstructed from the model is shown in Figure 6(b). Again, the agreement between the two is good. The correlation index between the two is 0.978.

IV. CONCLUSIONS

In this paper, we have demonstrated, using full-wave CEM simulation data, that the radiated field from an antenna on a complex platform can be sparsely represented by a radiation center model. A matching-pursuit algorithm is devised to determine the model parameters. The previously developed ASAR imaging algorithm is used to accelerate the parameterization procedure. The resulting radiation center model provides a sparse, physical representation of the antenna-platform interaction.

REFERENCES

1. C. Ozdemir, R. Bhalla, L.C. Trintinalia, and H. Ling, A SAR—Antenna synthetic aperture radar imaging, *IEEE Trans Antennas Propagat* 46 (1998), 1845–1852.
2. C. Ozdemir, R. Bhalla, and H. Ling, A radiation center representation of antenna radiation patterns on a complex platform, *IEEE Trans Antennas Propagat* (submitted, Dec. 1997).
3. R. Bhalla, H. Ling, J. Moore, D.J. Andersh, S.W. Lee, and J. Hughes, 3D scattering center representation of complex targets using the shooting and bouncing ray technique: A review, *IEEE Antennas Propagat Mag* 40 (1998), 30–39.
4. W.P. Yu, L.G. To, and K. Oii, N-point scatterer model RCS/glint reconstruction from high-resolution ISAR target imaging, *Proc End Game Meas Modeling Conf*, Point Mugu, CA, Jan. 1991, pp. 197–212.
5. M.P. Hurst and R. Mittra, Scattering center analysis via Prony's method, *IEEE Trans Antennas Propagat* AP-35 (1987), 986–988.
6. N.Y. Tseng and W.D. Burnside, A very efficient RCS data compression and reconstruction technique, tech rep 722780-4, Electro-Science Lab., Ohio State University, Nov. 1992.
7. User's manual for APATCH, version 1.0, DEMACO Inc., Champaign, IL, Oct. 1992.
8. S.G. Mallat and Z. Zhang, Matching pursuit with time-frequency dictionaries, *IEEE Trans Signal Processing* 41 (1993), 3397–3415.
9. User's manual for FISC (fast Illinois solver code), Center for Computational Electromagnetics, University of Illinois at Urbana-Champaign and DEMACO, Inc., IL, Jan. 1997.

© 2000 John Wiley & Sons, Inc.

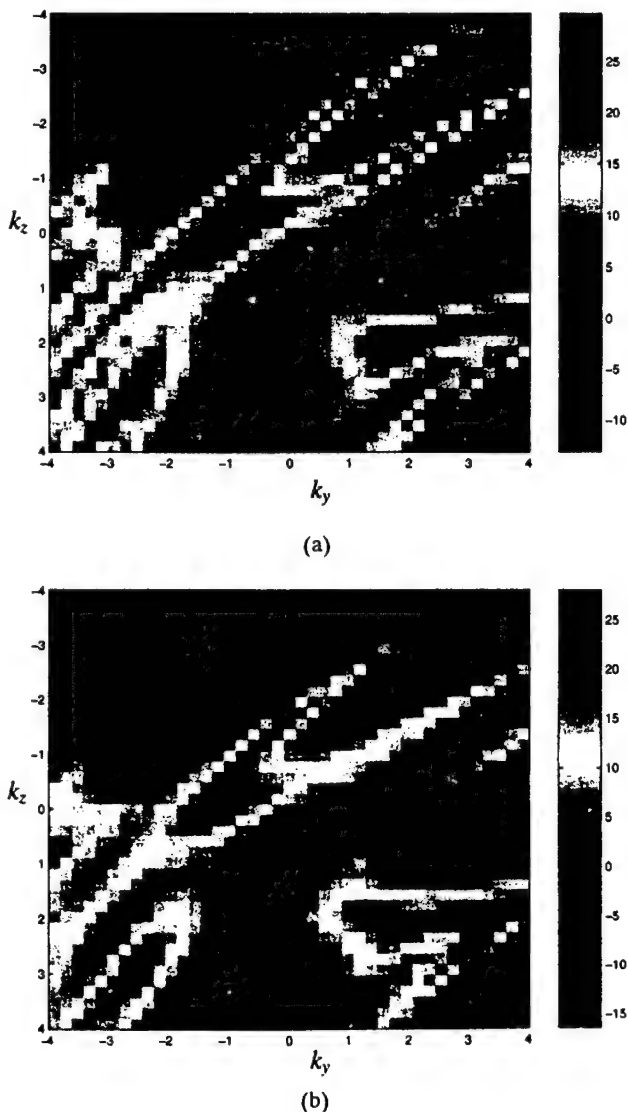


Figure 6 Comparison of original and reconstructed radiation pattern at $k_x = 0$. (a) Computed by FISC. (b) Reconstructed from radiation center model

A Frequency-Aspect Extrapolation Algorithm for ISAR Image Simulation Based on Two-Dimensional ESPRIT

Yuanxun Wang, *Member, IEEE*, and Hao Ling, *Fellow, IEEE*

Abstract—A frequency-aspect extrapolation algorithm is proposed to accelerate ISAR image simulation using fast multipole solvers. A two-dimensional (2-D) multiple-arrival model based on high-frequency physics is proposed to parameterize the induced currents on the target. A 2-D estimation of parameters via rotation invariance technique (ESPRIT) algorithm is developed to estimate the model parameters from a limited number of computed data samples in frequency and aspect. The model is then extrapolated to other frequencies and aspects to arrive at broadband, wide-angle radar cross section (RCS) data for inverse synthetic aperture radar (ISAR) image construction. This algorithm is tested using a canonical cylinder-plate structure to evaluate its performance. The ISAR image of the benchmark VFY-218 airplane at UHF band is then predicted using the fast multipole solver FISC and the 2-D extrapolation algorithm. The resulting image compares favorably with that obtained from chamber measurement data.

Index Terms—Fast multipole solver, frequency-aspect extrapolation, ISAR image simulation, two-dimensional ESPRIT.

I. INTRODUCTION

INVERSE synthetic aperture radar (ISAR) imaging is an important tool for radar signature diagnostic and target identification [1], [2]. In order to simulate the ISAR image of a target, it is necessary to solve the electromagnetic scattering problem at multiple frequencies and angles. Then, by performing a two-dimensional (2-D) Fourier transform on the resulting frequency-aspect radar cross section (RCS) data, a 2-D ISAR image of the target can be constructed. In this work, we consider ISAR image simulation of complex targets using a full-wave numerical technique. The focus of our attention is the class of iterative solvers based on the fast multipole method [3], [4]. These solvers have much lower computational complexity than traditional moment method (MoM) for scattering problems at a single frequency and a single observation angle. For multiple frequency-aspect RCS calculations, however, the solver has to be executed repeatedly for each angle and frequency.

To reduce the computation burden incurred by multiple frequency-aspect calculations, the concept of model-based parameter estimation can be applied to populate the required data set from a sparse set of computed data [5]–[12]. In particular, we

have recently developed a one-dimensional (1-D) frequency extrapolation algorithm [10], [12] and a 1-D angular extrapolation algorithm [11] to predict the high-frequency RCS of complex targets. Our approach is based on modeling the induced current on the target using a multiple-arrival model that closely resembles the ray-optical behavior at high frequencies. The model coefficients are determined by the superresolution estimation of parameters via rotation invariance technique (ESPRIT) algorithm [13], [14]. In this paper, we extend our algorithm to two dimensions to carry out simultaneous frequency-aspect extrapolation. We begin by proposing a 2-D multiple-arrival model in the frequency-aspect domain. Next, we implement a 2-D ESPRIT algorithm [15], [16] to estimate the model coefficients from a limited number of frequency-aspect current data computed using a fast multipole solver. Once the model is determined, the currents, and subsequently the RCS at other frequencies and aspects, can thus be computed.

This paper is organized as follows. In Section II, we examine the frequency and angular dependency of the current phase and propose a multiple-arrival model in the frequency-aspect domain. In Section III, a 2-D ESPRIT algorithm is developed and applied to estimate the time-of-arrival and cross range parameters in the frequency-aspect model from a few calculated frequency-aspect samples. In Section IV, the extrapolation algorithm is tested on a canonical 2-D cylinder-plate structure. The result is compared against both the exact result and that obtained by using the well-known bistatic approximation in angle [12], [17], [18]. The extrapolated results are also generated as a function of the number of calculated samples to investigate the convergence of the algorithm. Finally, we apply the algorithm to extrapolate the RCS and generate a 2-D ISAR image of the VFY-218 airplane at UHF band. The extrapolated result is compared to the image obtained from chamber measurement data [19]. Conclusions are given in Section V.

II. TWO-DIMENSIONAL MODEL FOR FREQUENCY-ASPECT EXTRAPOLATION

We shall first formulate a physical model for the current induced on the surface of a target due to an incident wave. The induced current at any point is in general the result of multiply incident waves from both the direct excitation and multiple scattering from other parts of the target. Therefore, we postulate that the induced current can be written as a sum of multiple incident waves, each with a different travel paths, as shown in Fig. 1. If we denote the down-range direction with respect to the incident

Manuscript received August 30, 1999; revised April 6, 2000. This work was supported in part by the Air Force MURI Center for Computational Electromagnetics under Contract AFOSR F49620-96-1-0025 and the Office of Naval Research under Contract N00014-98-1-0178.

The authors are with the Department of Electrical and Computer Engineering, University of Texas, Austin, TX 78712-1084 USA (e-mail: ling@ece.utexas.edu).

Publisher Item Identifier S 0196-2892(00)05909-X.

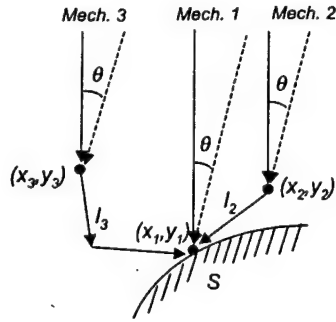


Fig. 1. Multiple-arrival model for the induced current.

wave as x and the cross range direction as y , the current at S as a function of frequency f can be written as

$$J(f, S) = \sum_{k=1}^K A_k e^{-j \frac{2\pi f}{c} d_k}, d_k = x_k + l_k \quad (1)$$

where K is the number of incident waves arriving at S , and c is the speed of light in free space. In the above definition of the path length d_k , we let (x_k, y_k) be the first hit point on the target due to the incident wave and l_k be the total intermediate path length of the multiple scattering mechanism from the first hit point to point S . A_k is the amplitude coefficient for each mechanism and is assumed to be frequency independent. Among the three mechanisms illustrated in Fig. 1, mechanism 1 is the direct incident wave from the source. Therefore, $l_1 = 0$, and (x_1, y_1) corresponds to point S . Mechanisms 2 and 3 are, respectively, a once-scattered and a twice-scattered wave before arriving at S . At high frequencies, this model is expected to be quite sparse, i.e., only a few terms are needed to adequately describe the scattering physics at an arbitrary point S on the target surface. This 1-D model was used to achieve frequency extrapolation at a fixed aspect angle in our earlier work [10], [12].

Angular dependency can also be incorporated in the above model. We assume that all the intermediate scattering points and the amplitude coefficient for each mechanism remain fixed as the incident angle is varied, as illustrated in Fig. 1. This assumption was found to be fairly accurate for ray-optical fields under small angular variation [20]. We have also applied it to achieve angular extrapolation at a fixed frequency for iterative moment solvers [11]. When we combine the aspect behavior with the frequency model in (1), we arrive at the following model for the current as a function of both frequency and incident angle

$$J(f, \theta, S) = \sum_{k=1}^K A_k e^{-j \frac{2\pi f}{c} (x_{ki} \cos \theta + y_{ki} \sin \theta + l_{ki})}. \quad (2)$$

Equation (2) contains three unknowns in the phase function of each mechanism. Next, we use the small-angle approximation $\cos \theta \approx 1$ to arrive at an expression with two unknowns in the phase

$$\begin{aligned} J(f, \theta, S) &\approx \sum_{k=1}^K A_k e^{-j \frac{2\pi f}{c} (d_{ki} \cos \theta + y_{ki} \sin \theta)} \\ &= \sum_{k=1}^K A_k e^{-j (k_x d_{ki} + k_y y_{ki})} \end{aligned} \quad (3)$$

where $k_x = 2\pi f \cos \theta / c$ and $k_y = 2\pi f \sin \theta / c$. Note that (3) can be further approximated to completely decouple the frequency and aspect variable

$$J(f, \theta, S) = \sum_{k=1}^K A_k e^{-j \frac{2\pi f_c}{c} y_{ki} \theta} e^{-j \frac{2\pi f}{c} d_{ki}} \quad (4)$$

if we use $\sin \theta \approx \theta$ and replace the frequency variable in the first exponential by the center frequency f_c . Equation (4) then reduces to (3b) in [11], when only aspect variation is considered. For the 2-D extrapolation in this work, we choose to use the model in (3), since it is more accurate when the aspect range is large. Equation (3) is in the form of a sum-of-exponential model, with linear phase dependence with respect to both k_x and k_y . Consequently, the 2-D superresolution algorithm ESPRIT [17] can be applied to equally spaced k_x and k_y data samples. Next, we shall describe the implementation of the 2-D ESPRIT algorithm to estimate the unknown parameters in the model.

III. TWO-DIMENSIONAL ESPRIT ALGORITHM

In [16], a 2-D ESPRIT algorithm was developed for estimating the direction-of-arrival in 2-D antenna array problems. Here, we shall show that with some minor modifications, it can be applied to estimate the parameters A_k , d_k and y_k in (3). First, we assume that the parameters are to be estimated from known current values solved at $M \times N$ equally spaced samples in the $k_x - k_y$ plane, where M is the number of samples in k_x and N is the number of samples in k_y . These $M \times N$ samples are similar to the elements of a 2-D antenna array described in [16]. We define

$$p_k = e^{-j \Delta k_x d_k}, \quad q_k = e^{-j \Delta k_y y_k} \quad (5)$$

where Δk_x and Δk_y are the sampling intervals in k_x and k_y , respectively. If we shift the origin of the variables k_x and k_y to zero, we can rewrite (3) into a form similar to (9) of [16]

$$\begin{aligned} z_{il} &= \sum_{k=1}^K s_k p_k^{i-1} q_k^{l-1} + n_{il}, \\ i &= 1, 2, \dots, M, \quad l = 1, 2, \dots, N \end{aligned} \quad (6)$$

where z_{il} is the current at the i th k_x value and the l th k_y value. s_k is the modified amplitude coefficient for the k th mechanism to account for the origin shift. n_{il} is assumed to be white Gaussian noise, which in our case is used to model the numerical error in the current computation. Since ESPRIT postulates such a sum-of-exponential model with additive white noise, an averaging procedure has to be performed to smooth out the noise to obtain the correct estimate of the covariance matrix. In [16], the averaging is performed naturally in the time domain. However, for the problem at hand, the time dimension does not exist and has to be synthesized. This can be accomplished via a sub-array processing technique [21]. As shown in Fig. 2, a sub-array size is chosen to be half of the original array. Then shifting the sub-array one data sample at a time in either k_x or k_y will result in a new sub-array, which can be considered as the array at a new time index. If we assume M and N are even numbers, the total number of sub-arrays that can be generated

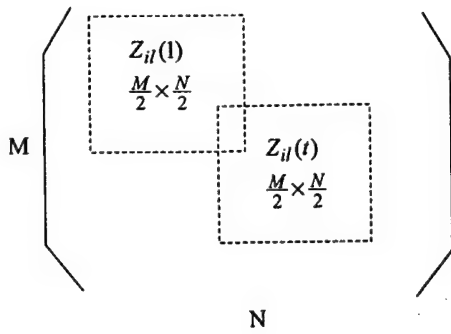


Fig. 2. Sub-array processing.

in this manner is $(M/2 + 1)(N/2 + 1)$. The signal vectors $z(t)$, $s(t)$, and $n(t)$ are defined as the reshaped column vectors of the t th sub-array as shown in (7)–(9), at the bottom of the page. In the above expressions, $I = M/2$ and $I = N/2$ are the maximum row and column indices of each sub-array. The array covariance matrix can thus be defined exactly like formula (15) in [16]. Following the procedures in [16], we estimate the parameters p_k and q_k . The time-of-arrival parameter d_k and the cross-range parameter y_k are obtained using

$$d_k = \frac{1}{\Delta k_x} \angle p_k, \quad y_k = \frac{1}{\Delta k_y} \angle q_k. \quad (10)$$

Finally, the amplitude coefficient A_k can be generated by solving (3) via a least squares procedure. Noted that the maximum order number K permitted by the algorithm is

$$K \leq \min \left[\left(\frac{M}{2} - 1 \right) \frac{N}{2}, \left(\frac{N}{2} - 1 \right) \frac{M}{2} \right] - 1. \quad (11)$$

For the scattering problems we have examined, K is usually chosen to be 3 or 4. The minimum number of frequency and angular samples can then be selected to satisfy the above criterion.

After the coefficients A_k , d_k , and y_k are estimated, we assume (3) also holds for other frequencies and aspects. Therefore, the induced current can be extrapolated to other k_x and k_y values of interest. An ISAR image is then generated using standard Fourier processing of the $k_x - k_y$ data. To summarize, the extrapolation procedure is carried out by first selecting a number of densely sampled points in a limited frequency-aspect range and solving the scattering problems at these points. Usually, the computed frequencies are chosen close to the low frequency end, and the aspect angles are centered about the central angle of interest. Second, the 2-D ESPRIT algorithm is applied to estimate the model parameters of the current at each point on the target surface. Third, the induced current is extrapolated to a wider k_x and k_y range based on the model coefficients generated from 2-D ESPRIT processing. Finally, the cur-

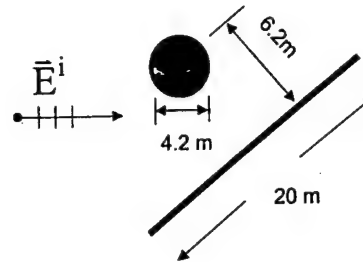


Fig. 3. Geometry of the cylinder-plate target.

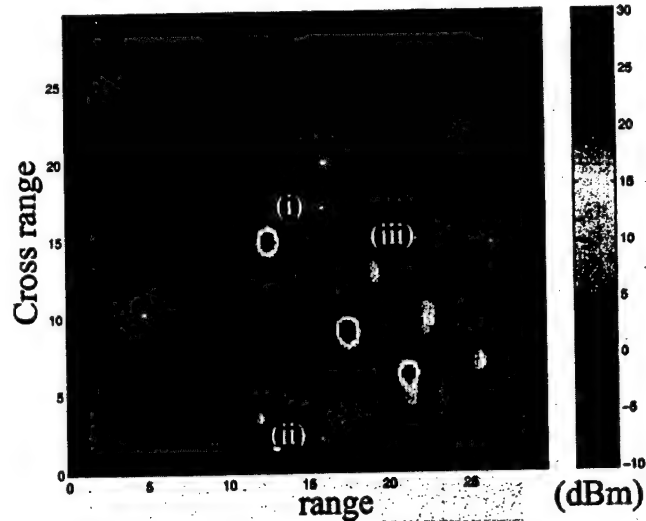


Fig. 4. Reference ISAR image generated using the brute-force MoM calculations at $71 \times 81 = 5751$ points.

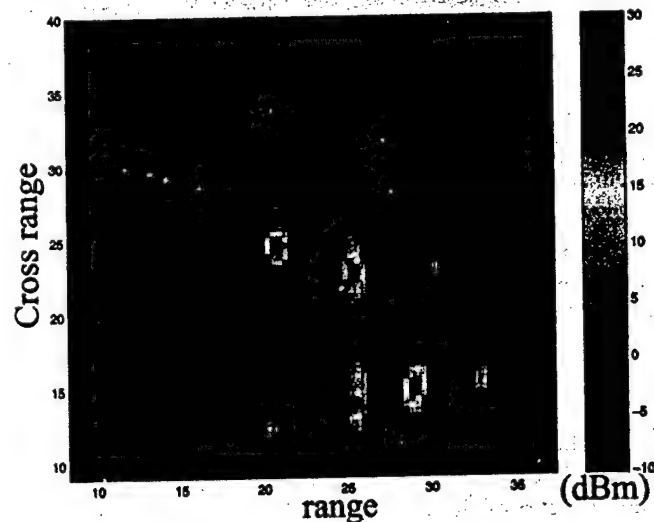


Fig. 5. ISAR image generated from 71 calculated frequency points and the bistatic approximation.

$$z(t) = [z_{11}(t) \quad \cdots \quad z_{1L}(t) \quad \cdots \quad z_{I1}(t) \quad \cdots \quad z_{IL}(t)]^T \quad (7)$$

$$s(t) = [s_1(t) \quad s_2(t) \quad \cdots \quad s_k(t)]^T \quad (8)$$

$$n(t) = [n_{11}(t) \quad \cdots \quad n_{1L}(t) \quad \cdots \quad n_{I1}(t) \quad \cdots \quad n_{IL}(t)]^T. \quad (9)$$

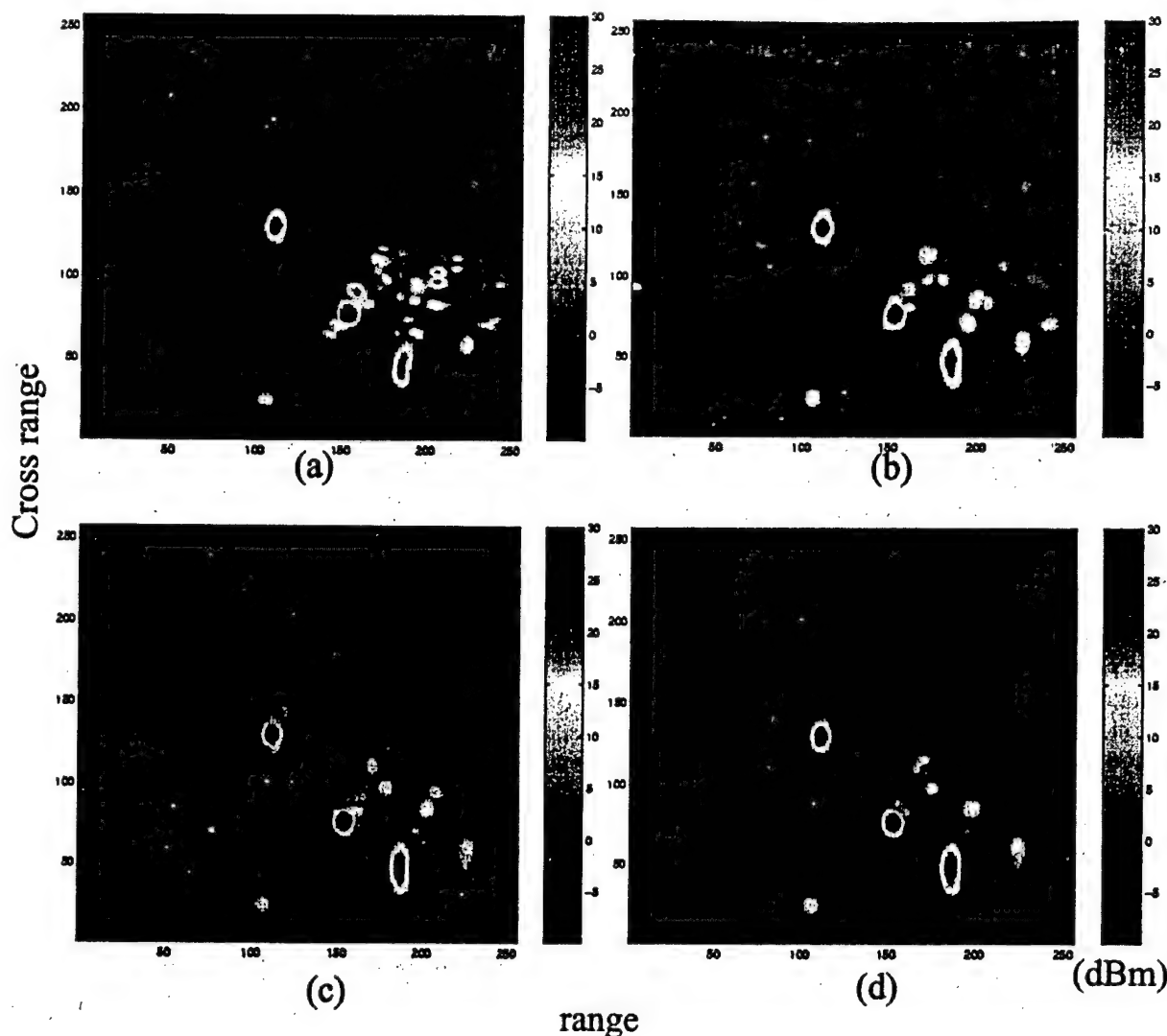


Fig. 6. ISAR images generated from the 2-D extrapolation algorithm using (a) 8×8 calculated points, (b) 9×9 calculated points, (c) 10×10 calculated points, and (d) 11×11 calculated points.

rent is integrated to generate the scattered far field as a function of frequency and aspect and the results are used to generate the desired ISAR image.

IV. NUMERICAL RESULTS

To validate the frequency-aspect extrapolation algorithm, we first consider a 2-D cylinder-plate structure, shown in Fig. 3. The diameter of the cylinder is 4.2 m, and the length of the plate is 20 m. The origin of the cylinder and the center of the plate are separated by 6.2 m. The frequency band of interest is from 0.3 GHz to 0.65 GHz, and the observation angle is from 25° to 65° . Fig. 4 shows the reference ISAR image generated from $71 \times 81 = 5751$ computed points in the frequency-aspect plane. The image has a dynamic range of 40 dB. In this structure, strong multiple scattering mechanisms between the cylinder and the plate dominate the backscattering. We can see in the image the features corresponding to the direct scattering from the cylinder, labeled (i), the front edge point of the plate (ii), and the shadow boundary cast on the plate by the cylinder

(iii). Additionally, there are other range-delayed features corresponding to the multiple scattering mechanisms. For comparison, we calculate the current at 71 frequency samples for one aspect angle and use the well-known bistatic approximation [17], [18] to extrapolate the RCS at other aspect angles. Fig. 5 plots the resulting ISAR image from the extrapolated frequency-aspect data using the bistatic approximation. In this image, only the direct scattering features [(i) and (ii)] are correctly predicted, while the higher-order scattering features are poorly predicted in either position or amplitude. This is because the bistatic approximation is based on physical optics, in which the current is assumed to be excited by only the direct incident wave.

We next construct the ISAR image using the 2-D frequency-aspect extrapolation algorithm. We choose 8×8 points at the low frequency end and about the central angle of the original 71×81 points. After the time-of-arrival and cross-range parameters are extracted by using 2-D ESPRIT, the induced currents and scattered far fields are extrapolated to the $k_x - k_y$ aperture of the original samples. In this manner, the ISAR

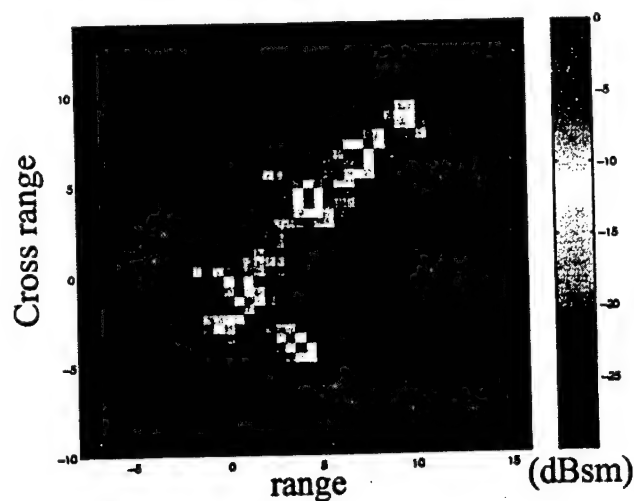


Fig. 7. ISAR image of the VFY-218 at 130° from nose-on, generated from the extrapolated result using 2-D ESPRIT with 36 FISC-computed points.

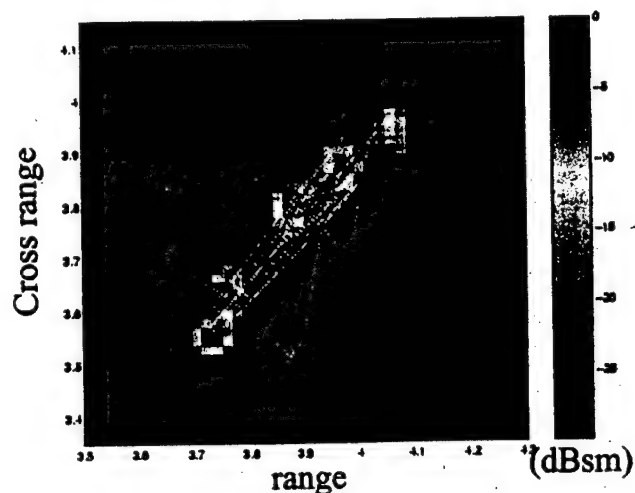


Fig. 8. ISAR image of the VFY-218 at 130° from nose-on generated from chamber measurement data [19].

image can be generated directly by a 2-D FFT of the $k_x - k_y$ data without the polar reformatting operation [2]. The resulting ISAR image is plotted in Fig. 6(a). As we can see, most of the features are predicted in the correct position. However, some of the weaker features are highly defocused. We repeat this process using 2-D ESPRIT extrapolation for 9×9 , 10×10 , and 11×11 input points. The resulting images are shown in Fig. 6(b)–(d), respectively. From this series of images, we see that the strong scattering features are quite stable throughout while the weaker features begin to converge as the number of input points is increased. We find that the correlation indices between the extrapolated images and the reference image are, respectively, 0.72, 0.80, 0.82 and 0.88. This shows a steady improvement as the number of input points is increased. For the case of 11×11 input points, nearly all of the features in the extrapolated image agree well with those in the reference image from the brute-force calculation. This corresponds to a 7:1 extrapolation ratio in each dimension.

Next, we use the 2-D extrapolation algorithm to simulate the ISAR image of the benchmark VFY-218 airplane. The simulation is carried out using the multilevel fast multipole code FISC [22] on a Pentium II 450 MHz PC. The total computation time would take about 200 days if a brute-force calculation is carried out over the required 41×41 frequency-aspect samples (to achieve 0.5 m resolution in range and cross range). Based on the 7:1 criterion found above, the actual computation is only carried out for $6 \times 6 = 36$ points from 267 MHz to 297 MHz in frequency and 127° to 132° in aspect. The total computation time is 40 h. Note that the time savings over the brute-force calculation is even greater than the $(41/6)^2$ ratio. This is because these 36 points are chosen at the low end of the frequency band and take far less time to compute than those at the high frequency end. The induced current and far fields are then extrapolated to a $k_x - k_y$ grid from 267 MHz to 533 MHz in frequency and from 110° to 140° in aspect. The resulting ISAR image of the airplane at 130° is shown in Fig. 7. Fig. 8 shows the ISAR image constructed from chamber measurement data at the same look angle [19]. Comparing these two images, we observe that nearly all of the key features in the measurement image are predicted in the simulated image from using FISC and the 2-D extrapolation algorithm. As expected, the image in Fig. 7 is much cleaner than the previously predicted image shown in [12, Fig. 11], which was simulated from the 1-D frequency extrapolation procedure in combination with the bistatic approximation. The improvement is due to the fact that the multiple scattering mechanisms are correctly incorporated in both dimensions in our new model. There still exist some low dynamic range noises in the predicted image, which can be improved with more computed points.

V. CONCLUSION

A 2-D frequency-aspect extrapolation algorithm has been developed to accelerate ISAR image simulation using fast multipole solvers. A 2-D multiple-arrival model consistent with high-frequency scattering physics was proposed to model the induced currents on the target. A 2-D ESPRIT algorithm was developed to estimate the model parameters from a limited number of computed data samples in frequency and aspect. The model was then extrapolated to other frequencies and aspects to arrive at broadband, wide-angle RCS data for ISAR image construction. This algorithm has been tested using a canonical cylinder-plate structure to evaluate its performance. It was found that a 7:1 extrapolation ratio in each dimension can be achieved. Furthermore, the input data samples can be chosen in the low frequency range for greater computational payoff. Lastly, the ISAR image of the benchmark VFY-218 airplane at UHF band has been predicted using the fast multipole solver FISC and the 2-D extrapolation algorithm. The resulting image compared favorably with that obtained from chamber measurement data. The computation time savings over the brute-force calculation was about two orders of magnitude.

ACKNOWLEDGMENT

The authors would like to thank Prof. W. Chew and Dr. J. Song for their help in using FISC.

REFERENCES

- [1] C. C. Chen and H. C. Andrews, "Target motion induced radar imaging," *IEEE Trans. Aerosp. Electron. Syst.*, vol. AES-16, pp. 2-14, Jan. 1980.
- [2] A. Ausherman, A. Kozma, J. L. Waker, H. M. Jones, and E. C. Poggio, "Developments in radar imaging," *IEEE Trans. Aerosp. Electron. Syst.*, vol. AES-20, pp. 363-400, Apr. 1984.
- [3] R. Coifman, V. Rokhlin, and S. Wandzura, "The fast multipole method for the wave equation: A pedestrian prescription," *IEEE Trans. Antennas Propagat. Mag.*, vol. 35, pp. 7-12, June 1993.
- [4] J. Song, C. C. Lu, and W. C. Chew, "Multilevel fast multipole algorithm for electromagnetic scattering by large complex objects," *IEEE Trans. Antennas Propagat. Mag.*, vol. 45, pp. 1488-1493, Oct. 1997.
- [5] G. J. Burke, E. K. Miller, S. Chakrabarti, and K. Demarest, "Using model-based parameter estimation to increase the efficiency of computing electromagnetic transfer functions," *IEEE Trans. Magn.*, vol. 25, pp. 2807-2809, July 1989.
- [6] K. Kottapalli, T. K. Sarkar, Y. Hua, E. K. Miller, and G. L. Burke, "Accurate computation of wide-band response of electromagnetic systems utilizing narrow-band information," *IEEE Trans. Microwave Theory Tech.*, vol. MTT-39, pp. 682-687, Apr. 1991.
- [7] Z. Altman and R. Mittra, "Combining an extrapolation technique with the method of moments for solving large scattering problems involving bodies of revolution," *IEEE Trans. Antennas Propagat.*, vol. 44, pp. 548-553, Apr. 1996.
- [8] E. K. Miller, "Model-based parameter estimation in electromagnetics: Part I. Background and theoretical development," *IEEE Antennas Propagat. Mag.*, vol. 40, pp. 42-52, Feb. 1998.
- [9] C. J. Reddy, M. D. Deshpande, C. R. Cockrell, and F. B. Beck, "Fast RCS computation over a frequency band using method of moments in conjunction with asymptotic waveform evaluation technique," *IEEE Trans. Antennas Propagat.*, vol. 46, pp. 1229-1233, Aug. 1998.
- [10] Y. Wang, H. Ling, J. Song, and W. C. Chew, "A frequency extrapolation algorithm for FISC," *IEEE Trans. Antennas Propagat.*, vol. 45, pp. 1891-1893, Dec. 1997.
- [11] Y. Wang and H. Ling, "A model-based angular extrapolation technique for iterative method-of-moment solvers," *Microwave Opt. Tech. Lett.*, vol. 20, pp. 229-233, Feb. 1999.
- [12] —, "Radar signature prediction using moment method codes via a frequency extrapolation technique," *IEEE Trans. Antennas Propagat.*, vol. 47, pp. 1008-1015, June 1999.
- [13] R. Roy, A. Paulraj, and T. Kailath, "ESPRIT—A subspace rotation approach to estimation of parameters of cisoids in noise," *IEEE Trans. Acoust., Speech, Signal Processing*, vol. ASSP-34, pp. 1340-1342, Oct. 1986.
- [14] R. Roy and T. Kailath, "ESPRIT—Estimation of signal parameters via rotation invariance techniques," *IEEE Trans. Acoust., Speech, Signal Processing*, vol. 37, pp. 984-995, July 1989.
- [15] J. Li and R. T. Compton Jr., "Angle and polarization estimation using ESPRIT with a polarization sensitive array," *IEEE Trans. Antennas Propagat.*, vol. 39, pp. 1376-1383, Sept. 1991.
- [16] —, "Two-dimensional angle and polarization estimation using the ESPRIT algorithm," *IEEE Trans. Antennas Propagat.*, vol. 40, pp. 550-555, May 1992.
- [17] R. Bhalla and H. Ling, "ISAR image formation using bistatic data computed from the shooting and bouncing ray technique," *J. Electromagn. Waves Applicat.*, vol. 7, pp. 1271-1287, Sept. 1993.
- [18] J. F. Shaffer, B. A. Cooper, K. W. Hom, R. C. Baucke, and N. A. Talcott Jr., "A review of bistatic k -space imaging for electromagnetic prediction codes for scattering and antennas," *IEEE Antennas Propagat. Mag.*, vol. 39, pp. 21-29, Oct. 1997.
- [19] H. T. G. Wang, M. L. Sanders, and A. Woo, "Radar Cross Section Measurement Data of the VFY 218 Configuration," Naval Air Warfare Center, China Lake, CA, Tech. Rep. NAWCWPNS TM-7621, Jan. 1994.
- [20] R. Bhalla, H. Ling, and H. Nussbaum, "Multi-aspect range profile extrapolation for the shooting and bouncing ray technique," *J. Electromagn. Waves Applicat.*, vol. 10, pp. 249-268, Feb. 1996.
- [21] T.-J. Shan, M. Wax, and T. Kailath, "On spatial smoothing for direction-of-arrival estimation of coherent signals," *IEEE Trans. Acoust., Speech, Signal Processing*, vol. ASSP-33, pp. 806-811, Aug. 1985.
- [22] User's Manual, Fast Illinois Solver Code (FISC), Center Comput. Electromagn., Univ. Illinois and DEMACO, Inc., Urbana, IL, Jan. 1997.

Yuanxun Wang (S'96-M'99) was born in 1973. He received the B.S. degree in electrical engineering from University of Science and Technology of China, Hefei, China, in 1993, the M.S. and Ph.D. degrees in electrical engineering from University of Texas, Austin, in 1996 and 1999.

From 1995 to 1999, he was with the Department of Electrical and Computer Engineering, University of Texas, Austin, as a Research Assistant. He is currently a Postdoctoral Research Engineer with the Department of Electrical Engineering, University of California, Los Angeles. His research interests include modeling and simulation of electromagnetic waves, microwave circuits, and digital signal processing, and integrating them for applications in radar and wireless communication.

Hao Ling (S'83-M'86-SM'92-F'99) was born in Taichung, Taiwan, on September 26, 1959. He received the B.S. degrees in electrical engineering and physics from the Massachusetts Institute of Technology, Cambridge, in 1982, and the M.S. and Ph.D. degrees in electrical engineering from the University of Illinois, Urbana, in 1983 and 1986, respectively.

Since 1986, he has been with the Faculty, University of Texas, Austin, and is currently a Professor with the Department of Electrical and Computer Engineering and holder of the Chevron Centennial Fellowship in Engineering. In 1982, he was with the IBM Thomas J. Watson Research Center, Yorktown Heights, NY, where he conducted low temperature experiments in the Josephson Department. In 1987, he was with the Summer Visiting Faculty Program, Lawrence Livermore National Laboratory, Livermore, CA. In 1990, he was an Air Force Summer Fellow with Rome Air Development Center, Hanscom Air Force Base, MA. His principal area of research is in computational electromagnetics. During the past decade, he has actively contributed to the development and validation of numerical and asymptotic methods for characterizing the radar cross section from complex targets. His recent research interests also include radar signal processing, fast algorithms for radar image simulation, and automatic target identification.

Dr. Ling was a recipient of the National Science Foundation Presidential Young Investigator Award in 1987, the NASA Certificate of Appreciation in 1991, and has received several teaching awards from the University of Texas, Austin.

and the MUSIC superresolution algorithm. The various scenarios studied include element spacing, noise level, antenna gain and delay, and platform effects. Our results show quantitatively the effect of mutual coupling on the direction-of-arrival estimates. The compensation of the coupling effect using the coupling matrix approach is also examined. This approach is found to be quite satisfactory in most cases, except when the array calibration data contain a high noise level or when strong platform effects are present. © 2000 John Wiley & Sons, Inc. Microwave Opt Technol Lett 26: 331–336, 2000.

Key words: array mutual coupling; direction-of-arrival estimates; compensation by coupling matrix

I. INTRODUCTION

It is well known that the mutual coupling between antenna elements in an array can strongly affect their radiation/receiving characteristics [1, 2]. For direction-finding applications, the direction-of-arrival estimates can be very sensitive to mutual coupling, and such effect needs to be properly accounted for [3]. An effective way to describe and compensate for the coupling effect in the array signal processing community is through the use of a coupling matrix [4]. It relates the active element patterns of the individual elements in the presence of the array environment to the idealized, free-standing element patterns. By measuring the actual array response at a few known incident angles during calibration, the coupling matrix can be estimated. Such an array calibration technique has been proven effective in many simulation and measurement results [5–7] involving simple antenna structures.

In this paper, we carry out a study to simulate the effect of mutual coupling for circular arrays. Our objectives are twofold. First, we set out to simulate the degradation effect due to mutual coupling in direction finding. Second, we set out to examine the validity of the coupling matrix model. This study is motivated by anomalies observed in measurement results from a smart antenna testbed for wireless communications [8]. Our approach is to use the full-wave electromagnetic solver NEC [9] to carry out the simulation. The superresolution algorithm MUSIC is applied to perform the direction-of-arrival (DOA) estimate. The various scenarios studied include element spacing, noise level, antenna gain and delay, and platform effects. Our results show quantitatively the effect of mutual coupling on DOA estimates. In addition, it is shown that the coupling matrix model is quite adequate under most scenarios examined by us.

II. FORMULATIONS FOR DIRECTION FINDING

The mutual coupling effect in an antenna array is commonly described in array signal processing by the following model [4]:

$$\mathbf{A}_{\text{true}} = \mathbf{C}\mathbf{A}_{\text{theo}} \quad (1)$$

where \mathbf{A}_{true} is the actual array response matrix, \mathbf{A}_{theo} is the ideal array response matrix in the absence of mutual coupling, and \mathbf{C} is an angular-independent coupling matrix. Each row of \mathbf{A}_{true} is the relative received signal strength of a particular antenna element as a function of the incident angle of an incoming plane wave. In the context of standard antenna terminology, this is known as the active element pattern of the array element. In the absence of mutual coupling, the receiving pattern for a single antenna element is independent of the others, and is only a function of the

SIMULATION OF MUTUAL COUPLING EFFECT IN CIRCULAR ARRAYS FOR DIRECTION-FINDING APPLICATIONS

Tao Su,¹ Kapil Dandekar,¹ and Hao Ling¹

¹ Department of Electrical and Computer Engineering
University of Texas at Austin
Austin, Texas 78712-1084

Received 20 March 2000

ABSTRACT: The effect of mutual coupling on direction finding in circular arrays is simulated using rigorous electromagnetic computation

Contract grant sponsor: Office of Naval Research

Contract grant number: N00014-98-1-0178

Contract grant sponsor: Texas Higher Education Coordinating Board
under the Texas Advanced Technology Program

incident angle and the position of the element. We consider the case where the sources as well as the array are located in the (x, y) -plane. Then the ideal element pattern can be written as

$$a_{\text{theo},m}(\phi) = e^{jk(x_m \cos \phi + y_m \sin \phi)}, \quad m = 1, \dots, M \quad (2)$$

where M is the total number of elements, (x_m, y_m) are the coordinates of the m th element, and ϕ is the incident angle. The ideal array response is then

$$\mathbf{A}_{\text{theo}} = [a_{\text{theo},1}(\phi) a_{\text{theo},2}(\phi) \cdots a_{\text{theo},M}(\phi)]^T. \quad (3)$$

Since \mathbf{A}_{theo} is known based on the array geometry, if \mathbf{A}_{true} is given, then \mathbf{C} can be determined by using the pseudoinverse concept as

$$\mathbf{C} = \mathbf{A}_{\text{true}} \mathbf{A}_{\text{theo}}^H (\mathbf{A}_{\text{theo}} \mathbf{A}_{\text{theo}}^H)^{-1}. \quad (4)$$

For simple antennas whose current distributions have the same shape but different amplitudes, \mathbf{C} can be found from \mathbf{A}_{true} at only a few observation angles. Once \mathbf{C} is known, \mathbf{A}_{true} can be interpolated to very fine angular granularity based on the model. Therefore, the coupling matrix concept is a very efficient description of the mutual coupling effect. We will use numerical simulation data to examine the validity of this model for direction finding.

To extract the directions of arrival from the received signals at the array, we use the superresolution algorithm MUSIC. If the signals come from N unknown directions, the received signal at the m th antenna can be written as

$$x_m(t) = \sum_{n=1}^N a_m(\phi_n) s_n(t) + z_m(t) \quad (5)$$

where $s_n(t)$ is the amplitude of the n th signal, $a_m(\phi_n)$ is the active element pattern of the m th element at the n th incident angle, and $z_m(t)$ represents the noise. Expressed in matrix form, (5) becomes

$$\mathbf{X} = \mathbf{A} \mathbf{S} + \mathbf{Z} \quad (6)$$

where \mathbf{A} is the array response. In principle, the actual array response \mathbf{A}_{true} should be used in (6) to properly model the received signal. However, if the ideal array response \mathbf{A}_{theo} is used instead, we, in effect, ignore the mutual coupling between the elements, and generate what we will call the uncompensated result. In the next section, we evaluate the performance difference between the compensated and uncompensated results to assess the significance of mutual coupling.

If the noise is assumed to be white Gaussian noise, the correlation matrix of \mathbf{X} can be separated into the signal part and the noise part:

$$\mathbf{R} = \mathbf{X} \mathbf{X}^H = \mathbf{A} \mathbf{S} \mathbf{S}^H \mathbf{A}^H + \sigma_n^2 \mathbf{I} \quad (7)$$

where σ_n^2 is the noise power. If the signals are uncorrelated, the N largest eigenvalues of \mathbf{R} correspond to the signal subspace, and the rest correspond to the noise subspace. Let \mathbf{V}_n denote the eigenvectors corresponding to the noise space.

The power spectrum defined in the MUSIC algorithm is then

$$P(\phi) = \frac{1}{\sum_{m=1}^M a_m^H(\phi) \mathbf{V}_n \mathbf{V}_n^H a_m(\phi)}. \quad (8)$$

The DOAs are determined by observing the peaks in the power spectrum as a function of incident angle.

III. SIMULATION RESULTS

A seven-element circular array shown in Figure 1 is used in the simulation. The radius of the circle is 0.5 wavelength. The array elements are half-wave dipoles. Each dipole is divided into 21 segments in the NEC simulation, with the load impedances equal to 73Ω at the center segments. First, the actual array response is computed densely from 0 to 360° in steps of 0.2° . This will be used to generate the reference DOA results. Next, we use the actual array response at eight incident angles equally spaced around a circle to determine the coupling matrix \mathbf{C} using (4). An interpolated version of the array response is then obtained using (1). The DOA results generated in this manner will be termed the "compensated-by-coupling matrix" (CC) results.

To illustrate the mutual coupling effect in direction finding, we first consider one incoming signal from the angle 0° , 45° , or 90° . The signal-to-noise ratio (SNR) is set to be 30 dB. The normalized MUSIC power spectra are plotted in Figure 2(a). The dashed curves are the uncompensated results computed using the ideal array response \mathbf{A}_{theo} . The solid curves are the reference results generated using the actual array response \mathbf{A}_{true} . The mutual coupling effect can be easily observed from the uncompensated curves where the peaks in the power spectra are significantly broadened. It is interesting to note that, due to the symmetry of the circular array structure, the direction of arrival is still estimated correctly by the uncompensated curve for a single incoming signal. However, as will be shown shortly, this will not be so when there is more than one incoming signal. We also test the validity of the coupling matrix model by generating the power spectra using the interpolated \mathbf{A}_{true} . The compensated-by-coupling matrix (CC) results nearly overlay the reference results, and are not shown. Only eight samples of the actual array response are used to generate the 7×7 coupling matrix. When compared to the densely computed actual array response of size 1800×7 , the coupling matrix model in (1) is indeed a very efficient representation of the mutual coupling effect. Figure 2(b) illustrates the power spectra when two

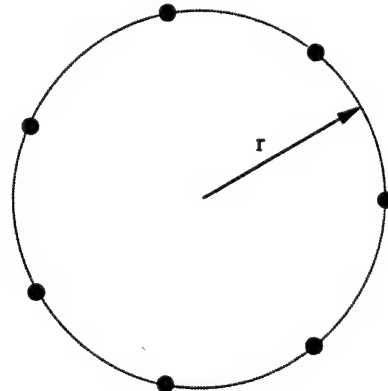
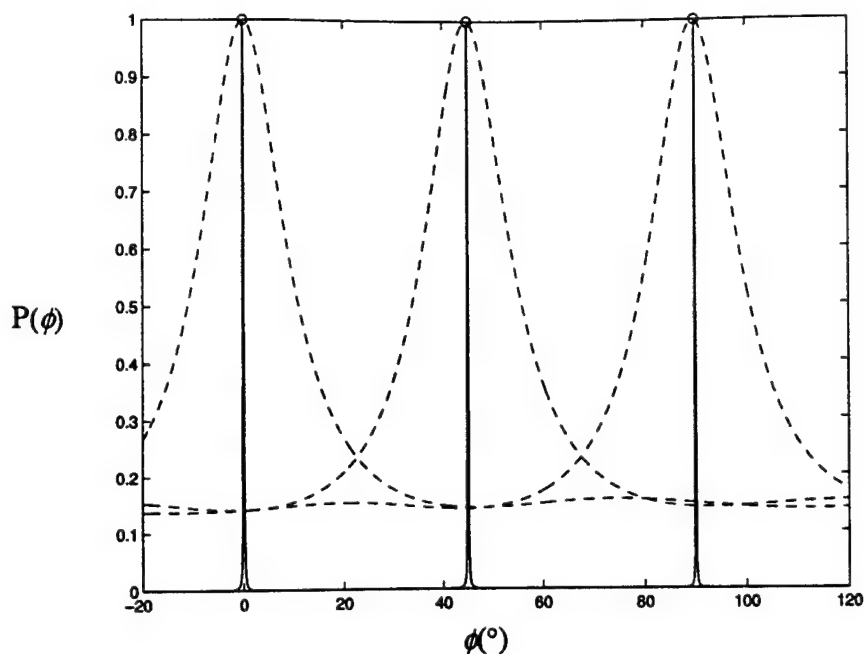
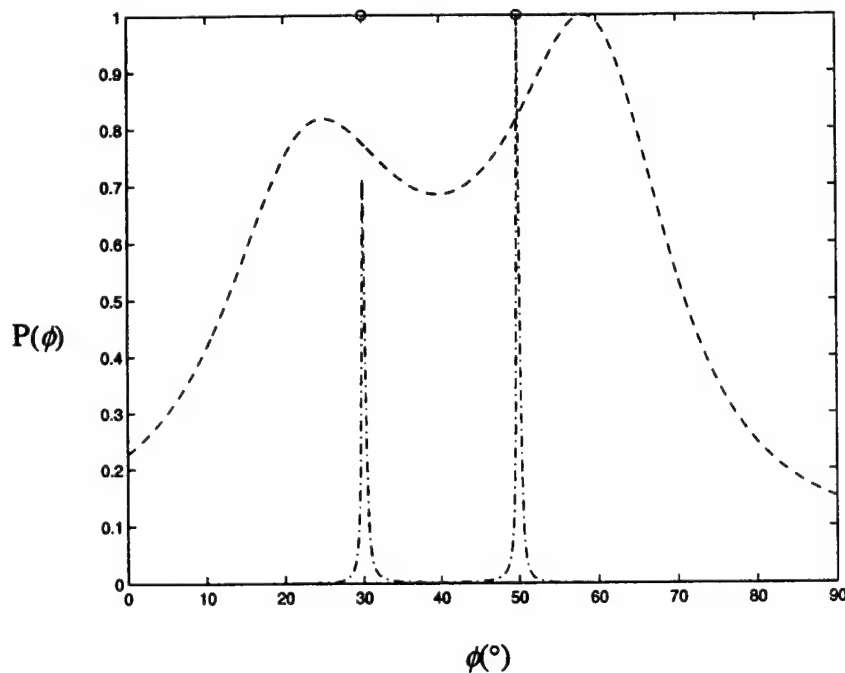


Figure 1 Circular array layout



(a)



(b)

Figure 2 MUSIC power spectrum before and after compensation of the mutual coupling effect. ---Uncompensated, ----compensated by coupling matrix (CC), —reference. (a) Power spectrum with one incoming signal. (b) Power spectrum with two incoming signals

uncorrelated signals exist at 30 and 50°. The dashed curve is the uncompensated result, and the dash-dot curve is the CC result. When there is more than one signal, the coupling effect becomes more severe. The peaks of the uncompensated result no longer indicate the correct directions of arrival. However, the CC result still has sharp peaks at the correct DOA.

Next, we examine the mutual coupling effect when the spacing between array elements is reduced. We let the radius

of the circular array be 0.25 wavelength. The power spectra when there are two incoming signals at 30 and 50° are plotted in Figure 3. Compared with the previous example, we see that the mutual coupling effect is much stronger, as expected. The uncompensated curve, which ignores the mutual coupling, shows only one broad peak. The CC curve, on the other hand, still correctly resolves the two DOAs.

In the third example, we examine array calibration in a very noisy environment. We reduce the signal-to-noise ratio

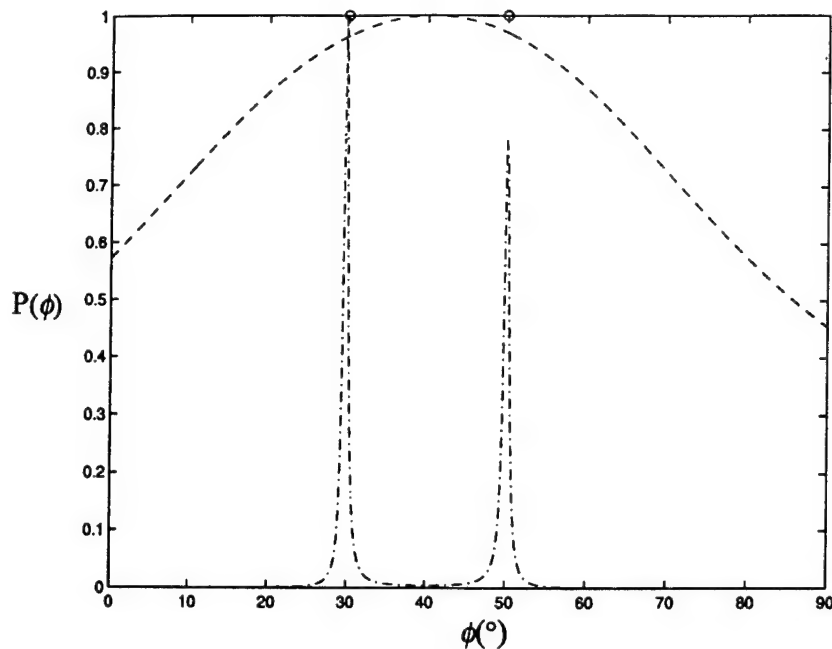


Figure 3 MUSIC power spectrum before and after compensation when the array spacing is halved. ---Uncompensated, ----CC

to 0 dB. Data used for both A_{true} and C contain white noise. Two signals are imposed on the array, and the MUSIC power spectra are plotted in Figure 4. The dashed curve is the uncompensated result, the dash-dot curve is the CC result, and the solid curve is the reference result. Since A_{true} is collected in the presence of strong noise, the reference curve shows the degradation of the MUSIC algorithm due to noise. The CC curve includes the additional degradation from estimating the coupling matrix using noisy data. As we can see, when the coupling matrix is estimated in the noisy environ-

ment, the direction-finding result is not as satisfactory. The uncompensated result is again the poorest.

In the fourth example, we consider the antenna gain and delay difference between the array elements, in addition to the mutual coupling. We simulate this condition in NEC by using different load impedances for different antenna elements. The real and imaginary parts of the load impedances are randomly selected between -400 and 400Ω . The power spectra for one signal coming at 0 , 45 , or 90° are plotted in Figure 5. Some of the uncompensated results show false

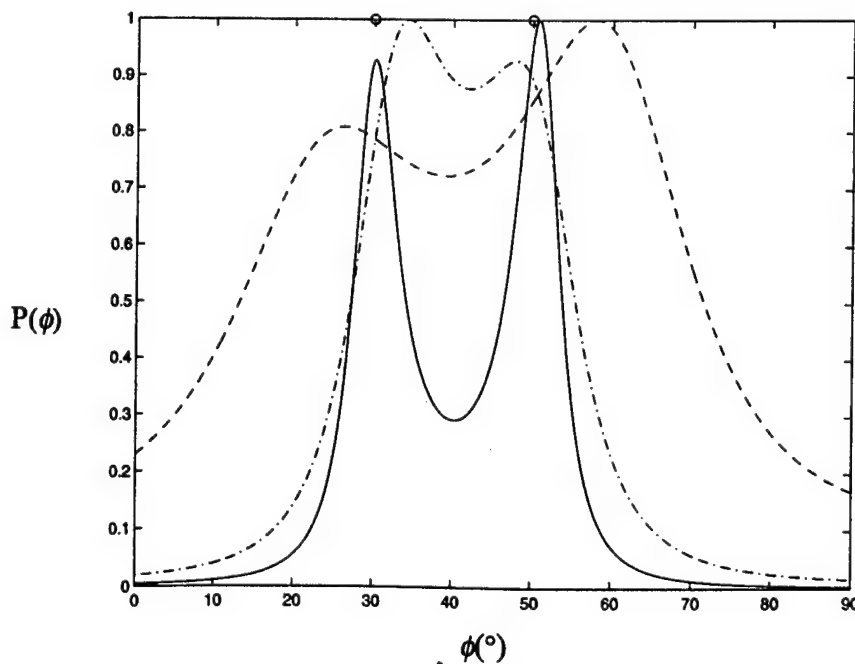


Figure 4 MUSIC power spectrum before and after compensation when the SNR is lowered to 0 dB. ---Uncompensated, ----CC, —reference

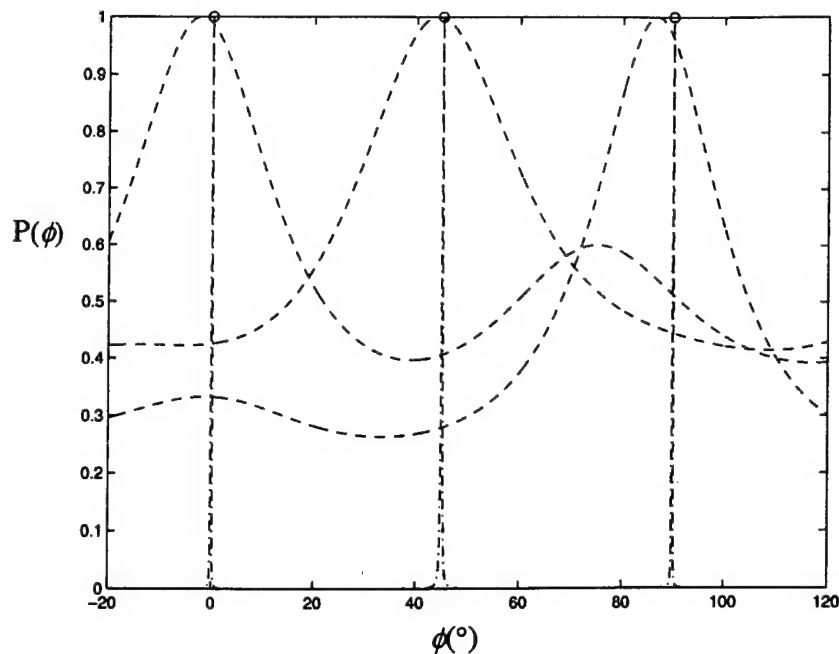


Figure 5 MUSIC power spectrum before and after compensation when unknown antenna gains and delays are considered. ---Uncompensated, ----CC

peaks in the spectrum. The peaks corresponding to the correct DOAs also deviate from their correct locations. This implies that the error in antenna gain and delay is as significant as the mutual coupling effect. On the other hand, the sharp peaks from the CC results indicate that the gain and delay errors can still be correctly accounted for by the coupling matrix model. This is not surprising since the condition for (1) to be valid is still satisfied.

Finally, we consider an example where a platform structure is placed close to the array. We put a center conducting

post in the middle of the array to simulate a real antenna array layout. The post is 0.2 wavelength in radius, and is approximated by 36 vertical wires in NEC. We again consider the case of two incoming signals. The MUSIC power spectra are plotted in Figure 6, where the dashed curve is the uncompensated result, the dash-dot curve is the CC result, and the solid curve is the reference result. It can be observed that, although the CC result is much better than the uncompensated one, it cannot achieve the same resolution as the reference curve. This is because the actual array response is

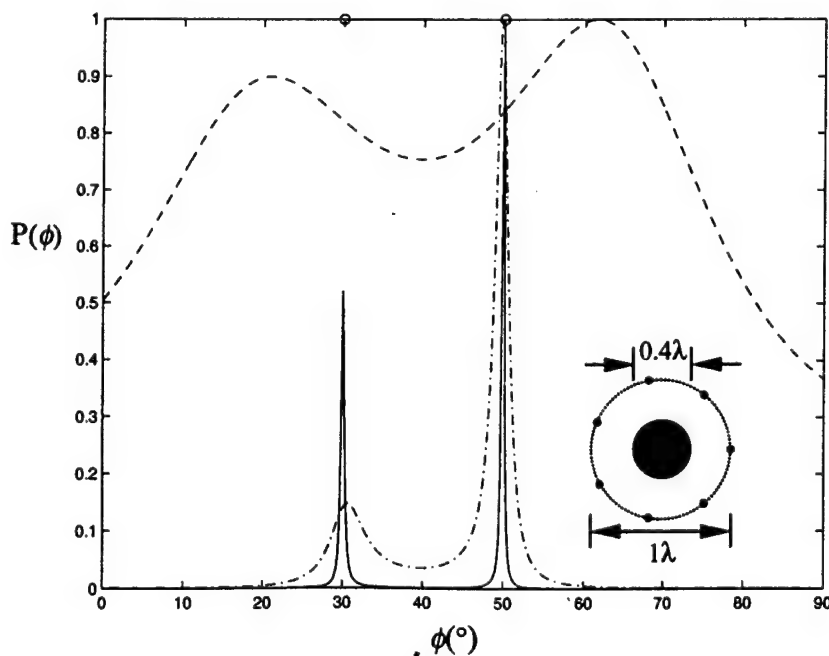


Figure 6 MUSIC power spectrum before and after compensation when the platform effect is considered. ---Uncompensated, ----CC, —reference

not correctly modeled by (1), as the ideal element patterns used in (1) do not include the effect of the platform. Thus, the coupling matrix is no longer angular independent. However, if the two signals are not too closely spaced in angle, the DOA estimates are still satisfactory.

IV. CONCLUSIONS

In this paper, the effect of mutual coupling on direction-of-arrival estimates in a circular array is simulated using rigorous electromagnetic computation. The compensation of the coupling effect using the coupling matrix approach is also examined. Numerical results show that the mutual coupling effect can lead to significant errors in direction finding when not properly accounted for. The compensation of the mutual coupling effect using the coupling matrix approach is found to be quite satisfactory in most cases. The coupling matrix model provides a very sparse description of the array response. It can also take into account additional antenna gain and delay errors. However, the performance of this approach degrades in cases when the array calibration data contain a high noise level or when strong platform effects are present.

REFERENCES

1. D.F. Kelley and W.L. Stutzman, Array antenna pattern modeling methods that include mutual coupling effects, *IEEE Trans Antennas Propagat* 41 (1993), 1625–1632.
2. I.J. Gupta and A.A. Ksienski, Effect of mutual coupling on the performance of adaptive arrays, *IEEE Trans Antennas Propagat* AP-31 (1983), 785–791.
3. T. Svantesson, Modeling and estimation of mutual coupling in a uniform linear array of dipoles, *IEEE Int Conf Acoust, Speech, Signal Processing*, Phoenix, AZ, 1999, pp. 2961–2964.
4. B. Friedlander and A.J. Weiss, Direction finding in the presence of mutual coupling, *IEEE Trans Antennas Propagat* 39 (1991), 273–284.
5. C.M.S. See, A method for array calibration in parametric sensor array processing, *IEEE Singapore Int Conf Commun Sys*, Singapore, 1994, pp. 915–919.
6. J. Pierre and M. Kaveh, Experimental performance of calibration and direction-finding algorithms, *IEEE Int Conf Acoust, Speech, Signal Processing*, Toronto, Ont., Canada, 1991, pp. 1365–1368.
7. A.N. Lemma, E.F. Deprettere, and A.J. Veen, Experimental analysis of antenna coupling for high-resolution DOA estimation algorithms, *IEEE Workshop Signal Processing Advances in Wireless Commun*, Annapolis, MD, May 1999, pp. 362–365.
8. S.S. Jeng, G.T. Okamoto, G. Xu, H.P. Lin, and W.J. Vogel, Experimental evaluation of smart antenna system performance for wireless communications, *IEEE Trans Antennas Propagat* 46 (1998), 749–757.
9. NEC-2 manual, Lawrence Livermore National Lab, 1996.

FREQUENCY INTERPOLATION OF ELECTROMAGNETIC SCATTERING DATA USING A HYBRID MODEL

Bin Jiang,¹ Tao Su,¹ and Hao Ling¹

¹Department of Electrical and Computer Engineering
University of Texas at Austin
Austin, Texas 78712-1084

Received 19 June 2000

ABSTRACT: A frequency-interpolation algorithm for electromagnetic scattering data from large, complex targets is proposed. It is based on the hybridization of the existing multiple-arrival model and the rational-function model. At each point on the target, the induced current is parameterized using both models separately. The model that best matches the scattering physics at that location is chosen based on the resulting interpolation error. As a result, those regions on the target that are best described by ray-optical phenomena are interpolated by the multiple-arrival model, while those regions that exhibit resonance phenomena are interpolated by the rational-function model. Numerical results show that the hybrid scheme is superior to either the multiple-arrival model or the rational-function model for a target containing complex features. © 2000 John Wiley & Sons, Inc. *Microwave Opt Technol Lett* 27: 307–312, 2000.

Key words: frequency interpolation; method of moments; multiple-arrival model; rational-function model

1. INTRODUCTION

The electromagnetic scattering data from a complex target are often of interest over a broad band of frequencies. To simulate multiple-frequency data using a frequency-domain computational electromagnetics solver is an exhaustive procedure as the computation must be carried out one frequency at a time. The problem is further compounded by the fact that the required sampling density in frequency is approximately proportional to the size of the target. For large complex targets, it is therefore desirable to develop algorithms to generate a dense set of frequency data from a very sparse set of computed frequency points to save computation time. This frequency-interpolation problem was recently addressed in [1] using a model-based approach based on a high-frequency model. The current at each point on the target is modeled by a collection of time-of-arrival mecha-

Contract grant sponsor: Office of Naval Research

Contract grant number: N00014-98-1-0178

Contract grant sponsor: Air Force MURI Center for Computational Electromagnetics

Contract grant number: AFOSR F49620-96-1-0025

nisms arising from multiple scattering (see Fig. 1). The time of arrival and the strength of the different mechanisms are extracted from the available frequency data using the adaptive feature extraction (AFE) algorithm [2]. It was shown that good interpolation results can be obtained even for very sparsely sampled data in frequency.

In this paper, we set out to improve the accuracy of the above interpolation algorithm for complex targets by incorporating additional scattering physics in the model. The multiple-arrival model is well matched to the ray-optical description of fields and currents. However, more general targets contain not only large-scale features, but also small resonant features. Although these resonant contributions are, in general, weaker than the returns from large-scale features, they do impact the accuracy of the interpolation if not properly taken into account. The multiple-arrival model, however, is not a good model for resonance phenomena as many time-of-arrival terms are required to adequately describe resonance. A much better model is the rational-function model, which has been widely used in frequency-interpolation problems in the resonant region [3–8]. It can be shown that the multiple-arrival model and the rational-function model are, in fact, complementary models. The former is a sum of exponentials in frequency, while the latter is a sum of exponentials in time. To take advantage of the strength of each model, we propose here a hybrid interpolation scheme that uses the most appropriate model over different portions of the target. At each point on the target, we parameterize the induced current using both models separately. Next, by using the resulting parameterization error as the selection criterion, we choose the model that best matches the scattering physics at that location. The total scattered field is then constructed from the interpolated currents. Section 2 describes our formulation. The two models and the methods for parameterization are first summarized. They are followed by the hybrid procedure. Our test results in Section 3 show that the hybrid scheme is superior to either the multiple-arrival or the rational-function model alone for a target containing complex features.

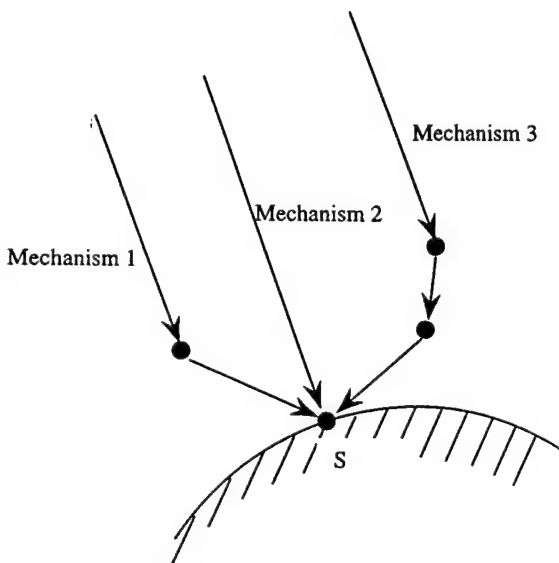


Figure 1 Multiple-arrival model for the induced current

2. FORMULATION

2.1. Multiple-Arrival Model and AFE Interpolation Algorithm.

In the multiple-arrival model, we assume that the induced current at a point on the target can be written as a summation of multiple-scattering mechanisms from M different incident paths (see Fig. 1):

$$J(f) = \sum_{i=1}^M A_i \exp(-j2\pi f t_i) \frac{f^{\alpha_i}}{\sqrt{\sum_p |f_p^{\alpha_i}|^2}} \quad (1)$$

where f is the frequency, t_i is the time of arrival for mechanism i , and A_i is the corresponding excitation amplitude. This time-of-arrival model is based on high-frequency ray-optical phenomena, and has been well utilized in the electromagnetics community [9–11]. The last term in this model incorporates an additional frequency-dependent factor α_i , which was not used in [1]. It is consistent with high-frequency diffraction theory [10, 12, 13], and improves the accuracy of the model. Lastly, the extra factor in the denominator is included for normalization.

To determine the unknowns in the model based on the available frequency samples of the current, we use the adaptive feature extraction algorithm [2]. The parameterization is carried out in an iterative manner starting from the strongest mechanism. The sampled frequency response is first projected onto the complex conjugate of the model bases for all possible values of t_j and α_j . We then select the basis that gives the maximum projection value. This is described as follows:

$$A_i = \max \left\langle J_i(f), \exp(j2\pi f t_j) \frac{f^{\alpha_j}}{\sqrt{\sum_p |f_p^{\alpha_j}|^2}} \right\rangle \quad (2)$$

where the inner product in the above formula is defined as

$$\langle a(f), b(f) \rangle = \frac{1}{N} \sum_{p=1}^N a(f_p) b(f_p). \quad (3)$$

After the strongest feature with (A_i, t_i, α_i) is captured, that feature is subtracted from the signal to generate a remainder signal:

$$J_{i+1}(f) = J_i(f) - A_i \exp(-j2\pi f t_i) \frac{f^{\alpha_i}}{\sqrt{\sum_p |f_p^{\alpha_i}|^2}}. \quad (4)$$

The above procedure is iterated to extract the parameters for each scattering mechanism until the remaining signal reaches a sufficiently small level.

A key concept in AFE is to use random frequency sampling during the original data generation to avoid the ambiguity in selecting the strongest feature [1]. Therefore, the frequencies at which the electromagnetic computations are carried out should not be evenly spaced. In addition, since the strongest feature contains interference from the weaker features, the amplitude of each feature is not extracted perfectly using AFE. We have found that, by performing a linear least square optimization for the amplitude parameter

after the whole iteration procedure, the AFE performance is significantly improved.

2.2. Rational Function Model and Cauchy Method. The multiple-arrival model and AFE can be used to effectively carry out frequency interpolation for targets containing ray-optical phenomena. For target resonance, however, it is more appropriate to use a rational-function model to describe the frequency resonance mechanism. The rational-function model is introduced below, and the Cauchy method for determining the model parameters is summarized. The reader is referred to [5, 6] for a detailed description of the method.

Consider the frequency response of a system $H(s)$. From circuit theory, it is customary to describe $H(s)$ by the ratio of two polynomials $A(s)$ and $B(s)$ as follows:

$$H(s) = \frac{A(s)}{B(s)} = \frac{\sum_{k=0}^P a_k s^k}{\sum_{k=0}^Q b_k s^k}. \quad (5)$$

For $Q > P$, this is a pole model, and thus can be used to describe the strong resonance behavior of the current in the frequency domain by the proper choice of the pole locations.

Given the value of $H(s)$ and its frequency derivatives at some frequency points s_n , the Cauchy problem is stated as

$$\text{given } H^j(s_n), \quad \text{for } j = 0, \dots, J, n = 1, \dots, N$$

find P and Q , $\{a_k, k = 0, \dots, P\}$ and $\{b_k, k = 0, \dots, Q\}$.

where $H^j(s_n)$ represents the j th frequency derivative of H at s_n . Equation (5) can be rearranged into a matrix form as follows:

$$[A \quad -B] \begin{bmatrix} a \\ b \end{bmatrix} = 0 \quad (6)$$

where

$$A(n, k) = \frac{k!}{(k-j)!} s_n^{(k-j)} u(k-j) \quad (7)$$

and

$$B(n, k) = \sum_{i=0}^j C_{j,i} H^{(j-i)}(s_n) \frac{k!}{(k-i)!} s_n^{(k-i)} u(k-i). \quad (8)$$

Here, $u(k)$ is 0 for $k < 0$ and 1 otherwise, $C_{j,i} = (j!/(i!(j-i)!))$, $a = [a_1 a_2 a_3 \dots a_P]^T$, and $b = [b_1 b_2 b_3 \dots b_Q]^T$. To solve for the polynomial coefficients a_k and b_k from the matrix equation (5), singular value decomposition is utilized. The model orders P and Q can be estimated from the number of significant singular values. The singular vector corresponding to the smallest singular value is chosen to be the solution of (6).

Several comments are in order. First, the quantity to be interpolated in our problem is the frequency response of the current. Thus, $H(s) = J(f)$ where $s = j2\pi f$. Second, we only use frequency points, and not frequency derivatives as the input to the Cauchy algorithm. This is for ease of hybridization with the AFE algorithm. Furthermore, for an iterative solution to electromagnetic integral equations, the computational complexity to generate the frequency derivative of the

current is as high as that for a new frequency point. Third, instead of estimating the orders of the polynomial functions, we choose $Q = P + 1$ and $P + Q + 1 = N$ in our implementation. We find that our results are not very sensitive to the order estimation. Lastly, we note that the frequency points need not be equally spaced in carrying out the Cauchy method. This gives us the possibility to use the same set of sampled data for both the Cauchy and AFE interpolation schemes.

2.3. Hybrid AFE-Cauchy Algorithm. We are now armed with two interpolation algorithms. The AFE algorithm works well for low-order multiple-scattering mechanisms that resemble high-frequency ray optics, while the Cauchy algorithm is better suited for describing resonance phenomena. The essential idea of the hybrid algorithm is to choose the most appropriate model for the current at each point on the target. Our approach is as follows. At each point on the target, we first parameterize the induced current using both the AFE and Cauchy algorithms separately, with the same set of sampled frequency responses. The model that best matches the scattering physics at that location is then chosen. In the actual implementation, the selection is made by comparing the interpolated data from the two models against the brute-force computation at several new frequency points. The model with the smaller interpolation error is chosen for that location. As a result, the surface of the target can be divided into two regions—the AFE region and the Cauchy region. Over the AFE region, the currents exhibit high-frequency scattering phenomenology. Over the Cauchy region, the currents exhibit strong resonance. Once the parameterization and model determination have been made, the interpolated currents on the target over the frequency band of interest can be generated. Therefore, the scattered far field can be obtained by integrating the induced current over the target at any frequency of interest.

It has been pointed out that the AFE algorithm requires as its input the currents computed at a set of nonuniformly sampled frequencies. In fact, the more random the sampling, the better the performance of the AFE. It has also been noted that, in the Cauchy algorithm, the frequency points need not be uniformly sampled. However, equally spaced frequency points increase the chance for the Cauchy method to accurately capture the poles in the frequency domain. Consequently, we find contradictory requirements for the optimal sampling in frequency between the AFE and Cauchy algorithms. AFE requires random sampling, while Cauchy prefers uniform sampling. Here, we choose a compromise solution, i.e., semirandom sampling. To choose the N frequency points needed for interpolation, we first equally divide the whole frequency band into N uniformly spaced subbands. The sampling point within each subband is chosen randomly based on a uniform probability distribution. The sampled data can then be used in both algorithms.

3. NUMERICAL EXAMPLE

We consider a 2-D conducting target as shown in Figure 2. Although this plate-like target looks simple, its scattering characteristics involve a variety of scattering mechanisms [14]. An E -polarized plane wave is incident at an angle of 60° from the right. The reference backscattering data versus frequency are first computed using the method of moments (MoM) at 100 frequency points from 0.1 to 10 GHz in 0.1 GHz steps. The frequency response of the backscattered field is plotted

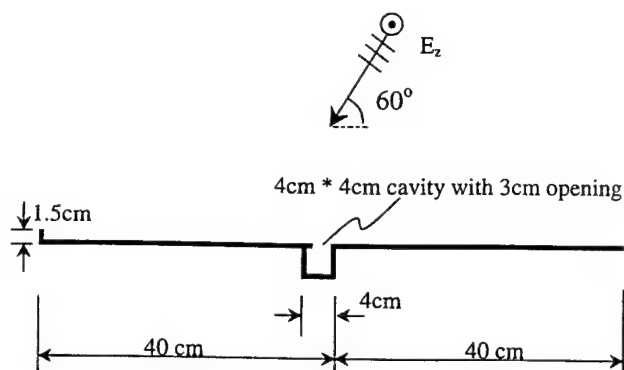


Figure 2 Geometry of the conducting plate with cavity and fin

as the solid line in Figure 3. By inverse Fourier transforming the frequency data, the range profile of the target can be generated. It is plotted in Figure 4 as the solid curve (a Hamming window has been applied to reduce range side-lobes). We recognize four large peaks in the range profile, which correspond, respectively, to the scattering from the right edge of the plate, the aperture of the partially open cavity, the interior of the cavity, and the small fin at the left edge.

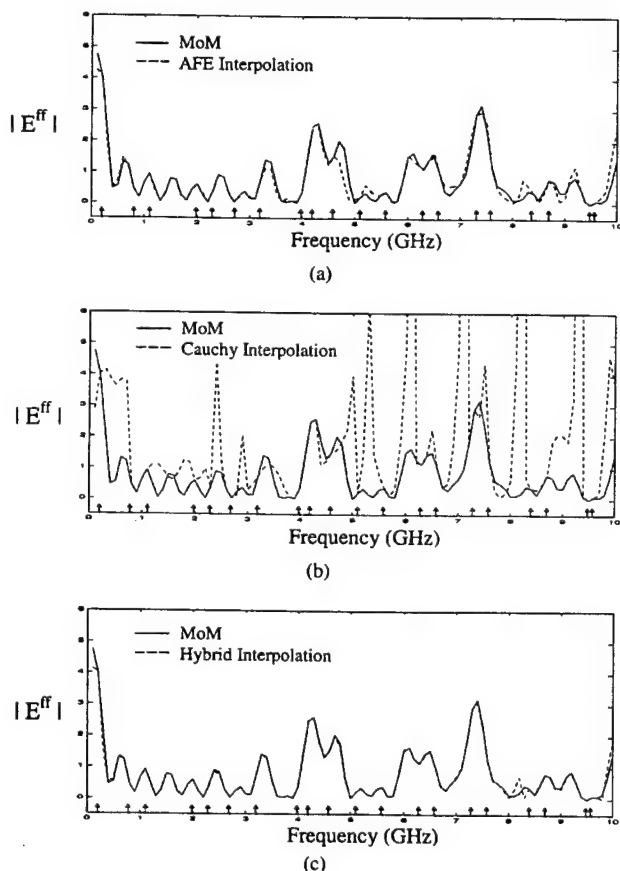


Figure 3 (a) Comparison of the backscattered field versus frequency between the brute-force MoM and the AFE interpolation results based on 20 points. (b) Comparison of the backscattered field versus frequency between the brute-force MoM and the Cauchy interpolation results based on 20 points. (c) Comparison of the backscattered field versus frequency between the brute-force MoM and the hybrid interpolation results based on 20 points

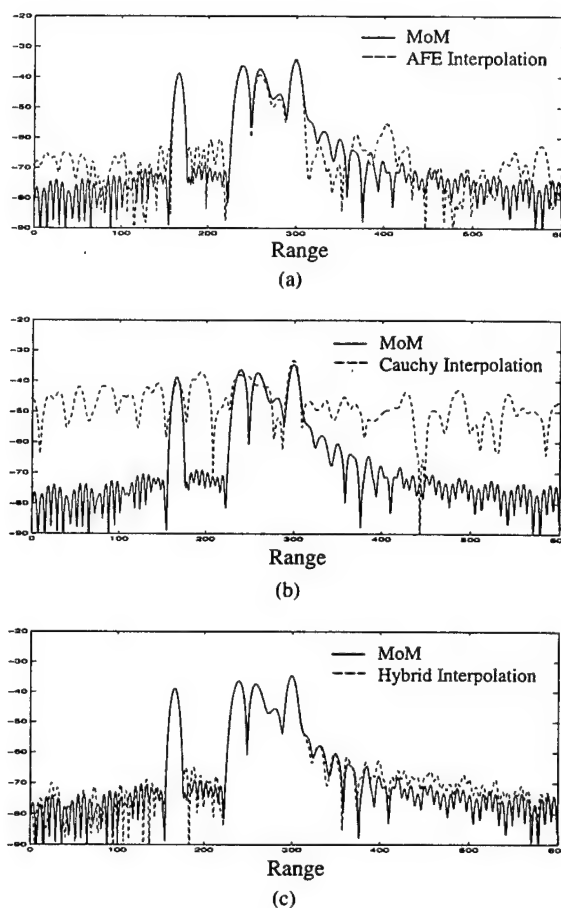


Figure 4 (a) Comparison of the range profiles generated from the brute-force MoM and the AFE-interpolated data. (b) Comparison of the range profiles generated from the brute-force MoM and the Cauchy-interpolated data. (c) Comparison of the range profiles generated from the brute-force MoM and the hybrid-interpolated data

be seen as dispersive ringing occurs after the third peak and overlaps with the fourth peak. We should note that the frequency response is marginally sampled at a step size of 0.1 GHz. Further undersampling will result in a loss of features in the frequency domain or aliasing in the time/range domain.

We next carry out the frequency interpolation using only 20 frequency points. The locations of the 20 frequency points are chosen semirandomly, as discussed in the last section, and are indicated as small arrows along the frequency axis in Figure 3. First, the target current is interpolated using the AFE algorithm based on the multiple-arrival model over the whole target surface. The interpolated result is plotted as the dashed line in Figure 3(a). Compared to the reference result from the brute-force MoM, AFE gives rather good performance, and can capture most of the features in the scattered field. The largest error in the AFE result occurs at frequencies around 4.5 and 9 GHz, which are close to the first two resonant frequencies of the small cavity. This observation is further corroborated in the corresponding range profile from the AFE-interpolated data, shown as the dashed curve in Figure 4(a). The AFE algorithm performs well in predicting the three strong peaks due to the exterior features on the target. However, it has trouble predicting the resonant cavity return, which is rather dispersive in range.

Next, the Cauchy method is used to interpolate the current over the entire target surface. The frequency response and the range profile results are shown, respectively, in Figures 3(b) and 4(b) as dashed lines. Since the rational function is a pole model, we find that the Cauchy algorithm tries hard to capture the poles of the system. However, since the current is sparsely sampled in frequency, an incorrect pole location and pole strength are generated. This is particularly true for low-order multiple-scattering events that have a large delay spread in the times of arrival. The long delay spread in time translates into rapid oscillations in the frequency response, and a very high model order is needed to adequately model the response using poles. From the range profile in Figure 4(b), we see that the Cauchy algorithm gives extremely poor results. Thus, the Cauchy algorithm cannot be used by itself to carry out the frequency interpolation of large targets that are dominated by ray-optical phenomena.

Finally, we apply the hybrid interpolation algorithm. The selection between the Cauchy-interpolated and the AFE-interpolated currents at each point on the target surface is made by comparing them against the reference current at three extra test frequencies. The chosen interpolated currents are then used to generate the backscattered field, as shown in Figure 3(c). When compared to Figure 3(a) and (b), the hybrid result shows an obvious improvement in its agreement with the reference result. Note that the error near the cavity resonant frequencies in Figure 3(a) is greatly reduced in Figure 3(c). The range profile in Figure 4(c) further substantiates this claim as both the scattering centers and the resonance of the cavity are well predicted.

Figure 5 shows how the whole target is automatically divided into two regions during the hybrid procedure, depending on the local scattering physics. The Cauchy region is shown within the open lines, while the AFE region is shown within the solid lines. The right half of the plate fits the multiple-arrival model very well, and thus is chosen as the AFE region. The cavity in the middle exhibits strong resonance, and can be well parameterized by the Cauchy method. As for the left half of the plate, we expect it to be an AFE region with the same scattering mechanisms as the right-half part. However, since the delay spread in the times of arrival between the direct incident wave and the scattered wave from the fin at the left edge is small, the Cauchy method has a

sufficient model order to parameterize the scattering behavior. In fact, we find that either the Cauchy or the AFE model may be chosen in this region with equally good results.

4. SUMMARY

In this paper, we have proposed a frequency-interpolation algorithm for electromagnetic scattering data from large, complex targets. It is based on the hybridization of the existing multiple-arrival model and the rational-function model. The adaptive feature extraction algorithm is used to extract the parameters in the multiple-arrival model, while the parameters in the rational-function model are obtained using the Cauchy method. At each point on the target, we first parameterize the induced current using both the AFE and Cauchy algorithms separately. The model that best matches the scattering physics at that location is automatically chosen based on the resulting interpolation error. Consequently, those regions on the target that are best described by ray-optical phenomena are interpolated by the multiple-arrival model, while those regions that exhibit resonance phenomena are interpolated by the rational-function model. Numerical results for a target containing complex features have demonstrated that the hybrid model results in more accurate interpolation than either of the two models alone. The hybrid interpolation scheme is quite robust, and can lead to significant computational savings since broadband signature data can be generated from a very sparse set of computed frequency points. Extension of this algorithm to 3-D, nonconducting targets is currently being investigated.

REFERENCES

1. Y. Wang and H. Ling, Efficient radar signature prediction using a frequency-aspect interpolation technique based on adaptive feature extraction, *IEEE Trans Antennas Propagat* (submitted, June 1999).
2. Y. Wang and H. Ling, Adaptive ISAR construction from non-uniformly undersampled data, *IEEE Trans Antennas Propagat*, 48 (2000), 329-331.
3. E.K. Miller, Model-based parameter estimation in electromagnetics: Part I. Background and theoretical development, *Appl Comput Electromag Newsletter* 10 (1995).
4. G.J. Burke, E.K. Miller, S. Chakrabarti, and K. Demarest, Using model-based parameter estimation to increase the efficiency of the computing electromagnetic transfer functions, *IEEE Trans Magn*, 25 (1989), 2807-2809.
5. R.S. Adve, T.K. Sarkar, D.M. Rao, E.K. Miller, and D.R. Pflug, Application of the Cauchy method for extrapolating/interpolating narrow band system responses, *IEEE Trans Microwave Theory Tech*, 45 (1997), 837-845.
6. K. Kottapalli, T.K. Sarkar, Y. Hua, E.K. Miller, and G.J. Burke, Accurate computation of wide-band response of electromagnetic systems utilizing narrow-band information, *IEEE Trans Microwave Theory Tech*, 39 (1991), 682-687.
7. C.J. Reddy, M.D. Deshpande, C.R. Cockrell, and F.B. Beck, Fast RCS computation over a frequency band using method of moments in conjunction with asymptotic waveform evaluation technique, *IEEE Trans Antennas Propagat*, 46 (1998), 1229-1233.
8. F. Ling, D. Jiao, and J.M. Jin, Efficient electromagnetic modeling of microstrip structures in multilayer media, *IEEE Trans Microwave Theory Tech*, 47 (1999), 1810-1818.
9. M. Hurst and R. Mittra, Scattering center analysis via Prony's method, *IEEE Trans Antennas Propagat*, AP-35 (1987), 986-988.
10. L.C. Potter, D.M. Chiang, R. Carriere, and M.J. Gerry, A GTD-based parametric model for radar scattering, *IEEE Trans Antennas Propagat*, 43 (1995), 1058-1067.
11. Y. Wang and H. Ling, Radar signature prediction using moment

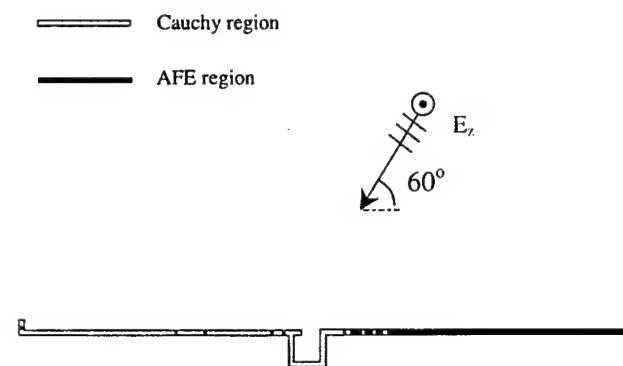


Figure 5 Illustration of how different portions of the target are parameterized in the hybrid approach. The Cauchy region is shown within the open lines, and the AFE region is shown within the solid lines

method codes via a frequency extrapolation technique, *IEEE Trans Antennas Propagat*, 47 (1999), 1008–1015.

12. A. Moghaddar, Y. Ogawa, and E.K. Walton, Estimating the time-delay and frequency delay parameter of scattering components using a modified MUSIC algorithm, *IEEE Trans Antennas Propagat*, 42 (1994), 1412–1418.
13. T. Su, Y. Wang, and H. Ling, A frequency extrapolation technique for computing antenna-platform radiation problem, *IEEE Trans Antennas Propagat* (submitted, Sept. 1999).
14. J. Moore and H. Ling, Super-resolved time-frequency analysis of wideband backscattered data, *IEEE Trans Antennas Propagat*, 43 (1995), 623–626.

© 2000 John Wiley & Sons, Inc.

The Effect of Mutual Coupling on Direction Finding in Smart Antenna Applications

Kapil R. Dandekar, Hao Ling and Guanghan Xu

Electromagnetic computation is used to account for mutual coupling effects in a smart antenna system and improve the performance of direction of arrival (DOA) estimation. Experimental results of the Bartlett and Multiple Signal Classification (MUSIC) DOA algorithms for mobile users transmitting at 1.8 GHz are given.

Keywords: Antenna Arrays, Array Signal Processing, Mutual Coupling

Introduction: The effect of mutual coupling on antenna arrays has long been recognized in the array processing community [1-5]. In particular, our past experimental studies using a smart antenna testbed showed anomalous DOA results [6]. For a single mobile user in an open field environment, the spatial spectra using a uniform circular array (UCA) showed a large sidelobe not corresponding to any signal multipath or interference. The presence of this sidelobe offset by 180° from the direct path signal component led to use of the term “rebound” sidelobe to describe this phenomenon. Initial speculation attributed the cause of rebound to be either mutual coupling or amplitude and phase mismatch between array elements.

In this letter, we set out to explain and remove the rebound anomaly. Our approach is to compute the array response including mutual coupling effects using the computational

electromagnetics solver Numerical Electromagnetics Code (NEC) [7]. This computed array response is then applied to DOA estimation using measurement data collected from our smart antenna testbed. Our results show that the rebound sidelobe is reduced significantly when mutual coupling is taken into consideration.

Array Mathematical Model: Assume that there are M elements in the base station antenna array located at (x_i, y_i) , $1 \leq i \leq M$. A steering vector characterizes the relative phase response of each antenna array element to an incident signal with DOA θ . An expression for the i^{th} component of the theoretical (“uncompensated”) steering vector is given by Equation (1):

$$\mathbf{a}_i(\theta) = \exp(-jk(x_i \cos \theta + y_i \sin \theta)) \quad (1)$$

where k is the wavenumber of the incident electromagnetic radiation. An array manifold matrix contains as its columns a collection of steering vectors corresponding to a set of angles. DOA algorithms, such as Bartlett and MUSIC, use knowledge of the steering vector to generate a spatial spectrum that gives signal power versus direction. The equations for the Bartlett and MUSIC spatial spectra are given respectively as [8]:

$$\mathbf{P}_{\text{BARTLETT}}(\theta) = (\bar{\mathbf{a}}^H(\theta) \tilde{\mathbf{R}} \bar{\mathbf{a}}(\theta)) / (\bar{\mathbf{a}}^H(\theta) \bar{\mathbf{a}}(\theta)) \quad (2)$$

$$\mathbf{P}_{\text{MUSIC}}(\theta) = (\bar{\mathbf{a}}^H(\theta) \bar{\mathbf{a}}(\theta)) / (\bar{\mathbf{a}}^H(\theta) \Pi^\perp \bar{\mathbf{a}}(\theta)) \quad (3)$$

where $\tilde{\mathbf{R}}$ is the estimated array data covariance matrix and Π^\perp is the estimated noise subspace obtainable through an eigenvalue decomposition of $\tilde{\mathbf{R}}$. The standard approach to DOA estimation is to use the ideal steering vector given in Equation (1) in the above expressions. However, possible interactions among the antenna elements are neglected.

Array Response Including Mutual Coupling: To properly account for mutual coupling, NEC simulation is used to compute the actual array response ("compensated" steering vectors) to incident signals from each direction about the array. The array elements are each four collinear half-wave dipoles. Each of the dipole elements is represented as a wire divided into segments for NEC analysis. Lump loading is used to model the isolation between the dipole antennas and the load impedance of the array elements. To simulate the array response to a signal from a particular DOA, the induced currents on the dipole elements due to a plane wave incident from that DOA are first computed. The array response is the vector of received voltages across the load impedance of each antenna element. The complete array manifold containing the array response from all simulated incident DOAs is used when performing uplink DOA analysis with measurement data.

Experiment Setup: Measurements using the smart antenna testbed were made in an open field. A 7-element UCA with an operating frequency of 1.88 GHz was used. The immediate environment was grassy with buildings off in the distance. There were up to two signal generators with dipoles used to represent mobile users transmitting to the basestation. Data was collected using the testbed and uplink spatial spectra were considered for each generator transmitting individually and both generators transmitting together.

Results: Figure 1 shows the spatial spectrum generated using the Bartlett DOA algorithm for measurement data due to a single mobile user located at 48° . The dashed

curve is generated using uncompensated steering vectors and shows a large rebound sidelobe at 210° . The solid curve is generated using the NEC-computed array response that takes into account mutual coupling. While the effect on the detected DOA and main lobe is minimal, the rebound lobe is significantly reduced through use of compensation. Figure 2 shows the MUSIC spatial spectrum using uncompensated and compensated steering vectors for the same mobile user. Again, the rebound lobe near 210° is reduced. In addition, the main lobe indicating the actual DOA is sharpened. Measurements at a number of different angles about the array nearly always verified these results for both DOA algorithms.

Figure 3 shows the uncompensated and compensated MUSIC spatial spectra for a situation in which there are two mobile users (located at 30° and 78°) transmitting simultaneously. In particular, compensation allows the DOAs of the users to be made much more prominent compared to the sidelobes. For all tested cases, mutual coupling compensation typically reduced sidelobes not corresponding to mobile users by approximately 3 dB. These sidelobes could be mistaken for either another mobile user or multipath signal energy.

Conclusions: The anomalous direction finding results observed in a smart antenna testbed has been explained in terms of mutual coupling effects. This work shows how off-line calculations using the widely available NEC can improve direction finding performance in smart antenna systems without the need for costly field calibration. The

improvement comes in the form of reduced rebound sidelobes that could be mistaken for interference or multipath signal energy.

Acknowledgements: This work is supported by the Texas Higher Education Coordinating Board under the Texas Advanced Technology Program and by the Office of Naval Research under contract no. N00014-98-1-0178.

References

- [1] T. Svantesson, *Direction Finding in the Presence of Mutual Coupling*, Chalmers University of Technology Technical Report No. 307L, 1999.
- [2] A. Lemma, E. Deprettere, and A. van der Veen, "Experimental Analysis of Antenna Coupling for High-Resolution DOA Estimation Algorithms," *1999 IEEE 2nd Workshop on Signal Processing Advances in Wireless Communications*, pp. 362-365, July 1999.
- [3] T. Su, K. R. Dandekar, and H. Ling, "Simulation of Mutual Coupling Effect in Circular Arrays for Direction Finding Applications," to appear in *Microwave and Optical Technology Letters*, Sept. 2000.
- [4] K. Pasala and E. Friel, "Mutual Coupling Effects and Their Reduction in Wideband Direction of Arrival Estimation," *IEEE Trans. on Aerospace and Electronic Systems*, vol. 30, no. 4, Oct. 1994.
- [5] R. Adve and T. Sarkar, "Compensation for the Effects of Mutual Coupling on Direct Data Domain Adaptive Algorithms," vol. AP-48, no. 1, Jan. 2000.
- [6] A. Kavak, *Vector Propagation Channel Studies for Smart Antenna Wireless Communication Systems*, Ph.D. Dissertation, The University of Texas at Austin, Jan. 2000.
- [7] G. J. Burke and A. J. Poggio, "Numerical Electromagnetics Code (NEC)-method of moments," Technical Document 11, Naval Ocean Systems Center, San Diego, Calif., Jan. 1981.
- [8] H. Krim and M. Viberg, "Two Decades of Array Signal Processing Research: The Parametric Approach," *IEEE Signal Processing Magazine*, pp. 67-94, July 1996.

Authors' affiliations:

K. R. Dandekar, H. Ling and G. Xu (Department of Electrical and Computer Engineering, University of Texas at Austin, Engineering Science Building 143, Austin, TX 78712, USA)

Corresponding Author Email Address: dandekar@ece.utexas.edu

Figure Captions

Figure 1 – Bartlett Spatial Spectrum for Single Mobile User at 48°

—— Compensated
— — Uncompensated

Figure 2 – MUSIC Spatial Spectrum for Single Mobile User at 48°

—— Compensated
— — Uncompensated

Figure 3 – MUSIC Spatial Spectrum for Two Mobile Users at 30° & 78°

—— Compensated
— — Uncompensated

Figure 1

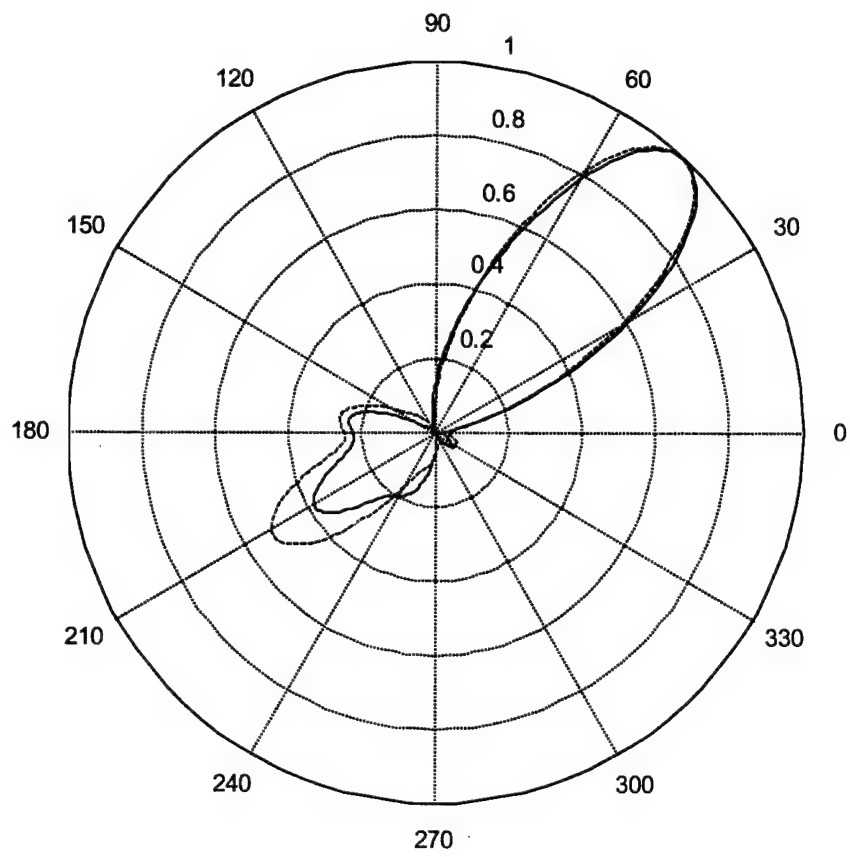


Figure 2

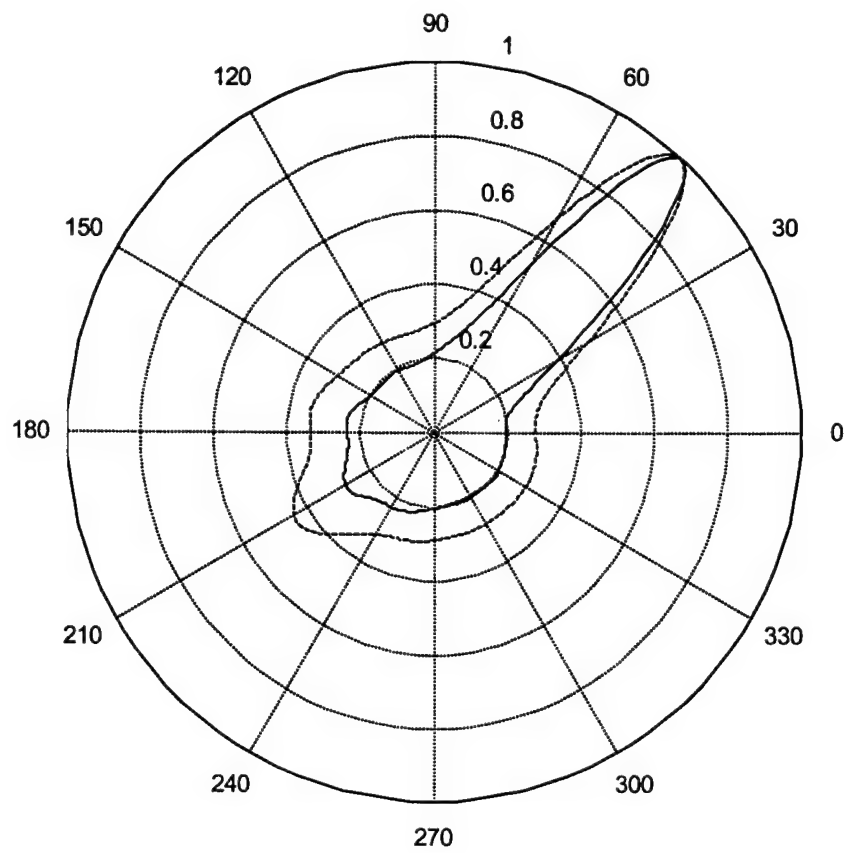
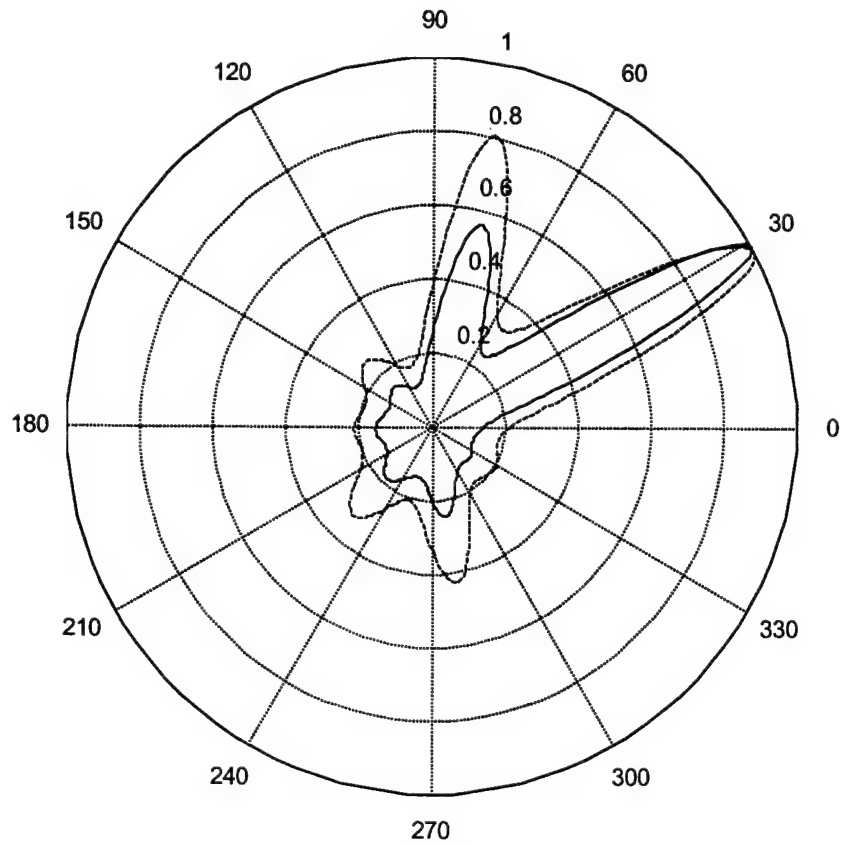


Figure 3



On Modeling Mutual Coupling in Antenna Arrays Using the Coupling Matrix

Tao Su and Hao Ling
Dept. of Electrical and Computer Engineering
The Univ. of Texas at Austin
Austin, TX 78712-1084

Abstract

The coupling matrix is a standard way to represent the mutual coupling effect between elements in an antenna array. In this paper, two commonly used approaches to determine the coupling matrix are examined and their limitations are discussed. The coupling matrix obtained from the minimum mean square error matching of the active and stand-alone element patterns is shown to be more effective than the mutual impedance approach. Furthermore, the coupling matrix model is extended for more complex antenna arrays and an example is provided to illustrate the effectiveness of the extended model.

Key Words: array mutual coupling, coupling matrix

I. Introduction

It is well known that the radiation/receiving pattern of an antenna element situated in an array environment can be quite different from its stand-alone pattern due to mutual coupling effects. The antenna element pattern in the array environment is called the active element pattern in the antenna community [1]. In applications such as direction finding, the active element patterns of the array elements are needed to carry out direction of arrival estimation. If the stand-alone element patterns are used instead of the active element patterns, significant degradation can result in array performance [2].

To properly account for the mutual coupling effect and for simplicity, it is customary to express the active element patterns as the product of a coupling matrix and the stand-alone element patterns. Although the coupling matrix concept is widely utilized for array signal processing, two very different approaches have been adopted in the literature to interpret and determine the coupling matrix. The first approach comes out of the antenna community. Gupta and Ksienski [3] first derived the coupling matrix from a microwave network point of view. The array is viewed as a multi-port network and it is shown that the coupling matrix can be simply related to the generalized impedance matrix of the multi-port network. Since the generalized impedance matrix is an intrinsic property of the antenna structure, such a derivation of the coupling matrix is quite attractive from fundamental electromagnetics point of view. This approach has been utilized and extended in a number of antenna mutual coupling studies [4-6].

The second approach originated from the array signal processing community. Friedlander and Weiss [7] first proposed a method for direction finding based on the coupling matrix model. In their view, the coupling matrix is simply an averaged effect of

the angular-dependent relationship between the active element patterns and the stand-alone element patterns. Based on this assumption, various array calibration procedures have been developed in which the coupling matrix is determined by minimum mean square error (MMSE) matching of the two sets of patterns at a few known incident angles [8,9].

While both of these approaches have been used with success on arrays consisting of simple dipole elements, the assumptions used in their derivation and the limitations of each approach have not been examined in detail in the literature. In this paper, we set out to compare the two different approaches for determining the coupling matrix. We first review the two approaches and discuss the limitations of each approach in Section II. In Section III, numerical results are generated using the standard numerical electromagnetic solver NEC [9] to verify our observations. In Section IV, we show that the coupling matrix model can be further extended for more complex antenna arrays and an example is provided to illustrate the effectiveness of the extended model.

II. Mutual coupling models

Assume an array with N elements is located in the xy -plane and receives a plane wave incident from angle ϕ in the azimuth plane. Let us consider a matrix relationship between the active element patterns and the stand-alone element patterns as:

$$\mathbf{A}_{true}(\phi) = \mathbf{M}\mathbf{A}_{theo}(\phi) \quad (1)$$

where \mathbf{A}_{true} and \mathbf{A}_{theo} are the active and stand-alone element patterns, respectively, and \mathbf{M} is the mutual coupling matrix. \mathbf{A}_{theo} has N rows with each row containing the stand-alone

element pattern for a particular element in the array. For the i^{th} row, it can be represented as:

$$a_i(\phi) = f_i(\phi) e^{jk(x_i \cos \phi + y_i \sin \phi)} \quad (2)$$

where $f_i(\phi)$ is the stand-alone element response as a function of ϕ and the exponential term is the explicit position-dependent phase delay for the i^{th} element located at (x_i, y_i) .

The stand-alone pattern matrix of the array is then defined as:

$$\mathbf{A}_{theo}(\phi) = [a_1(\phi) \ a_2(\phi) \ \cdots \ a_N(\phi)]^T \quad (3)$$

The active pattern matrix \mathbf{A}_{true} has the same structure as \mathbf{A}_{theo} , except that $a_i(\phi)$ is replaced by the active element pattern of the i^{th} element. The two different approaches in determining the mutual coupling matrix \mathbf{M} are discussed below.

A. The **Z** approach

In the first approach, the antenna array with N elements is viewed as an N port microwave network [3]. The relationship between the antenna terminal voltages and currents on reception under a plane wave excitation can be written as:

[illegible]

In the above expression, $V_{i,oc}$ is the received voltage at the i^{th} port when all the antenna terminals are open circuited, and Z_{ij} is the mutual impedance between the i^{th} and the j^{th} port defined as $Z_{ij} = V_i / I_j \Big|_{I_k=0, k \neq i}$. If we assume that each antenna is loaded by load

impedance Z_{iL} at its terminals and use the relationship $V_i = -Z_{iL}I_i$, we can express the terminal voltages in the following matrix form:

$$\begin{bmatrix} 1 + \frac{Z_{11}}{Z_{1L}} & \dots & \frac{Z_{1i}}{Z_{iL}} & \dots & \frac{Z_{1N}}{Z_{NL}} \\ \vdots & \ddots & \vdots & \ddots & \vdots \\ \frac{Z_{i1}}{Z_{1L}} & \dots & 1 + \frac{Z_{ii}}{Z_{iL}} & \dots & \frac{Z_{iN}}{Z_{NL}} \\ \vdots & \ddots & \vdots & \ddots & \vdots \\ \frac{Z_{N1}}{Z_{1L}} & \dots & \frac{Z_{Ni}}{Z_{iL}} & \dots & 1 + \frac{Z_{NN}}{Z_{NL}} \end{bmatrix} \begin{bmatrix} V_1 \\ \vdots \\ V_i \\ \vdots \\ V_N \end{bmatrix} = \begin{bmatrix} V_{1,oc} \\ \vdots \\ V_{i,oc} \\ \vdots \\ V_{N,oc} \end{bmatrix}$$

or

$$\mathbf{Z}\mathbf{V} = \mathbf{V}_{oc} \quad (5)$$

Note that if we stack columnwise the received voltage vectors \mathbf{V} obtained for different plane wave incident angles, the resulting matrix is in fact the active pattern matrix \mathbf{A}_{true} in equation (1) (apart from an unimportant scaling factor). Similarly, if we stack the open circuit voltage vectors \mathbf{V}_{oc} and assume that they are the same as the voltages received under stand-alone conditions, the resulting matrix is the stand-alone pattern matrix \mathbf{A}_{theo} . Therefore, the mutual coupling matrix in (1) can be written as:

$$\mathbf{M} = \mathbf{Z}^{-1} \quad (6)$$

This completes the derivation of \mathbf{M} under the \mathbf{Z} approach.

Since the normalized impedance \mathbf{Z} is intrinsic to the structure and is completely independent of angle, \mathbf{M} is also angle independent. This is a highly desirable conclusion. However, it hinges on the assumption that the received voltage at the terminals of an antenna when all the antenna elements are open-circuited is the same as the received voltage when all the other elements are absent. From the electromagnetic point of view, this is clearly not true as the induced currents on the antenna elements will not be

identically zero under the open circuit condition. As a result, the total voltage developed at the antenna terminals is not only due to the incident field, but also fields produced by the induced currents on other elements. Therefore, while equation (5) is always true, the coupling matrix \mathbf{M} given by (6) does not rigorously relate the active and stand-alone element patterns. Under certain situations, however, this model may work approximately. For example, if we consider an array comprising of half-wave dipole elements, the induced currents on every element should be very small under the open circuit condition and the \mathbf{Z} approach may be quite adequate. This will be examined numerically in Section III.

B. The C approach

In the second approach, the mutual coupling matrix is viewed as an average of the angular dependent relationship between the active and stand-alone element patterns [7]. Under this assumption, \mathbf{M} can be obtained by using the MMSE matching between the two patterns at a number of incident angles:

$$\mathbf{M} = \mathbf{C} = \mathbf{A}_{true} \mathbf{A}_{theo}^H (\mathbf{A}_{theo} \mathbf{A}_{theo}^H)^{-1} \quad (7)$$

We refer to the above formulation as the \mathbf{C} approach.

The effectiveness of the \mathbf{C} approach will now be examined from the induced current point of view based on the method of moments (MoM). In MoM, the integral equation of the induced currents on all the antennas in the array can be written into a matrix form as follows:

$$\mathbf{L}\mathbf{I} = \mathbf{V} \quad (8)$$

where \mathbf{I} is the current, \mathbf{V} is the incident plane wave excitation and \mathbf{L} is the moment matrix. Suppose we remove all but the i^{th} antenna in the array, we can find the stand-alone current distribution on the i^{th} antenna by solving a smaller moment system described by:

$$\mathbf{L}_i^0 \mathbf{I}_i^0 = \mathbf{V}_i \quad (9)$$

N such systems can be written for all the elements in the array. Since the right hand side is determined by the incident field only, it does not change whether the antenna is stand-alone or in the array environment. Thus we rewrite equation (8) as

$$[\mathbf{L}] \begin{bmatrix} \mathbf{I}_1 \\ \vdots \\ \mathbf{I}_N \end{bmatrix} = \begin{bmatrix} \mathbf{L}_1^0 & & \mathbf{0} \\ & \ddots & \\ \mathbf{0} & & \mathbf{L}_N^0 \end{bmatrix} \begin{bmatrix} \mathbf{I}_1^0 \\ \vdots \\ \mathbf{I}_N^0 \end{bmatrix}$$

or

$$\mathbf{L}\mathbf{I} = \mathbf{L}^0 \mathbf{I}^0 \quad (10)$$

By solving (10), the actual current distribution is related to the stand-alone current by

$$\mathbf{I} = \mathbf{L}^{-1} \mathbf{L}^0 \mathbf{I}^0 \quad (11)$$

Next we try to extract the currents at the terminals of the antenna elements from the \mathbf{I} vector and stack them over all the incident angles to arrive at the active pattern matrix \mathbf{A}_{true} . Similarly, we try to extract the terminal currents from the \mathbf{I}^0 vector and stack them to form the stand-alone pattern matrix \mathbf{A}_{theo} . First, we sift out the terminal currents from \mathbf{I} and the corresponding rows from the matrix $(\mathbf{L}^{-1} \mathbf{L}^0)$ in (11) to form:

$$\mathbf{I}_{term} = (\mathbf{L}^{-1} \mathbf{L}^0)_{term} \mathbf{I}^0 \quad (12)$$

where the subscript '*term*' indicates the rows corresponding to the antenna terminals.

Next, we sift out the terminal currents from \mathbf{I}^0 by writing:

$$\mathbf{I}^0 = \begin{bmatrix} \mathbf{S}_1 & & \mathbf{0} \\ & \ddots & \\ \mathbf{0} & & \mathbf{S}_N \end{bmatrix} \begin{bmatrix} I_{1,term}^0 \\ \vdots \\ I_{N,term}^0 \end{bmatrix} \quad (13)$$

where \mathbf{S}_i is the shape of the current distribution on the i^{th} element and $I_{i,term}^0$ is its corresponding terminal current. Substituting (13) into (12), we can find the relationship between the actual and stand-alone terminal currents. Note that the moment matrices \mathbf{L} and \mathbf{L}^0 are angular independent. If the shape of the current distribution on a stand-alone antenna element is also angular independent, then equation (12) can be rigorously cast into the form of (1). To summarize, we have shown that the relationship between the active element pattern and the stand-alone element pattern is angular independent provided that the shape of the current distribution on each stand-alone antenna element is independent of angle. When this condition is satisfied, the mutual coupling matrix can be effectively determined by (7).

Let us now examine when the angular-independent current shape condition can be met. The first situation has been discussed in [5], where all the antennas are vertical wires and the incident directions have the same elevation angle. In this case, the stand-alone current distribution of an antenna is exactly the same over all the incident angles. A second common situation is when the antenna elements are working near resonance. In this case, the stand-alone current distribution on an antenna is dominated by the resonant mode and thus has approximately the same shape over all the incident angles. An example of this situation is an array of half-wave dipoles.

III. Numerical examples

In this section, we illustrate the conditions for the **Z** and **C** approaches to be valid using computer simulation. We study a linear array consists of 4 dipoles, whose centers are spaced 0.45 wavelength apart, as shown in Fig. 1. The simulations are carried out using NEC.

In the first example, the dipoles are half wavelength in length. All the dipoles are loaded with 73 ohms of load impedance at the center. Elements 1 and 4 are rotated 45° and -45° , respectively, about the y axis. Elements 2 and 3 are rotated 45° and -45° , respectively, about the x axis. We determine the coupling matrix using both the **C** approach and the **Z** approach for this structure. The current at the center of each antenna is computed for incident angles from -90° to 90° at a step of 1° . This serves as the reference active element pattern. The values at $\pm 75^\circ$, $\pm 45^\circ$, and 0° are used to calculate the **C** matrix from (7). To determine the **Z** matrix, we first obtain the mutual admittance by short circuiting all the antenna ports, driving the j^{th} antenna with a voltage source, and computing $Y_{ij} = I_i / V_j \big|_{V_k=0, k \neq j}$. By inverting the resulting generalized admittance matrix, we get the mutual impedance Z_{ij} . The normalized impedance matrix **Z** is then obtained from (5).

Once we obtain the two coupling matrices, we use them to calculate the active element patterns from the stand-alone element patterns. Notice that since the elements are tilted, even the stand-alone element patterns are not isotropic. The active element patterns of antenna elements 1 and 2 are plotted in Figs. 2(a) and 2(b), respectively. The solid curves are the active element patterns directly computed by NEC. The dashed curves are obtained using the **Z** approach and the dotted lines are modeled using the **C** approach. We find that the dashed curves are quite close to the computed ones, but not exactly the

same. This is because the V_{oc} condition described in Section IIA is only approximately satisfied, even for an array of half-wave dipoles. On the other hand, the curves using the **C** approach match almost perfectly with the computed ones. In this case, the antennas operate in resonance and the stand-alone current distribution has the same shape over all incident angles, even though they are not all vertically aligned.

To further observe the effectiveness of the mutual coupling models, we apply the active element patterns to a direction finding problem, which is quite sensitive to the element patterns. Two uncorrelated incoming signals are assumed from the incident angles of 50° and 65° . The signal to noise ratio (SNR) is set to 30 dB. The angles of arrival are determined using the standard MUSIC algorithm, and the resulting normalized power spectra are plotted in Fig. 3. The solid curve is the result from the reference active element patterns. For comparison, the result by neglecting mutual coupling effect is obtained by using the stand-alone element patterns and is plotted as the dash-dot curve. The large degradation shows the importance of taking mutual coupling into consideration. The dashed curve is the result of the **Z** approach. The dotted curve is obtained using the **C** approach. It is observed that the **C** approach performs almost as well as the reference active element patterns, while the **Z** approach leads to some degradation in the peak position and width of the power spectra.

In the second example, we replace the half-wave dipole elements with full-wave dipoles. Compared with the previous example, the V_{oc} condition is strongly violated for the **Z** approach and the near-resonant condition is not satisfied for the **C** approach. Fig. 4 shows the computed and modeled active element patterns. This time, neither the **Z** nor the **C** approach is close to the reference result.

Finally we make the full wave dipoles perpendicular to the xy plane. Now the vertical wire condition is satisfied for the **C** approach. The resulting element patterns are plotted in Fig. 5. The **Z** approach still works poorly as in example 2. However, the **C** approach perfectly models the active element patterns. As discussed in the Section IIB, the matching in this case is exact.

IV. Extension of the mutual coupling model

As can be seen in the examples, the **C** approach is more accurate than the **Z** approach. Yet the situations when the **C** approach can be applied is still quite limited. The approach fails for more complex antenna structures. By observing equation (11) we can see that if the array elements consist of thin wires, each piece of the wires affects the active element pattern in the same manner as a dipole antenna. Thus for certain cases, the model in (1) can be extended to include the coupling from all parts of the array. For example, if we have an array of Yagi antennas, we may include the coupling from the parasitic elements to model the active element patterns more accurately. More specifically, we extend the model as follows:

$$\mathbf{A}_{true} = [\mathbf{C} \quad \mathbf{C}'] \begin{bmatrix} \mathbf{A}_{theo} \\ \mathbf{A}'_{theo} \end{bmatrix} \quad (14)$$

where \mathbf{A}'_{theo} is the stand-alone receiving patterns of the parasitic elements and \mathbf{C}' describes the coupling from the parasitic elements to the driven elements. Like the standard **C** approach, (14) is valid if all the parasitic elements are vertical or their lengths are close to resonant length. The MMSE matching can again be used to determine the coupling matrix, except that the number of incident angles needed to give a unique solution is increased.

As an example, we look at an array consisting of 4 parallel Yagi antennas as shown in Fig. 6(a). All the elements in the array are perpendicular to the xy -plane and the separation between two adjacent Yagis is 1 wavelength. Each Yagi antenna consists of 3 wires with the center wire being the driven element as shown in Fig. 6(b). The stand-alone element pattern is plotted in Fig. 6(c). Next, the coupling matrix in (14) is determined from the computed active element patterns at 12 incident angles uniformly distributed between -180° and 180° . The reference and the modeled active element patterns of the first and second antenna are plotted in Figs. 7(a) and 7(b), respectively. The solid curves are the reference patterns and the dotted curves are obtained using the extended-**C** approach. They match with the reference patterns very well. As a comparison, we also model the active element patterns using the **Z** approach and the **C** approach. The results are shown in dashes and dash-dot curves, respectively. The agreement is obviously not as good. This is because the open-circuit voltage condition does not hold for the **Z** approach and the constant current shape condition for each array element is violated for the **C** approach.

V. Conclusions

In this paper, the two commonly used approaches for determining the mutual coupling matrix in array antennas have been discussed. It has been shown that the **Z** approach is an approximation that applies when the element pattern under the open circuit condition can be well approximated by the stand-alone element pattern. It has also been shown that the **C** approach holds true whenever the current distribution of a stand-alone element has the same shape over all incident angles. This condition is satisfied for

vertical wire antennas or near-resonant antennas. We have found from our numerical examples that the **C** approach is in general more accurate than the **Z** approach. We have also extended the **C** approach to model more complex wire elements by considering each wire as an individual antenna. An example of an Yagi array has been provided to demonstrate the effectiveness of the extended-**C** model.

Acknowledgments

This work is supported by the Office of Naval Research under Contract No. N00014-98-1-0178, and in part by the Texas Higher Education Coordinating Board under the Texas Advanced Technology Program.

References

- [1] D. F. Kelley and W. L. Stutzman, "Array antenna pattern modeling methods that include mutual coupling effects," *IEEE Trans. Antennas Propagat.*, vol. 41, pp. 1625-1632, Dec. 1993.
- [2] T. Su, K. Dandekar and H. Ling, "Simulation of mutual coupling effect in circular arrays for direction finding applications," *Microwave Opt. Tech. Lett.*, vol. 26, pp. 331-336, Sept. 2000.
- [3] I. J. Gupta and A. A. Ksienski, "Effect of mutual coupling on the performance of adaptive arrays," *IEEE Trans. Antennas Propagat.*, vol. 31, pp. 785-791, Sept. 1983.

- [4] T. Svantesson, "Modeling and estimation of mutual coupling in a uniform linear array of dipoles," *IEEE Int. Conf. Acoust. Speech Signal Processing*, pp. 2961-2964, Phoenix, 1999.
- [5] C.-C. Yeh, M.-L. Leou and D. R. Ucci, "Bearing estimations with mutual coupling present," *IEEE Trans. Antennas Propagat.*, vol. 37, pp. 1332-1335, Oct. 1989.
- [6] R. S. Adve and T. K. Sarkar, "Compensation for the effects of mutual coupling on direct data domain adaptive algorithms," *IEEE Trans. Antennas Propagat.*, vol. 48, pp. 86-94, Jan. 2000.
- [7] B. Friedlander and A. J. Weiss, "Direction finding in the presence of mutual coupling," *IEEE Trans. Antennas Propagat.*, vol. 39, pp. 273-284, Mar. 1991.
- [8] C. M. S. See, "A for array calibration in parametric sensor array processing," *IEEE Singapore Int. Conf. on Communication Systems*, pp. 915-919, Singapore, 1994.
- [9] A. N. Lemma, E. F. Deprettere and A. J. Veen, "Experimental analysis of antenna coupling for high-resolution DOA estimation algorithms," *IEEE workshop on Signal Processing Advances in Wireless Communications*, pp. 362-365, Annapolis, MD, May 1999.
- [10] *NEC-2 Manual*, Lawrence Livermore National Laboratory, 1996.

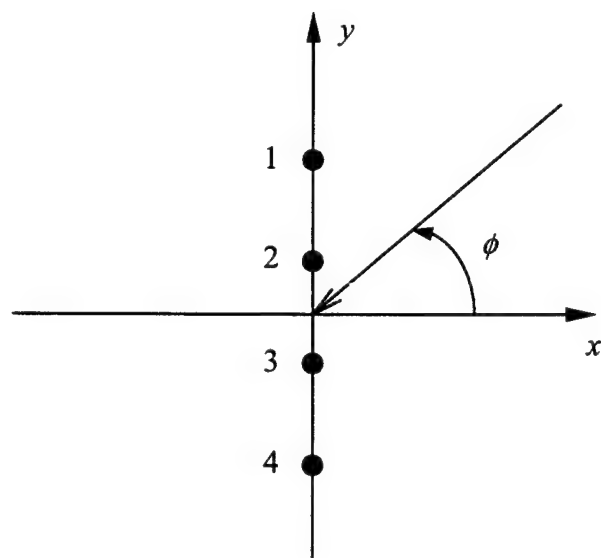
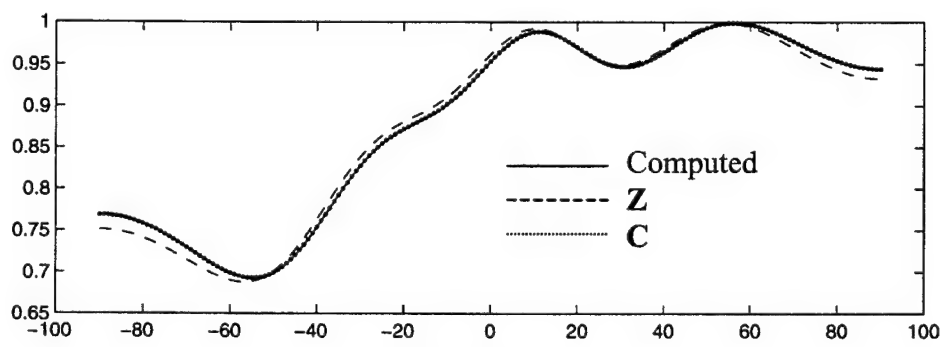
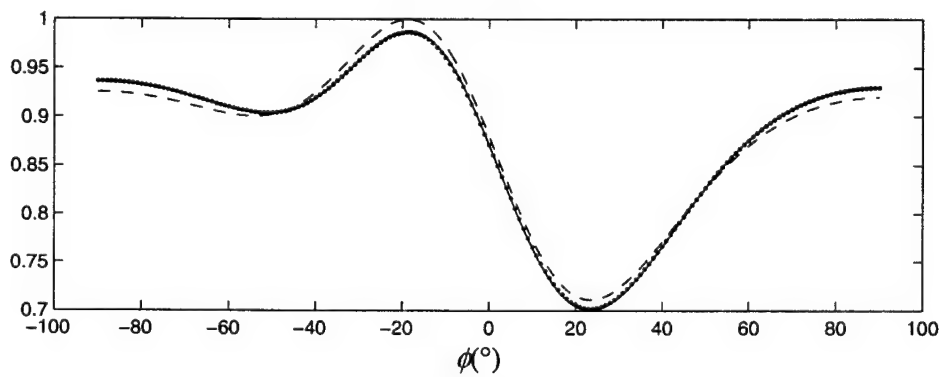


Fig. 1. Array Geometry



(a) element 1



(b) element 2

Fig. 2. Computed and modeled active element patterns for array of rotated half wave dipoles.

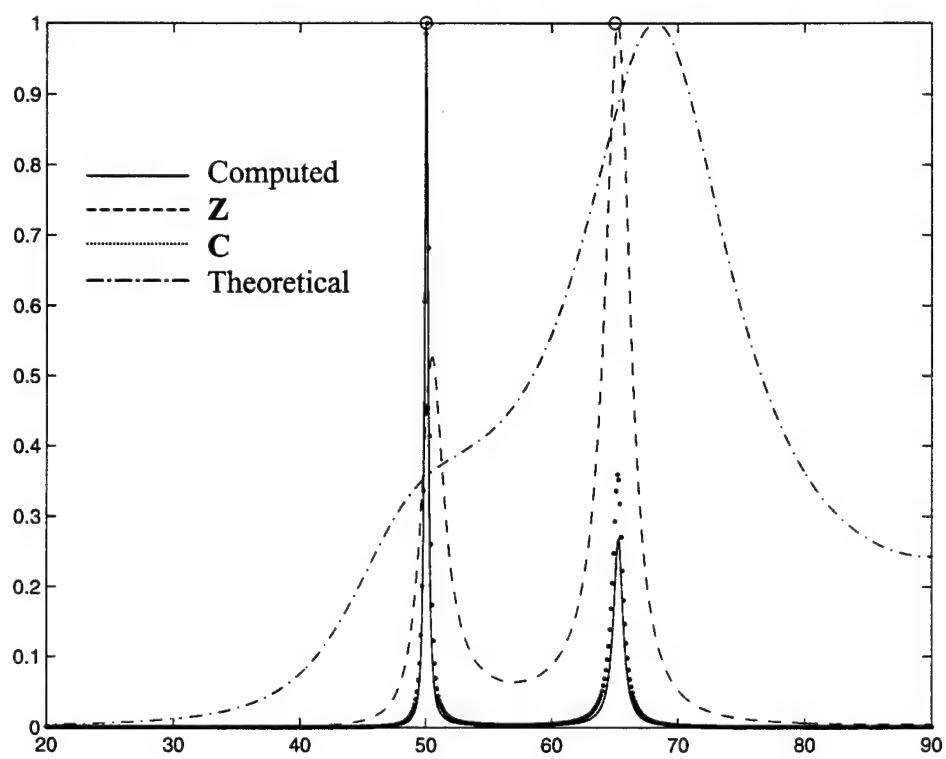
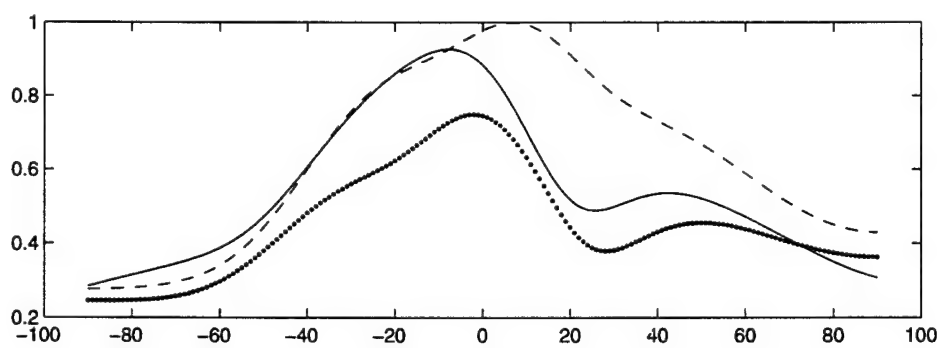
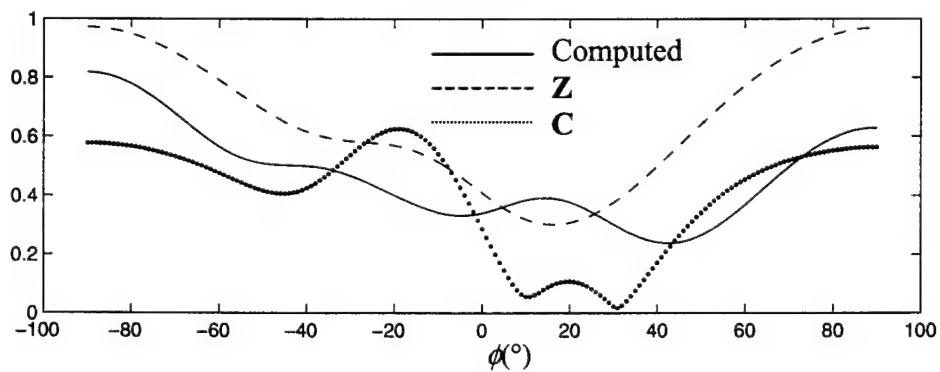


Fig. 3. Direction finding result using different element patterns

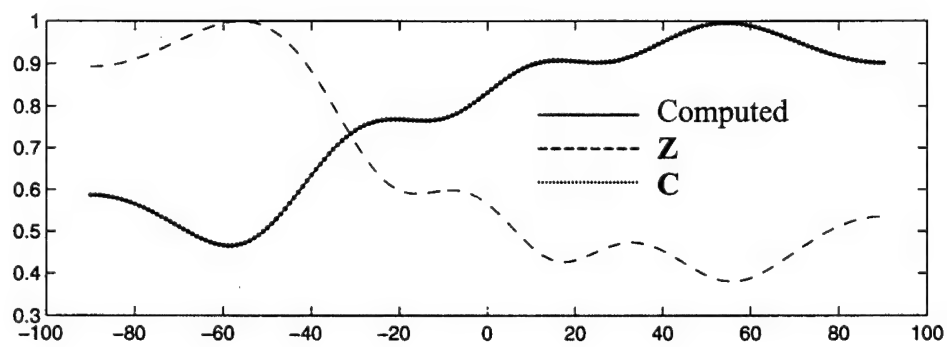


(a) element 1

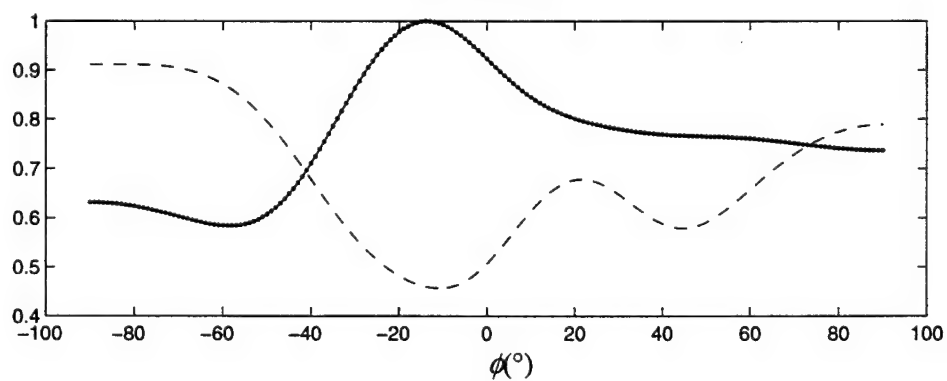


(b) element 2

Fig. 4. Computed and modeled active element patterns for array of rotated full wave dipoles.

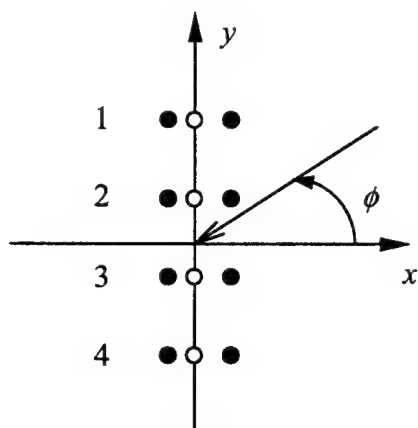


(a) element 1

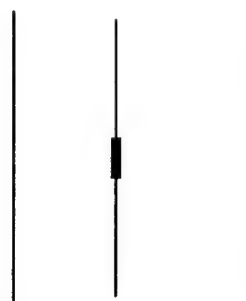


(b) element 2

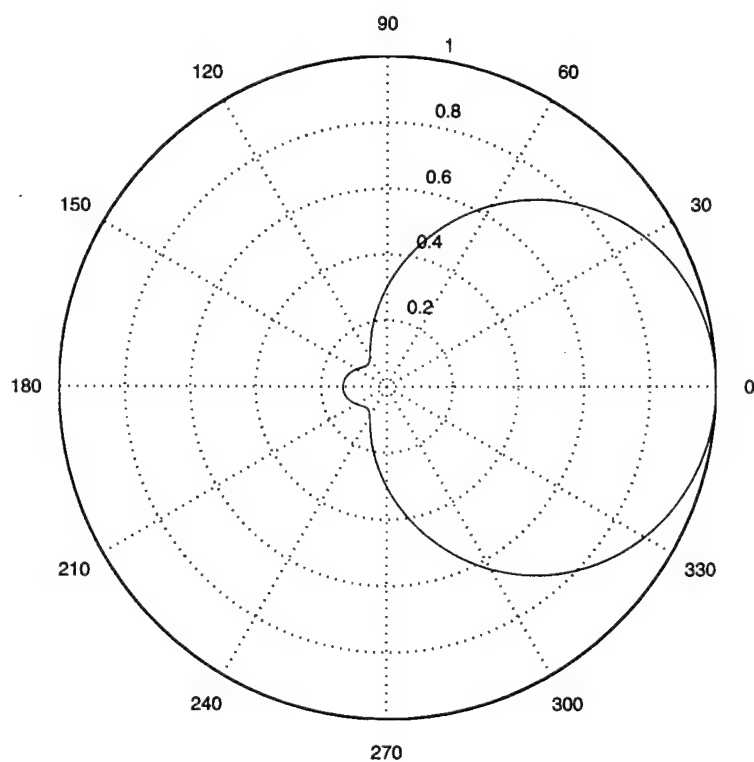
Fig. 5. Computed and modeled active element patterns for array of vertical full wave dipoles.



(a) Array geometry.



(b) Yagi element



(b) Stand-alone element pattern

Fig. 6. A 4-element array with Yagi elements

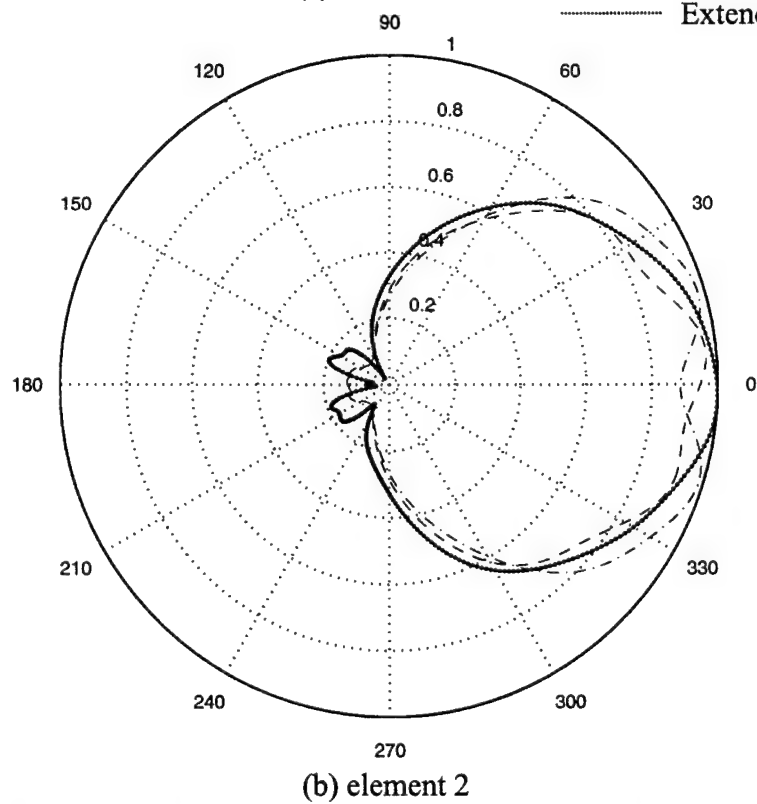
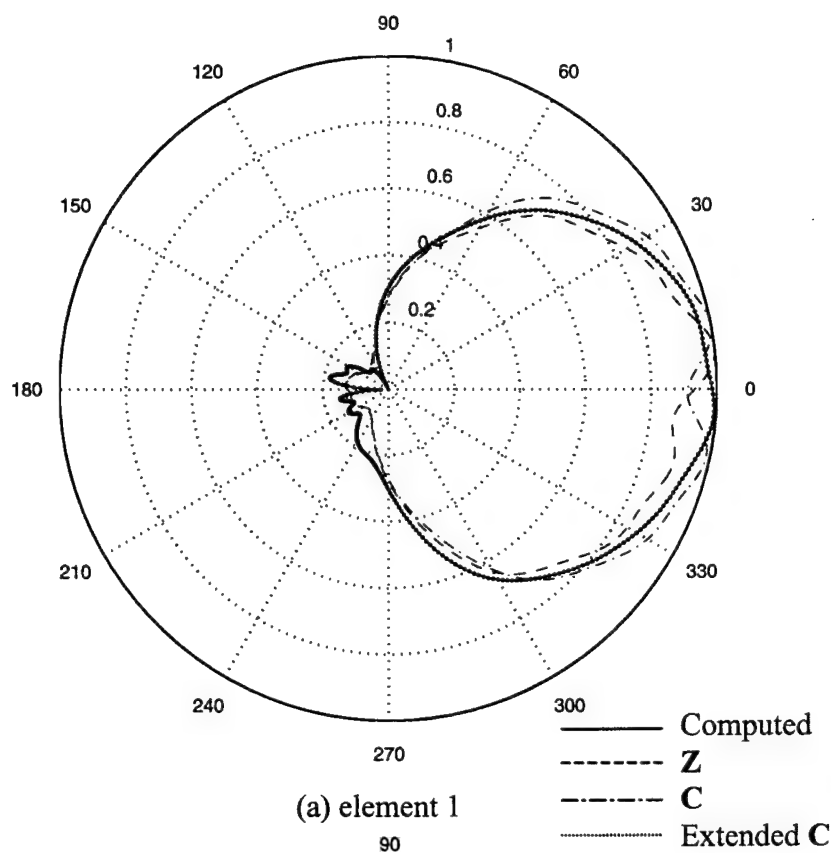


Fig. 7. Computed and modeled active element patterns for an array of Yagi antennas.

Shape Optimization of Broadband Microstrip Antennas Using the Genetic Algorithm

H. Choo, A. Hutani, L. C. Trintinalia⁺ and H. Ling

Department of Electrical and Computer Engineering
The University of Texas at Austin
Austin, TX 78712 U.S.A

⁺Department of Telecommunications and Control Engineering
Escola Politécnica da Universidade de São Paulo
São Paulo, Brazil

Abstract: The genetic algorithm (GA) is used to design patch shapes for microstrip antennas on FR-4 substrate for broadband applications. Measurement results of the GA-optimized designs show good agreement with numerical prediction. The optimized patch design achieves a four-fold improvement in bandwidth when compared to a standard square microstrip antenna.

Introduction: It is well known that standard microstrip patch antennas exhibit very narrow bandwidth. Various broadbanding methods have been proposed to date. For instance, adding parasitic patches, using thick air substrate, stacking patches and using shorting post for reactive loading are well known techniques to extend microstrip bandwidth [1]. Recently, Johnson and Rahmat-Samii reported

on the use of the genetic algorithm (GA) to search for novel patch shapes for broadband operation [2]. The attractiveness of GA shape optimization is that improved bandwidth performance can be achieved without increasing overall volume or manufacturing cost. They used thick air substrate, and explored metallic patch sizes up to half a wavelength.

In this paper, we also examine the use of GA for broadband applications. In contrast to the work of Johnson and Rahmat-Samii, we employ FR-4 as the substrate material, since it is the most commonly used material in wireless devices. In addition, fewer geometrical constraints are used in the GA in hope of obtaining better global optimum. We report a four-fold bandwidth improvement from our GA-optimized microstrip shape as compared to a standard square microstrip antenna.

GA Optimization: GA is implemented to optimize the microstrip patch shape in order to achieve broad bandwidth. In our GA, we use a two-dimensional (2-D) chromosome to encode each patch shape into a binary map [3]. The metallic sub-patches are represented by ones and the no-metal areas are represented by zeros. Since it is more desirable to obtain optimized patch shapes that are well-connected from the manufacturing point of view, a 2-D median filter is applied to the chromosomes to create a more realizable population at each generation of the GA.

To evaluate the performance of each patch shape, a full-wave electromagnetic patch code is used to predict its bandwidth performance [4]. The formulation of the code is similar to that described in [5] and is based on the solution to the electric field integral equation with the periodic, layered medium Green's function as its kernel. Roof-top basis functions are used to expand the unknown current on the metal patch and fast Fourier transform is used to accelerate the computation of the matrix elements. Because of the assumed periodicity of the patches in this code, we use a large enough period to simulate a single patch.

The design goal is to broaden the bandwidth of a microstrip antenna with a center frequency of 2 GHz by changing the patch shape. To achieve the design goal, the cost function is defined as the average of those S_{11} values that exceeds -10dB (i.e., VSWR=2:1) within the frequency band of interest. The target frequency range is between 1.9 GHz and 2.1 GHz.

Based on the cost function, the next generation is created by a reproduction process that involves crossover, mutation and 2-D median filtering. A 2-point crossover scheme using three chromosomes is devised. The process selects three chromosomes as parents, and divides each chromosome into three parts. Intermingling the three parent chromosomes then makes three child chromosomes. This crossover scheme exhibits a more disruptive characteristic for regeneration

than the conventional 1-point or 2-point crossover. It serves to counteract against the median filtering effect and is found to result in better convergence rate. The reproduction process is iterated until the cost function converges to a minimum value.

Results: Fig. 1(a) shows the shape of the GA-optimized microstrip. A 72mm \times 72mm square design area in which the metallic patch can reside is discretized into a 16 \times 16 grid for the chromosome definition. The thickness of the FR-4 substrate (dielectric constant of 4.3) is 1.6 mm. In the GA-optimized shape, the gray pixels are metal and the white pixels have no metal. The white dot shows the position of the probe feed. To experimentally verify the GA design, we have built and measured such a microstrip patch. Fig. 1(b) shows the return loss comparison between the measurement and simulation results. The solid line is the measurement result taken from an HP8753C network analyzer. The square dots represent the simulation result. Good agreement can be observed between the measurement and simulation. The graph shows a bandwidth of 6.16% by simulation and 6.18% by measurement. This is about three times that of a square microstrip antenna (36 mm \times 36 mm), which has a bandwidth of 1.98%. Further improvements in the bandwidth can be obtained from the GA by increasing the grid resolution from 16 \times 16 to 32 \times 32. Figs. 2 (a) and 2 (b) show respectively the GA-optimized patch

shape and the bandwidth performance in the higher resolution design. The bandwidth is found to be 8.04% by simulation and 8.10% by measurement. This is about four times that of a square microstrip antenna.

Finally, the operating principle of the GA-optimized shape is interpreted. It is clear from the two frequency dips in Fig. 2(b) that the antenna contains two operating modes that are very closely spaced in frequency. We have verified the two modes by examining the current distributions on the patch at 1.99 and 2.07 GHz. In addition to the dual-mode principle, another important bandwidth enhancement effect is achieved through the ragged edge shape. We have found that when the patch is restricted to single-mode operation (by imposing symmetry constraints), the introduction of ragged edges in the GA-optimized shape can enhance the bandwidth by about 30%. Therefore, the GA-optimized design combines both the dual-mode operation and ragged edge shape to achieve the broadest bandwidth.

Conclusions: Optimized patch shapes for microstrip antennas on thin FR-4 substrate have been investigated using the genetic algorithm. The optimized shape shows a four-fold improvement in bandwidth when compared to a standard square microstrip antenna. This result has been verified by laboratory measurement. The

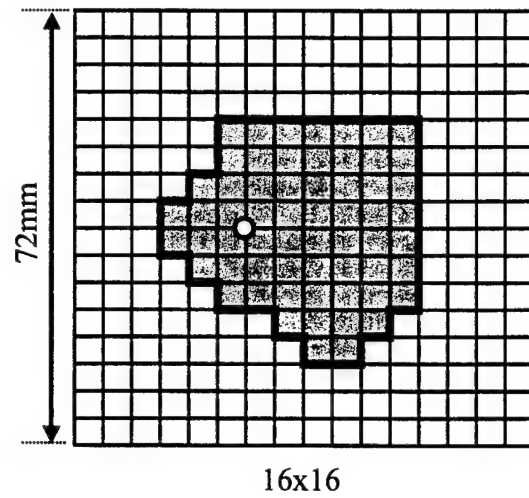
basic operating principle of the optimized shape can be explained in terms of a combination of dual-mode operation and ragged edge shape.

References

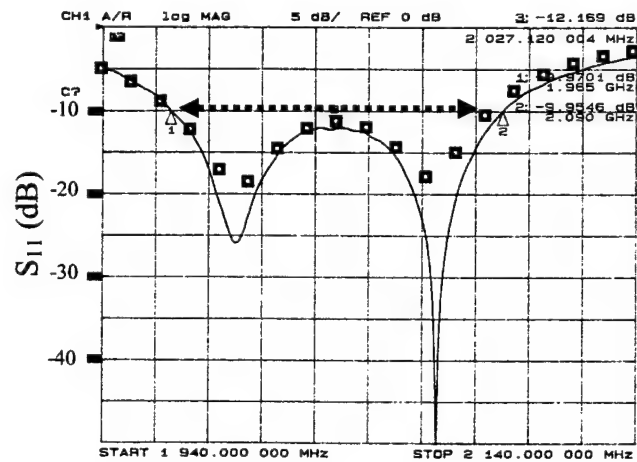
- [1] J. R. James, P. S. Hall, Handbook of Microstrip Antennas, vol. 1. London: Peter Peregrinus, 1989.
- [2] J. M. Johnson, Y. Rahmat-Samii, "Genetic Algorithms and Method of Moments (GA/MOM) for the Design of Integrated Antennas," *IEEE Trans. Antennas Propagat.*, vol. 47, pp. 1606-1614, Oct. 1999.
- [3] M. Villegas, O. Picon, "Creation of New Shapes for Resonant Microstrip Structures by Means of Genetic Algorithms," *Elec. Lett.*, vol. 33, pp. 1509-1510, Aug. 1997.
- [4] L. C. Trintinalia, "Electromagnetic Scattering from Frequency Selective Surfaces," M.S. Thesis, Escola Politécnica da Univ. de São Paulo, Brazil, 1992.
- [5] T. Cwik, R. Mittra, "Scattering from a Periodic Array of Free-Standing Arbitrarily Shaped Perfectly Conducting or Resistive Patches," *IEEE Trans. Antennas Propagat.*, vol. 35, pp.1226-1234, Nov. 1987.

Acknowledgments

This work is supported by the Office of Naval Research under Contract No. N00014-98-1-0178, the Air Force MURI Center for Computational Electromagnetics under Contract No. AFOSR F49620-96-1-0025, and the Texas Higher Education Coordinating Board under the Texas Advanced Technology Program.

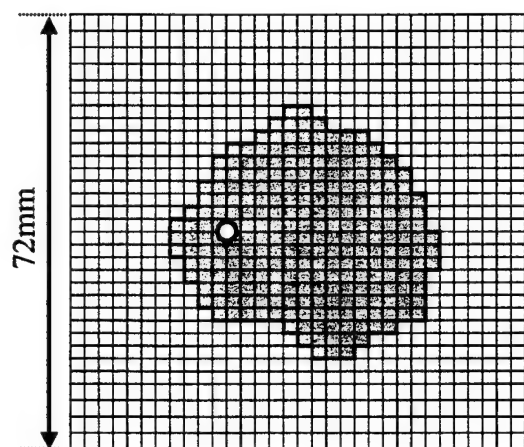


(a)



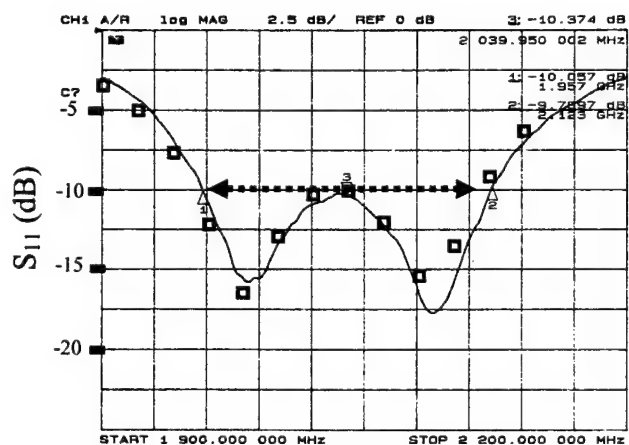
(b)

Fig. 1. (a) GA-optimized microstrip antenna using 16×16 resolution within a $72\text{mm} \times 72\text{mm}$ area. The gray pixels are metal and the white dot shows the position of the probe feed. (b) Return loss (dB) of the GA-optimized antenna from simulation (—) and measurement (\square).



32x32

(a)



(b)

Fig. 2. (a) GA-optimized microstrip antenna using 32x32 resolution within a 72mm x 72mm area. The gray pixels are metal and the white dot shows the position of the probe feed. (b) Return loss (dB) of the GA-optimized antenna from simulation (—) and measurement (\square).

A Wavelet-Based Preconditioner for Three-Dimensional Electromagnetic Integral Equations

H. Deng and H. Ling

Department of Electrical and Computer Engineering
The University of Texas at Austin
Austin, TX 78712-1024

Indexing terms: Wavelet Transform, Method of Moments, Preconditioning

A wavelet-based method is proposed to effectively precondition 3-D electromagnetic integral equations. The approximate-inverse preconditioner is constructed in the wavelet domain where both the moment matrix and its inverse exhibit sparse, multilevel finger structures. The inversion is carried out as a Forbenius-norm minimization problem. Numerical results on a 3-D cavity show that the iteration numbers are significantly reduced with the preconditioned system. The computational cost of the preconditioner is kept under $O(N\log N)$.

Introduction: There is growing interest in the computational electromagnetics community on the use of the fast multipole method (FMM) [1] for solving large-scale electromagnetic integral equations. With the multi-level implementation of the FMM, the computational complexity and storage requirement can be reduced to $O(N\log N)$ for the (moment matrix)-(vector) product. In order to take advantage of this reduced complexity, iterative solvers must be used. However, the convergence rate of the iterative solution process is strongly problem-dependent. For scattering geometries involving multiple interactions such as partially open cavities, the moment matrices are severely ill-conditioned and preconditioning is need to accelerate the convergence rate [2]. Some well-documented preconditioning methods such as incomplete LU-factorization (ILU) [3] may be effective, but usually require well-above $O(N\log N)$

complexity to implement. In this work, we propose a new wavelet-based method to construct an effective preconditioner for 3-D moment equations. The algorithm is based on determining an approximate inverse for the moment matrix in the wavelet transform domain. The computational cost of the preconditioner is kept under $O(N \log N)$, making it compatible with the FMM.

Problem Formulation: Consider a 3-D moment equation in the space domain:

$$[\mathbf{Z}]\mathbf{J} = \mathbf{E} \quad (1)$$

where $[\mathbf{Z}]$, \mathbf{J} , and \mathbf{E} are respectively the moment matrix, the induced current vector, and the excitation vector. If (1) is left-preconditioned by a preconditioner $[\mathbf{P}]$, we obtain:

$$[\mathbf{P}][\mathbf{Z}]\mathbf{J} = [\mathbf{P}]\mathbf{E} \quad (2)$$

Our approach is to try to construct a $[\mathbf{P}]$ that is the approximate inverse of $[\mathbf{Z}]$ using the wavelet transform. The moment equation in (1) can be represented using wavelet basis as:

$$[\tilde{\mathbf{Z}}]\tilde{\mathbf{J}} = \tilde{\mathbf{E}} \quad (3)$$

where

$$[\tilde{\mathbf{Z}}] = [\mathbf{M}]^T [\mathbf{Z}] [\mathbf{M}], \quad [\tilde{\mathbf{J}}] = [\mathbf{M}]^T \mathbf{J}, \quad [\tilde{\mathbf{E}}] = [\mathbf{M}]^T \mathbf{E}, \quad (4)$$

and $[\mathbf{M}]$ is the unitary wavelet transform matrix. Note that in 3-D problems $[\mathbf{Z}]$ is strongly diagonal-dominant. Consequently, $[\tilde{\mathbf{Z}}]$ can be effectively approximated by a sparse matrix with the multi-level “finger” pattern discussed in [4]. Furthermore, we observe from (4) that:

$$[\tilde{\mathbf{Z}}]^{-1} = [\mathbf{M}]^T [\mathbf{Z}]^{-1} [\mathbf{M}] = [\tilde{\mathbf{Z}}]^{-1} \quad (5)$$

Since the smooth parts in $[\mathbf{Z}]^{-1}$ are converted into small wavelet coefficients through the transform, $[\tilde{\mathbf{Z}}]^{-1}$ can again be approximated by a sparse matrix with the same finger

pattern as $[\tilde{\mathbf{Z}}]$. With the chosen sparsity pattern for both $[\tilde{\mathbf{Z}}]$ and $[\tilde{\mathbf{Z}}]^{-1}$, the approximate-inverse preconditioner for $[\tilde{\mathbf{Z}}]$ can now be solved efficiently by casting it as a Forbenius-norm minimization problem [5]:

$$\text{Min}_{[\tilde{\mathbf{P}}]} \|[\tilde{\mathbf{P}}][\tilde{\mathbf{Z}}] - \mathbf{I}\|_F \quad (6)$$

where \mathbf{I} is the identity matrix. Since

$$\|[\tilde{\mathbf{P}}][\tilde{\mathbf{Z}}] - \mathbf{I}\|_F = \sum_{j=1}^N \|\tilde{\mathbf{P}}_j[\tilde{\mathbf{Z}}] - \mathbf{e}_j\|^2 \quad (7)$$

where $\tilde{\mathbf{P}}_j$ and \mathbf{e}_j are respectively the j -th rows of $[\tilde{\mathbf{P}}]$ and \mathbf{I} , the solution of (6) becomes the following N independent least squares problems:

$$\text{Min}_{\tilde{\mathbf{P}}_j} \|\tilde{\mathbf{P}}_j[\tilde{\mathbf{Z}}] - \mathbf{e}_j\|^2, \quad j = 1, 2, \dots, N \quad (8)$$

Once $[\tilde{\mathbf{P}}]$ is solved for in the wavelet domain, the approximate-inverse preconditioner $[\mathbf{P}]$ can be obtained by the inverse wavelet transform:

$$[\mathbf{P}] = [\mathbf{M}][\tilde{\mathbf{P}}][\mathbf{M}]^T \approx [\mathbf{Z}]^{-1} \quad (9)$$

Combining (2) and (9) we have the following preconditioned moment equation:

$$[\mathbf{M}][\tilde{\mathbf{P}}][\mathbf{M}]^T[\mathbf{Z}]\mathbf{J} = [\mathbf{M}][\tilde{\mathbf{P}}][\mathbf{M}]^T\mathbf{E} \quad (10)$$

To summarize, the wavelet preconditioner $[\tilde{\mathbf{P}}]$ is generated by first finding the approximate wavelet transform of the moment matrix $[\tilde{\mathbf{Z}}]$ using (4), and then solving the Forbenius-norm minimization problem in (8). Once $[\tilde{\mathbf{P}}]$ is obtained, the preconditioning operation is carried out by a series of matrix-vector multiplication operations in (10). We now consider the computational cost of constructing $[\tilde{\mathbf{P}}]$ and that for the preconditioning operation. To construct $[\tilde{\mathbf{P}}]$, we must obtain an approximate $[\tilde{\mathbf{Z}}]$. Due to the strong

source singularity in 3-D problems, $[\mathbf{Z}]$ can be made approximately sparse with $O(N)$ non-zero elements by ignoring the far-field interactions. Therefore, the computation of $[\tilde{\mathbf{Z}}]$ can be implemented with fast 2-channel filterbank filtering with about $O(N)$ operations. Once $[\tilde{\mathbf{Z}}]$ is obtained, the complexity to solve (8) can be made proportional to the problem size N , provided that we carefully control the sparsity patterns of $[\tilde{\mathbf{Z}}]$ and its inverse. Next we consider the complexity to carry out the preconditioning operation on the left-hand side of (10). Since there are only $O(N \log N)$ non-zero elements in the wavelet transform matrix $[\mathbf{M}]$, the product of $[\mathbf{M}]$ with any vector requires $O(N \log N)$ operations. Note also that $[\tilde{\mathbf{P}}]$ is a sparse matrix with $O(N)$ non-zero elements. Therefore, if the preconditioning operation is carried out as a series of matrix-vector products on $[\mathbf{Z}]\mathbf{J}$ or \mathbf{E} , the total computation cost is limited to $O(N \log N)$ per iteration.

Numerical Results: The algorithm is tested using a 3-D conducting rectangular cavity with an open end. The (width)x(height)x(depth) dimensions of the cavity are $R \times R \times 1.5R$ where R is a size parameter. The incident plane wave is horizontally polarized with a frequency of 5.9GHz and makes an angle of 45° from the cavity opening in the elevation plane. The problem is formulated in terms of an electric-field integral equation. The Rao-Wilton-Glisson basis functions are used to form the original space-domain moment equation with a discretization size of about $\lambda_0/10$ (or 0.2"). The grayscale magnitude plots of the wavelet-based moment matrix $[\tilde{\mathbf{Z}}]$ and its inverse $[\tilde{\mathbf{Z}}]^{-1}$ are shown respectively in Figs. 2(a) and 2(b) with a problem size of $N=1024$ ($R \approx 2.1$ "). The wavelet filter used in the transform is the Daubechies filter of order 6, and the maximum wavelet transform level is $L=4$. As expected, both matrices exhibit the multi-level "finger"

structure. Accordingly we propose to use a fixed sparse matrix pattern shown in Fig. 2 with finger width D for both $[\tilde{\mathbf{Z}}]$ and $[\tilde{\mathbf{Z}}]^{-1}$ in solving the Frobenius-norm minimization problem. If the parameters D and L are kept constant, the complexity to solve (10) is proportional to the problem size N . To investigate the performance of the preconditioner, we proportionally increase the physical size of the cavity with the parameter R changing from 1.2" to 5.1" so that N increases from 256 to 8192, while the discretization interval and the frequency remain unchanged. The resulting iteration numbers in solving the moment equations as a function of the problem size are shown in Fig. 3. The iterative solver is BICGSTAB and a relative residual error of 0.001 is used as the stopping criterion. The maximum wavelet transform level is $L=5$ and the finger width D of the sparsity pattern is 16 for $N < 1024$ and 32 for $N \geq 1024$. We observe that with preconditioning, the iteration numbers are very small and grow at a very slow rate with respect to the problem size. The results demonstrate the effectiveness of the new wavelet-based preconditioner for 3-D moment equations.

Conclusions: We have proposed a wavelet-based preconditioner for 3-D electromagnetic integral equations in this work. Numerical results showed the preconditioner is very effective for ill-conditioned cavity structures. The total computational cost for the preconditioning can be kept under $O(N \log N)$. The new algorithm is compatible with fast boundary-integral algorithms such as the multilevel FMM.

Acknowledgement: This work is supported by the Air Force MURI Center for Computational Electromagnetics under Contract No. AFOSR F49620-96-1-0025, and in part by the Office of Naval Research under Contract No. N00014-98-1-0178.

References

- [1] Coifman, R., Rokhlin, V., and Wandzura, S., "The fast multipole method for the wave equation: a pedestrian prescription," *IEEE Antennas Propagat. Mag.*, vol. 35, no. 3, pp. 7-12, June 1993.
- [2] Ahn, C. H., Chew, W. C., Zhao, J. C., and Michielssen, E., "Approximate inverse preconditioner for near resonant scattering problems," Research Report, Univ. of Illinois, Apr. 1998.
- [3] Bruaset, A. M., *A survey of preconditioned iterative methods*, John Wiley & Sons, Inc., New York, 1995.
- [4] Beylkin, G., Coifman, R., and Rokhlin, V., "Fast wavelet transforms and numerical algorithms I," *Com. Pure Appl. Math.*, Vol. 44, pp. 141-183, 1991.
- [5] Grote, M. J., and Huckle, T., "Parallel preconditioning with sparse approximate inverse," *SIAM J. Sci. Comput.*, vol. 19, No. 3, , pp. 838-853, May 1997.

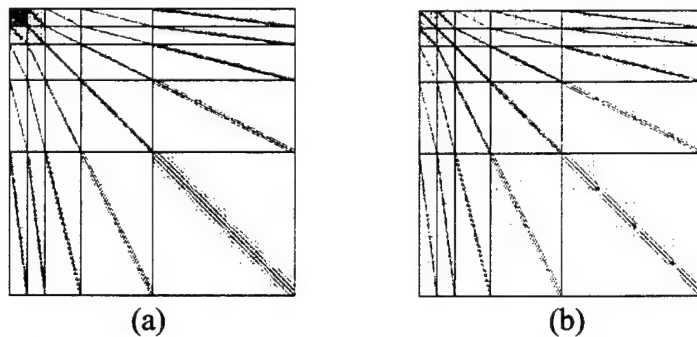


Figure 1. (a) The wavelet transformed moment matrix $[\tilde{Z}]$ for the rectangular cavity in logarithmic scale with $L=4$ ($N=1024$). (b) The inverse of the transformed matrix $[\tilde{Z}]^{-1}$.

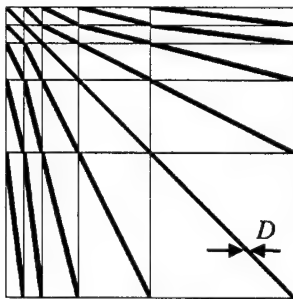


Figure 2. The non-zero pattern used to solve the Frobenius-norm minimization problem.

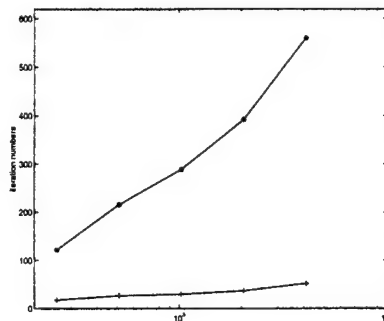
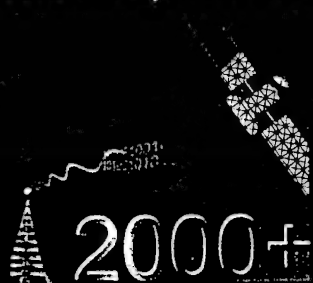


Figure 3. The iteration numbers vs. problem sizes for the cavity problem. (—*)— without preconditioning (—+— with the wavelet preconditioner).

2000 IEEE Antennas and Propagation Society International Symposium



Transmitting
Waves of Progress
to the Next Millennium



Salt Lake City, Utah
Doubletree Hotel
July 16-21, 2000

Volume One



AN IMPROVED TRIANGULAR PATCH BASIS FOR THE METHOD OF MOMENTS

Luiz C. Trintinalia¹* and Hao Ling²

¹ Department of Telecommunications and Control, Escola Politécnica da USP, Brazil.

² Department of Electrical and Computer Engineering, The University of Texas at Austin

1 - Introduction

Since the introduction of the RWG triangular patch basis function [1], it has become the most widely used basis for solving electromagnetic scattering problems with the method of moments. It has the highly desirable property of being free of line charges while being able to model arbitrarily shaped surfaces. Some authors have improved the original formulation by using curvilinear triangular patches [2] and incorporating edge conditions [3]. As pointed out in [4], it is well known that the results obtained from the RWG basis are sometimes very dependent on the meshing scheme used. Furthermore, the resulting current contains discontinuities that prevent its use for near field prediction. Although some filtering can be used before its use [5], the extra filtering operation results in loss of resolution. These problems are due to the fact that the RWG basis function cannot represent an arbitrary linear current distribution on each triangle.

In this paper we present a new set of triangular patch basis functions. It retains the same properties as the traditional RWG basis, but is capable of representing any linear current distribution over each triangle. With this improvement, the proposed basis is much less sensitive to the meshing scheme. Moreover, it provides a better representation of the actual current distribution, leading to a faster convergence of the moment method solution. All of this can be achieved with about the same computational complexity of the RWG basis.

2 - Description of the Problem

If a closed surface is represented using NF discretized triangular patches, a set of $NE=3*NF/2$ edges connecting those triangles is obtained. If we want to generate a set of basis functions that can represent an arbitrary linear current distribution over each of those triangles, we have, for each triangle i , a current distribution given by:

$$\vec{J}_i(x_i, y_i) = (a_{xi}x_i + b_{xi}y_i + c_{xi})\vec{u}_{xi} + (a_{yi}x_i + b_{yi}y_i + c_{yi})\vec{u}_{yi} \quad (1)$$

where x_i and y_i are local coordinates in the directions tangential to the triangle i . Since we have NF triangles, the number of degrees of freedom for this problem is equal to $6 NF$.

For electromagnetic problems we are interested only in current distributions whose components normal to the edges are continuous to avoid the presence of artificial line charges. By imposing this additional condition for each edge of the surface, we obtain two constraints for each edge, thereby reducing the degrees of freedom from $6 NF$ to $3 NF$. We need, consequently, a set of $3 NF$ divergence-conforming basis functions [6] to properly solve this problem.

In [1], Rao et al. proposed a set of basis functions (RWG basis functions) having one function associated with each edge, leading to a set of only $3*NF/2$ basis functions. Clearly, such set cannot represent an arbitrary linear current distribution as described earlier, meaning that it is not complete in that sense. This has already been pointed out in [6], but the solution proposed was to increase the order of the basis using quadratic functions.

To solve this problem we have developed a new set of linear basis functions (which we shall term the TL basis functions) where we have two vector basis functions associated with each edge $b-c$, as seen in Fig. 1:

$$\vec{f}_1(\vec{r}) = \begin{cases} \frac{l}{(2A^+)^{1/2}} \|\vec{\rho}^+ \times \vec{\rho}_c^+ \| \vec{\rho}_c^+ & \vec{r} \text{ in } T^+ \\ \frac{l}{(2A^-)^{1/2}} \|\vec{\rho}^- \times \vec{\rho}_c^- \| \vec{\rho}_c^- & \vec{r} \text{ in } T^- \end{cases} \quad \vec{f}_2(\vec{r}) = \begin{cases} \frac{l}{(2A^+)^{1/2}} \|\vec{\rho}^+ \times \vec{\rho}_b^+ \| \vec{\rho}_b^+ & \vec{r} \text{ in } T^+ \\ \frac{l}{(2A^-)^{1/2}} \|\vec{\rho}^- \times \vec{\rho}_b^- \| \vec{\rho}_b^- & \vec{r} \text{ in } T^- \end{cases} \quad (2)$$

where $\vec{\rho}^+ = \vec{r} - \vec{r}_a$, $\vec{\rho}^- = \vec{r}_a - \vec{r}$ and $\vec{\rho}_{b,c} = \vec{r}_{b,c} - \vec{r}_a$. Each of these basis functions is parallel to one edge and has a magnitude linearly proportional to the distance to the other edge, as shown in Fig. 2.

The TL basis functions share the following properties with the RWG functions:

- The current has no component normal to the boundary of the surface formed by triangles T^+ and T^- ;
- The component of current normal to the edge between the two triangles is continuous across the edge;
- The surface divergence of these functions, which is proportional to the surface charge density, is constant over each triangle, having the same magnitude on both, but opposite signs.

In fact, it can be shown that the RWG basis functions can be obtained by adding the two TL basis functions for the same edge. Because of the properties described, it will be shown that the same electric field integral equation (EFIE) formulation used with the RWG functions [1] can still be used, with only minor modifications for the new TL functions.

As an example of the improvement that can be obtained with the TL functions, Fig. 3 shows the best representation (in the mean square sense) of a sinusoidal current on a rectangular plate. We used the RWG and the TL basis functions with the same number of triangular patches. It can be seen that the representation obtained from the TL basis is significantly better than that from the RWG basis.

3 - EFIE Formulation

Using the standard EFIE formulation with the Galerkin method [1], we obtain

$$\langle \vec{E}^i, \vec{f}_{m,1} \rangle = j\omega \langle \vec{A}, \vec{f}_{m,1} \rangle + \langle \nabla \Phi, \vec{f}_{m,1} \rangle, \quad (3)$$

where $\langle \vec{a}, \vec{b} \rangle = \int_S \vec{a} \cdot \vec{b} dS$ and $\vec{f}_{m,1}$ denotes the basis functions in (2) at the m -th edge. As in [1],

because of the properties of \vec{f}_m at the edges, the last term in (3) can be rewritten as

$$\langle \nabla \Phi, \vec{f}_{m,1} \rangle = \nabla \cdot \vec{f}_{m,1}^+ \int_{T_m^+} \Phi dS + \nabla \cdot \vec{f}_{m,1}^- \int_{T_m^-} \Phi dS \quad (4)$$

One difference should be noted here. In [1] the values of the terms involving the vector potential and the incident field in (3) were approximated by their values at the centroid of the triangles. With this new set of basis/testing functions, one should use a different and more precise approximation:

$$\int_{T_m} \vec{A} \cdot \vec{f}_{m,1} dS \cong \frac{A_m}{3} \sum_{i=1}^3 \vec{A} \cdot \vec{f}_{m,1} \Big|_{\vec{r}=\vec{r}_i} \quad (5)$$

with

$$\bar{r}_1 = 2/3\bar{r}_a + 1/6\bar{r}_b + 1/6\bar{r}_c; \quad \bar{r}_2 = 1/6\bar{r}_a + 2/3\bar{r}_b + 1/6\bar{r}_c; \quad \bar{r}_3 = 1/6\bar{r}_a + 1/6\bar{r}_b + 2/3\bar{r}_c.$$

This is necessary because we now have 3 degrees of freedom for each triangle, so we need at least 3 testing points. This approximation leads to exact results when the vector potential or the incident field varies linearly.

The remaining steps to derive the matrix equation are similar to those in [1]. The integrals related to the scalar and vector potential determination, after transforming to a local system of normalized area coordinates, are the same as the RWG formulation, so the modifications needed to convert from the RWG basis to the TL basis are fairly straightforward.

4 - Numerical Results

To compare the new TL basis against the RWG basis, we have analyzed the scattering by a square conducting plate. Fig. 4 and Fig. 5 show respectively the predicted RCS and the cross polarization level for a square plate of side 1λ at normal incidence, plotted as a function of the number of basis functions used ($3 \times NF/2$ for RWG and $3 \times NF$ for TL). We can see a much faster convergence rate with the TL basis than with the RWG basis. Fig. 6 shows the current distributions obtained using a discretization of 72 triangular patches for the two types of basis functions. We see very abrupt variations of the current along the transverse direction for the RWG basis. For the TL basis, on the other hand, the current behavior is smoother, as expected. It also reaches higher values close to the side edges.

Other examples, such as scattering by a sphere, have also been analyzed and will be shown during the presentation. In all the examples we have analyzed, we always obtain, for the same meshing scheme, a better result using the TL basis versus the RWG basis in terms of RCS prediction. In terms of current distribution, the comparative performance is even better for the TL basis. Therefore this new set of basis functions represents an improvement over the RWG basis.

5 - Acknowledgments

This work was supported in part by the Air Force MURI Center for Computational Electromagnetics under Contract No. AFOSR F49620-96-1-0025, the Office of Naval Research under Contract No. N00014-98-1-0178, and a Lockheed Martin corporate research grant.

6 - References

- [1] S. M. Rao, D. R. Wilton and A. W. Glisson, "Electromagnetic scattering by surfaces of arbitrary shape," *IEEE Trans. Antennas Propagat.*, vol. 30, pp. 409-418, May 1982.
- [2] D. Wilkes and C. C. Cha, "Method of moments solution with parametric curved triangular patches," in *Proc. IEEE Int. Symp. Antennas Propagat.*, pp. 1512-1515, 1991.
- [3] W. J. Brown and D. R. Wilton, "Singular basis functions and curvilinear triangles in the solution of the electric field integral equation," *IEEE Trans. Antennas Propagat.*, vol. 47, pp. 347-353, Feb. 1999.
- [4] J. S. Kim, J. H. Yun, et al, "EMI analysis of finite sized image planes configuration using triangular patch model," *Electron. Lett.*, vol. 34, pp. 1735-1736, Sept. 1998.
- [5] Z. Altman, R. Mittra, O. Hashimoto and E. Michielssen, "Efficient representation of induced currents on large scatterers using the generalized pencil of function method," *IEEE Trans. Antennas Propagat.*, vol. 44, pp. 51-57, Jan. 1996.
- [6] R. D. Graglia, D. R. Wilton and A. F. Peterson, "Higher order interpolatory vector bases for computational electromagnetics," *IEEE Trans. Antennas Propagat.*, vol. 45, pp. 329-342, Mar. 1997.

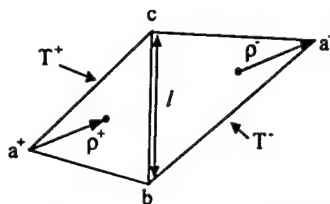


Fig. 1 Triangle pair and geometrical parameters associated.

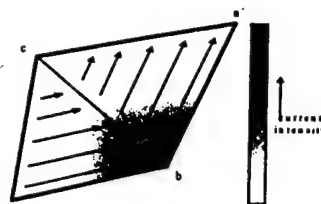


Fig. 2 New improved triangular patch basis function (of type I) intensity and direction.

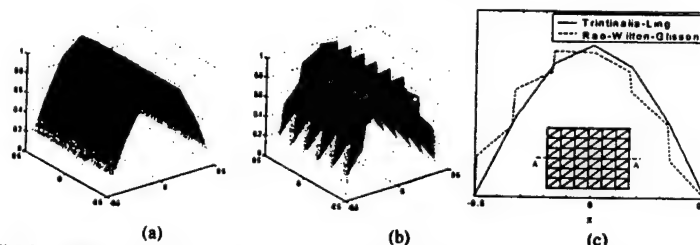


Fig. 3 (a) Sinusoidal current representation using the new TL basis functions and (b) the original RWG basis functions over a square plate, using 72 triangular patches. Figure (c) shows the A-A' cut of both representations.

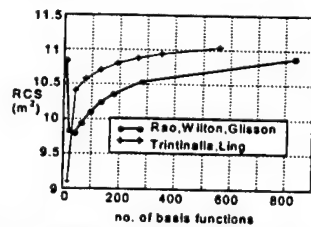


Fig. 4 Predicted RCS for normal incidence at a square plate of side 1λ , as a function of the number of basis functions used.

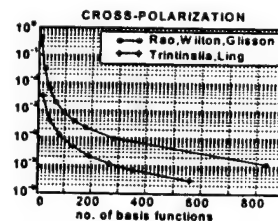


Fig. 5 Predicted cross-polarization for normal incidence at a square plate of side 1λ , as a function of the number of basis functions used.

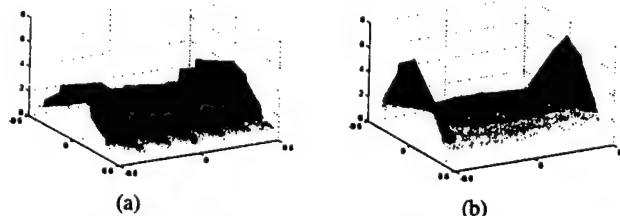


Fig. 6 Current distribution over a PEC square plate obtained using a 72 triangular patch discretization for RWG basis functions (a) and TL basis functions (b).

A Model for the Active Element Pattern of Array Elements Including Both Mutual Coupling and Platform Effects

Tao Su* and Hao Ling
Dept. of Electrical and Computer Engineering
The University of Texas at Austin
Austin, TX 78712

I. Introduction

It is well known that the mutual coupling between antenna elements in an array can strongly affect their radiation/receiving characteristics [1,2]. For direction finding applications, the result can be very sensitive to mutual coupling and such effect needs to be properly accounted for [3]. A common way to describe the coupling effect in the array signal processing community is through the use of a coupling matrix. It relates the active element patterns of the individual elements in the presence of the array environment to the idealized, free-standing element patterns. For simple antenna structures such as an array of dipoles, the coupling matrix is a very efficient description of the coupling effect. However, for arrays with more complex elements or for arrays mounted on complex platforms, such a simple model is no longer adequate.

In this paper, we propose an improved model to describe the active element patterns of an array that includes both the mutual coupling and platform effects. The key idea is to represent the additional scattering effect from the platform by point scatterers [4]. Based on the proposed model, we next devise an algorithm to extract the model parameters from the observed array response (i.e., the active element patterns) at a limited number of angles. The algorithm entails using a matching pursuit approach [5] to iteratively extract the model parameters. At each stage of the iteration, the amplitude and position of the next strongest scatterer is determined. The process continues until the difference between the model and the actual response becomes negligible. Computer simulation results show that the actual array response can be accurately recovered from the improved model. Consequently, this model can be used to effectively interpolate complex array responses from either measurement or computation made at a limited number of angles.

II. Formulation

The mutual coupling effect in an antenna array is commonly modeled by [3]:

$$\mathbf{A}_{\text{true}} = \mathbf{C} \mathbf{A}_{\text{theo}} \quad (1)$$

where \mathbf{A}_{true} is the actual array response matrix, \mathbf{A}_{theo} is the ideal array response matrix in the absence of mutual coupling, and \mathbf{C} is an angular-independent coupling matrix. The rows of \mathbf{A}_{true} are the active element patterns of the array elements versus angle. Since \mathbf{A}_{theo} is known based on the array geometry, if \mathbf{A}_{true} is given, then \mathbf{C} can be determined by using the pseudo-inverse concept as:

$$C = A_{true} A_{theo}^H (A_{theo} A_{theo}^H)^{-1} \quad (2)$$

For simple antennas whose current distributions have the same shape but different amplitudes, C can be found from A_{true} at only a few observation angles. Once C is known, A_{true} can be interpolated to very fine angular granularity based on the model.

When a platform is present, the above simple model is no longer valid. We have previously proposed an effective point scatterer model to describe the scattering off a complex platform [4]. Using this concept, the scattering from a platform can be equivalently replaced by the scattering from a set of point scatterers. Thus our proposed model for the actual array response including both the mutual coupling and platform effects can be written as

$$A_{true} = C(A_{theo} + P A_{plat}) = [C \quad CP] \begin{bmatrix} A_{theo} \\ A_{plat} \end{bmatrix} \quad (3)$$

where A_{plat} is the total phase delay due to the different point scatterers and P is an amplitude matrix representing the scattering strength from each point scatterer to each antenna element. In this model, the angular dependency due to the platform effect is accounted for by the position of the point scatterers. If we know the position of the point scatterers, the matrix C and P can be easily determined by the same pseudo-inverse procedure as in (2).

To locate the position of the point scatterers, we employ the matching pursuit algorithm [5]. During each stage of the process, we search in 2D xy-space for the best position of the next point scatterer. This is accomplished by assuming a point scatterer position, incorporating the associated phase delay into the last row of A_{plat} in (3) and solving for the corresponding C and P matrices. The location which results in the minimum

$$\|A_{true} - A_{model}(x, y)\|^2 \quad (4)$$

is then chosen as the next point scatterer. This process is similar to the back projection procedure [6], except that only the best point scatterer is retained. This process is then repeated as many times as necessary until the remainder energy is small enough to be neglected. At the end of the iteration process, both the positions of the point scatterers and the coefficients matrices C and P are determined.

III. Results

To validate the model, we simulate the array response for the structure shown in Fig. 1 using NEC. The array consists of 4 half-wave dipoles with an element separation of 0.4 wavelength. The platform is a plate approximated by 20 closely placed thin wires. The actual array response is computed at the incident angles from $\phi = -90^\circ$ to 90° . We take the response from -90° to 90° at a step of 10° to perform the modeling process described in the previous section. The first 5 extracted point scatterers are plotted in Fig. 2. Over 99% of the energy of the array response is modeled with only 5 point scatterers in this case. Fig. 3(a) shows the actual array response computed by NEC at an angular granularity of 1° . Fig.

3(b) is the array response predicted by the model. The agreement between the two is very good. As a comparison, we compute the coupling matrix directly from (2) using the computed result at all incident angles (angular granularity of 1°). The array response resulting from this model is plotted in Fig. 3(c). Even though the platform is quite small and many more incident angles are used, the predicted response misses some major characteristics. In direction finding applications, the difference can result in significant errors in the determining the direction of arrival.

In the next example, we look at a more complex platform as shown in Fig. 4. Since the platform is 10 wavelengths in length, we employ FISC [7], which is a method of moment (MoM) code based on the fast multipole method (FMM), to simulate the problem. We compute the actual array response from -180° to 180° . The point scatterers are extracted using the response at the interval of 10° . The first 15 point scatterers are plotted in Fig. 5. More than 98% of the energy is covered by the model. The actual array response and the model predicted response at an angular granularity of 1° are plotted in Fig. 6(a) and 6(b), respectively. Again the agreement is very good, demonstrating that the proposed model is effective in modeling the active element patterns on a complex platform.

IV. Conclusions

In this paper, a model is proposed to characterize both the array mutual coupling and platform effects. The platform is modeled by point scatterers and their positions are determined using a matching pursuit algorithm. The effectiveness of the model is demonstrated by numerical results. Using this model, we can describe the complex array response from measurement or simulation data collected at a limited number of incident angles.

Acknowledgment: This work was supported by the Office of Naval Research under Contract No. N00014-98-1-0178.

References

- [1] I. J. Gupta and A. A. Ksienski, "Effect of mutual coupling on the performance of adaptive arrays," *IEEE Trans. Antennas Propagat.*, v. 31, pp 785-791, Sept. 1983.
- [2] D. F. Kelley and W. L. Stutzman, "Array antenna pattern modeling methods that include mutual coupling effects," *IEEE Trans. Antennas Propagat.*, v. 41, pp 1625-1632, Dec. 1993.
- [3] B. Friedlander and J. Weiss, "Direction finding in the presence of mutual coupling," *IEEE Trans. Antennas Propagat.*, v. 39, pp 273-284, Mar. 1991.
- [4] T. Su, Y. Wang and H. Ling, "Frequency extrapolation and model-based parameterization of antenna-platform radiation from CEM data," *International IEEE AP-S Symposium*, pp. 446-449, Orlando, July 1999.
- [5] S. G. Mallat and Z. Zhang, "Matching pursuits with time-frequency dictionaries," *IEEE Trans. Signal Processing*, v. 41, pp. 3397-3415, Dec. 1993.
- [6] G. T. Herman, *Image Reconstruction from Projections*, Academic Press, New York, 1980.
- [7] *User's Manual for FISC (Fast Illinois Solver Code)*, Center for Computational Electromagnetics, University of Illinois at Urbana-Champaign and DEMACO, Inc., IL, Jan. 1997.

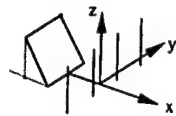


Fig. 1. Array - platform geometry for example 1

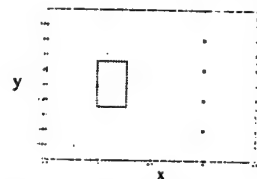


Fig. 2. Point scatterers for the structure in Fig. 1

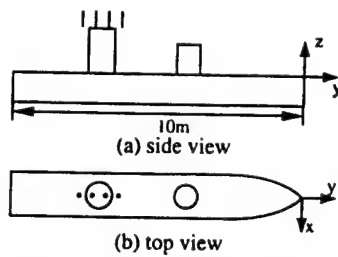


Fig. 4. Array - platform geometry in example 2

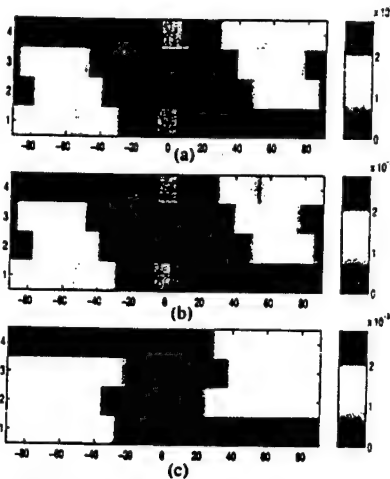


Fig. 3. Actual and model predicted array response

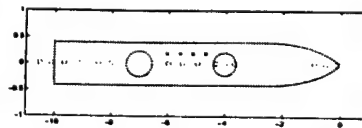


Fig. 5. Extracted point scatterers

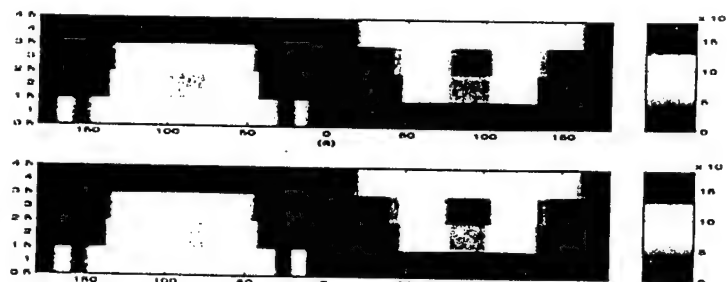


Fig. 6. Actual and model predicted array response for the structure in Fig. 4

A Wavelet-Packet Based Preconditioner for Iterative Solution of Electromagnetic Integral Equations

Hai Deng* and Hao Ling

Department of Electrical and Computer Engineering
The University of Texas at Austin
Austin, TX 78712-1084

1. Introduction

It has recently been demonstrated that the pre-defined wavelet packet (PWP) basis is very efficient for representing electromagnetic integral equation [1]. The PWP basis is designed from a wavelet packet decomposition tree that grows along the free-space wave number k_0 . It is found that the non-zero elements in the PWP-transformed matrix grow at a rate of about $O(N^{1.3})$ for small problem sizes, and the rate tends to $O(N \log N)$ for large problem sizes. Since the PWP-represented moment matrices are very sparse and diagonal-dominated, an efficient preconditioner can be constructed from the PWP-transformed moment matrix for iterative solution of moment equations. The preconditioning is especially important for near-resonant scatterers such as cavity structures, as the convergence rate of solving these problems using iterative solvers could be very slow [2].

In this work we aim to construct an effective preconditioner for moment equations from the PWP-transformed moment matrix. The preconditioning can be implemented in either the transform domain or the regular space domain. However, the computational complexity and memory requirement are at least on the order of $O(N^2)$ to transform the moment equation from the space domain to the wavelet packet domain [1]. Therefore, we devise a scheme to compute the PWP preconditioner directly from the PWP basis functions and implement the preconditioning operation in the space domain. Numerical results show that the PWP preconditioner is effective in accelerating the convergence rate of iterative solution for deep cavity structures. We also demonstrate that the total computational complexity and memory costs for the preconditioner can be kept to $O(N \log N)$, making it compatible with fast matrix-vector multiplication algorithms such as the multi-level fast multiple method (MLFMM) [3].

2. PWP-Based Approximate Inverse Preconditioner

We consider a left-preconditioned system as follows:

$$[P][Z] J = [P] E \quad (1)$$

where $[Z]$ is the space-domain moment matrix, J is the unknown induced current vector, E is the excitation vector, and $[P]$ is the preconditioner for the moment equation. To achieve the best preconditioning effect, $[P]$ should be as close to the inverse of $[Z]$ as possible. In this work we try to find such a preconditioner based on the PWP-transformed moment matrix $[\tilde{Z}]$. It can be represented as:

$$[\tilde{Z}] = [M]^T [Z] [M] \quad (2)$$

where $[M]^T$ denotes the transpose of $[M]$ and is the PWP transformation matrix. From (2), noting that $[M]$ is a unitary orthogonal matrix, we have:

$$[Z]^{-1} = [M] [\tilde{Z}]^{-1} [M]^T \quad (3)$$

Since the PWP-transformed moment matrix $[\tilde{Z}]$ is very sparse and diagonal dominant, we approximate $[\tilde{Z}]$ by a block-diagonal matrix $[\tilde{Z}_{bd}]$ that consists of the near-diagonal terms of $[\tilde{Z}]$. The approximate-inverse preconditioner $[P]$ defined in (1) is then constructed by inverting the block-diagonal matrix $[\tilde{Z}_{bd}]$ and transforming the resulting matrix back to the space domain:

$$[P] = [M] [\tilde{Z}_{bd}]^{-1} [M]^T \quad (4)$$

Therefore, the preconditioned moment equation becomes:

$$[M] [\tilde{Z}_{bd}]^{-1} [M]^T [Z] J = [M] [\tilde{Z}_{bd}]^{-1} [M]^T E \quad (5)$$

The inverse of the block diagonal matrix $[\tilde{Z}_{bd}]$ is simply the inverse of its individual diagonal blocks, and the inverted matrix $[\tilde{Z}_{bd}]^{-1}$ remains block diagonal. By properly choosing the block sizes of $[\tilde{Z}_{bd}]$, we can limit the computational cost of the inversion while maintaining the effectiveness of the preconditioner. Our approach is to divide the diagonal area of $[\tilde{Z}]$ into three parts (Fig. 1): (i) a block centered about the spectral frequency k_0 with block size M_1 , (ii) a set of diagonal blocks in the remaining upper-left region with block size M_2 , and (iii) a set of diagonal blocks in the lower-right region with block size M_3 . Because most of the energy in $[\tilde{Z}]$ is concentrated around the k_0 spectral frequency, we let M_1 grow a rate of $\sqrt[3]{N}$ with the problem size N . Next, with the chosen pattern of $[\tilde{Z}_{bd}]$, we compute the non-zero elements one-by-one using the PWP basis functions directly [1]. Since the number of non-zero elements in $[\tilde{Z}_{bd}]$ is about $O(N)$ and the average cost to compute an element is about $O(\log N)$, we can show that the total computational cost and memory requirement to generate and invert $[\tilde{Z}_{bd}]$ are under $O(N \log N)$ [4]. Finally, the PWP transformation matrix $[M]$ in (5) is sparse with about $O(N \log N)$ non-zero elements. Consequently, the computation complexity and memory requirement for the PWP preconditioning operation can be kept to $O(N \log N)$.

3. Numerical Results

To test the performance of the PWP preconditioner, we use an open-ended inlet shown in Fig. 2(a) as the scatterer. The combined field integral equation (CFIE) is used to construct the moment equation. Fig. 2(b) is the moment matrix $[\tilde{Z}]$ represented by the PWP basis for the inlet structure with dimensions $l:m:=15:1:1$ and $N=256$. We observe that the matrix is sparse and diagonal-dominant, with the strongest elements located around k_0 and the low spectral frequency areas.

Fig. 3 shows the iteration number required to solve the PWP preconditioned system versus the problem size with $l:m:=15:1:1$. In the PWP preconditioner,

we choose $M_2=32$, $M_3=1$, and let M_1 grow at a rate of $\sqrt[3]{N}$ starting from 32 at $N=128$. The problem size N is increased by proportionally increasing the scatterer size. The iterative solver used is the conjugate-gradient squared (CGS) method, and the stopping criterion is when the relative residual error is less than 10^{-6} . For comparison, we also show the results from a simple block-diagonal preconditioner in the space domain. We find that the iteration number grows rapidly with the problem size if no preconditioning is applied. With the PWP preconditioner applied, the iteration numbers are significantly reduced and they increase more slowly with problem size. Furthermore, the PWP preconditioner performs better than the equivalent space domain preconditioner.

Fig. 4 shows the convergence behavior of the preconditioned system for a fixed problem size ($N=512$) with the BiCGSTAB algorithm as the iterative solver. The residual error is plotted as a function of the number of iterations for the moment equation without any preconditioning, or with preconditioning in the space domain or the PWP basis domain. We observe that, with the PWP preconditioning, the relative residue decreases the fastest. In addition, the convergence behavior is more stable. Similar convergence behaviors are found for larger problem sizes and for other near-resonant configurations.

4. Conclusions

Due to the vanishing moments of wavelet basis functions, the PWP-based moment matrix is sparse and diagonally concentrated. Consequently, an effective preconditioner can be more easily constructed than that based on the space-domain moment matrix. Numerical results showed that the iteration numbers for the PWP-preconditioned moment equations are significantly smaller and grow at a lower rate than those without preconditioning or preconditioned using a space-domain preconditioner. The complexity for the construction and preconditioning operation of the PWP preconditioner is kept under $O(N \log N)$ in both computational cost and memory requirement.

Acknowledgment: This work was supported by the Air Force MURI Center for Computational Electromagnetics under contract AFOSR F49620-96-1-0025, and in part by the Office of Naval Research under Contract No. N00014-98-1-0178.

References:

- [1] H. Deng and H. Ling, "On a class of pre-defined wavelet packet basis for efficient representation of electromagnetic integral equations," to appear in *IEEE Trans. Antennas Propagat.*, Nov. 1999.
- [2] C. H. Ahn., W. C. Chew, J. C. Zhao and E. Michielssen, "Approximate inverse preconditioner for near resonant scattering problems," Research Report, Univ. of Illinois, Apr. 1998.
- [3] J. M. Song, C. C. Lu and W. C. Chew, "Multi-level fast-multipole algorithm for electromagnetic scattering for large complex objects," *IEEE Trans. Antennas Propagat.*, vol. 45, pp. 1488-1493, Oct. 1997.
- [4] H. Deng and H. Ling, "Preconditioning of electromagnetic integral equations for iterative solvers using pre-defined wavelet packet basis," *Electronics Lett.*, vol. 35, pp. 1144-1146, July 1999.

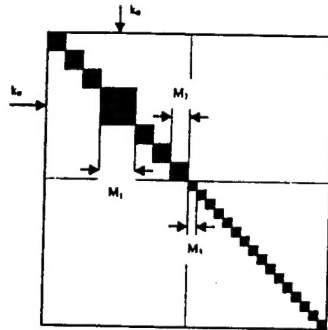


Figure 1. The block structure used to construct $[\tilde{Z}_{bd}]$

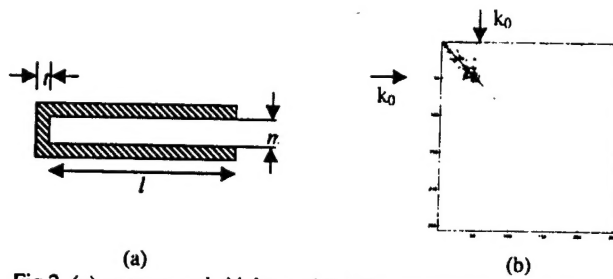


Fig.2. (a) an open-ended inlet, and (b) The moment matrix represented by PWP basis $[\tilde{Z}]$, for the inlet with $N=256$ (in logarithmic scale).

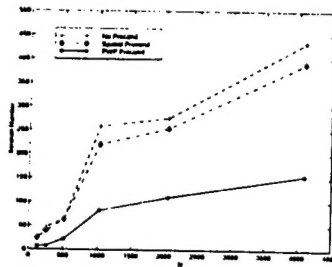


Figure 3. Iteration numbers vs. problem sizes for solving moment equations using different preconditioning methods

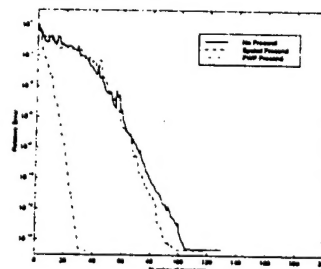


Fig.4. Convergence behaviors of the various preconditioned systems versus iteration numbers for PWP and other preconditioning methods with $N=512$.